Studies on

Fabrication and Characterisation of

TiO$_2$ based Dye-sensitised Solar Cells

A thesis

submitted in partial fulfillment of the

requirements for the degree of

Master of Science in Engineering

in the Faculty of Engineering

by

S. Sharmila

Department of Chemical Engineering

Indian Institute of Science

Bangalore 560012 (India)

2015

Declaration

I hereby certify that the report was written by me, according to the Departmental Guidelines and that in writing the report,

1. the experimental data collected and the simulation results obtained by me have been presented without any bias, modifications or alterations, and can be obtained by others using the information provided in the report,

2. I have not copied material from published or unpublished sources (text books, reports, papers, web sites etc.),

3. where material from any source was used, the source was given due credit by citing it in the text of the report and giving its details in the section on references,

   and

4. where material from any source was copied, it was put in quotation marks, and the source was given due credit by citing it in the text of the report and giving its details in the section on references.

S. Sharmila

Acknowledgements

Abstract

Photovoltaic cells are a promising solution to the current energy crisis. Among the different photovoltaic cell technologies developed, dye-sensitised solar cells (DSSC) are emerging as viable low-cost alternatives to Si PV technology. This thesis presents studies on fabrication and characterisation of TiO_2 based dye-sensitised solar cells. Chapter 1 gives an overview of different photovoltaic cell technologies and a review of the state-of-the art DSSC technology. Chapter 2 describes the techniques used for characterisation of DSSCs. Chapter 3 describes the fabrication of TiO_2 based dye-sensitised solar cells. Chapter 4 presents the analysis of measurements obtained by the characterisation techniques. Finally chapter 5 summarises the work done and suggests directions for future work.

iv

TABLE OF CONTENTS

List of Figures

x

List of Tables

Chapter 1

Introduction

1.1 Background

Photovoltaic (PV) cells are semiconductor based devices that convert sunlight to electricity. Photovoltaic cells were first developed as a source of power to run communication and military satellites in the outer space by the US[1]. The increasing demand for energy due to rapid urbanization and the negative impact of fossil fuels on climate change necessitated the use of alternate, renewable sources of energy which would leave minimum carbon footprint. This gave a major thrust to photovoltaic cell research. Research started with pure single crystal Si solar cells and has now diversified to cells with compound semiconductors, organic solar cells[2],[3],[4], dye sensitised solar cells and quantum dot solar cells[5],[6],[7],[8].

First generation solar cells use the highest purity materials with least structural defects such as single crystal Si, of purity 99.9999%. These cells yield the highest efficiency (of about 25% [9]) that solar cells have produced till date. Impurities and defects accelerate the recombination of electrons and holes and can bring down the efficiency of a solar cell. It is therefore important to maintain high levels of purity in all stages of fabrication. This stringent requirement for purity translates to high capital cost and high energy input for production. These solar cells are therefore very expensive.

Second generation solar cells include thin film cells made up of multi-crystalline or amorphous Si, CdTe and Cd-In-Ga-Se(CIGS). These cells are fabricated by less energy intensive techniques such as electroplating and vapour deposition. These cells, however, have a higher amount of defects, and hence their power conversion efficiency is lower, in the range of 10.1% to 19.6% [8].

Third generation solar cells comprise dye-sensitised solar cells, organic solar cells and quantum dot cells. They are relatively easier to fabricate and significantly cheaper than the first and the second generation solar cells. These cells are, however, not as efficient as the first two generations of solar cells. Nevertheless, the advantages of low cost and flexibility offset the disadvantage of lower efficiency and open new avenues for applications, e.g., building integrated photovoltaic cells[10].

1.2 Working principle of conventional p-n junction solar cells

The energy conversion process in photovoltaic cells consists of two important steps. First, the absorption of light generates an electron-hole pair. The electron and the hole are then separated by the structure of the device − electrons to the negative terminal and holes to the positive terminal − thus generating electrical power. It requires an understanding of the concept of energy levels in atoms and molecules to understand these processes. In a molecule, the lowest lying permitted energy levels are filled first, upto the highest occupied molecular orbital (HOMO); the next available energy level which is empty is termed the lowest unoccupied molecular orbital (LUMO). In a bulk crystalline semiconductor, the HOMO and the LUMO of the constituent molecules converge into valence and conduction bands respectively. In the absence of dopants, the electrochemical potential − the Fermi level − of the pure semiconductor lies in the band-gap of the valence and the conduction bands. Addition of electron donors, termed **n-doping**, makes the material electron rich and the Fermi level moves closer to the conduction band. Addition of electron acceptors, termed **p-doping**, depletes the electrons available and the Fermi level moves closer to the valence band. In an n-type material, the number of positively charged donor atoms (called positive ions), which are not free to move, exactly balance the number and charge of the negative free electrons. Similarly, in a p-type material, the number of negatively charged acceptor atoms which are immobile, balance the number and charge of the positive free holes. In a sandwich structure composed of n-doped and p-doped semiconductor, bending of the bands occurs in the vicinity of the junction with the bulk of the n-type and the p-type remaining unaffected. Electrons from the n-type diffuse into the p-type leaving

behind immobile positively charged donor atoms near the junction; holes from the p-type diffuse into the n-type leaving behind immobile negatively charged acceptor atoms near the junction. The immobile ions establish a "built-in" electric field. The electric field points from the positively charged donor ions in the n-type to the negatively charged acceptor ions in the p type. The free electrons and holes are influenced by this "built-in" electric field with the electrons drifting towards the positive donor ions and the holes drifting towards the negative acceptor ions. The drift current is in the direction opposite to the diffusion current. At equilibrium, the drift current is equal to the diffusion current and so, there is no net flow. At equilibrium there is a single Fermi level. When the cell is illuminated, additional charge carriers are generated, and the single Fermi level splits into two quasi-Fermi levels in the n-type or p-type region; the higher the light intensity the wider they split. Closer to the electrode, both the quasi-Fermi levels move towards the majority quasi-Fermi level of the external circuit. This shift of the Fermi levels in the electrodes represents the open circuit voltage V_{oc}. Such separation of charge carriers permits a selective collection at the collector electrodes and a net conversion of sunlight to electric power. This is illustrated in figure 1.1.
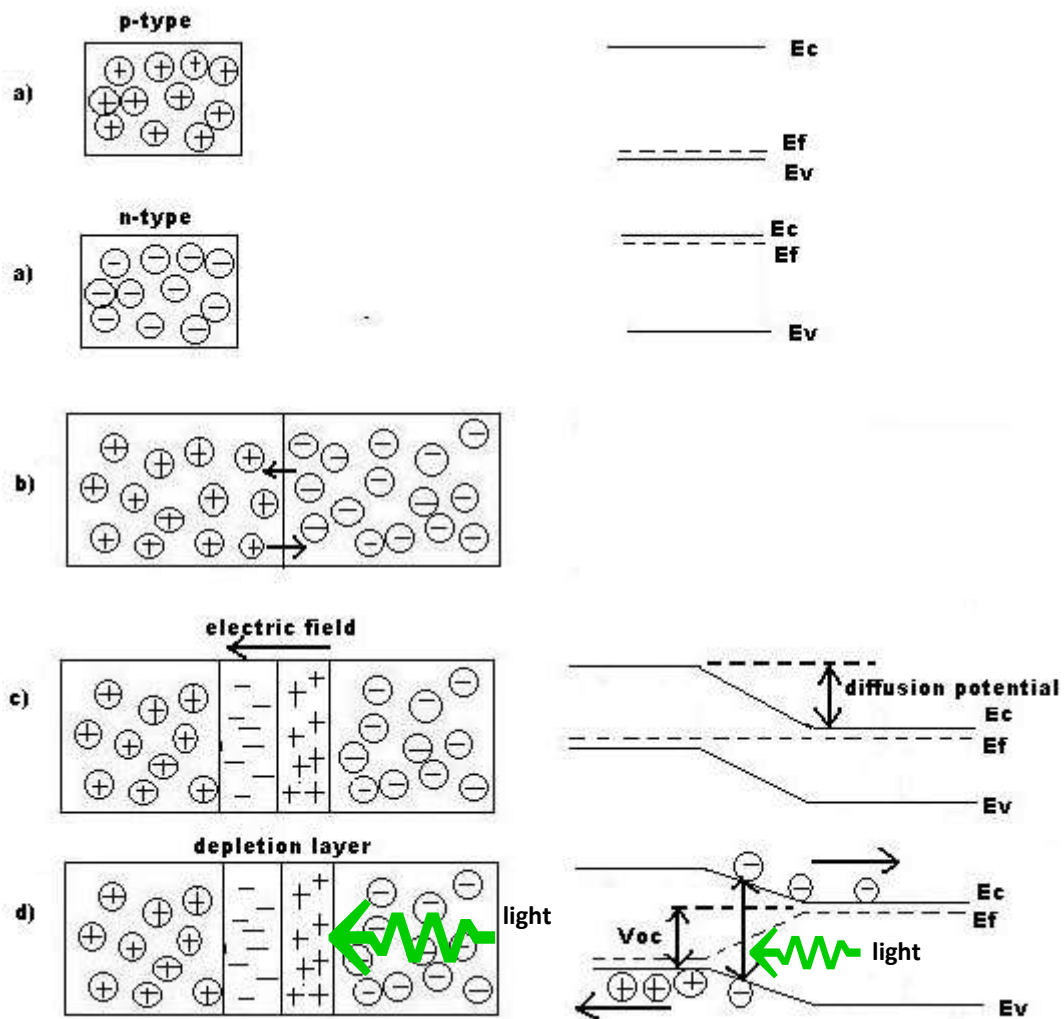
Figure 1.1 Band picture showing the conduction band E_c, valence band E_v, Fermi level E_f of a) p, n type semiconductors in isolation, b) p-n contact for the first time, c) p-n junction in equilibrium, d) p-n junction under illumination.

1.3 Dye-sensitised Solar Cells

Dye-sensitised solar cells (DSSC) belong to the category of third generation photovoltaic cells. They are a promising alternative to the conventional silicon based solar cells as they can be fabricated from relatively impure materials and hence are cheaper than silicon cells. This technology is inspired by photosynthesis and electricity generation is realised by means of a dye anchored to a wide-bandgap semiconductor: the dye mimics the functioning of the green-coloured pigment, chlorophyll, in leaves in that it absorbs light and generates excited electrons. The key advantage of a DSSC over other types of solar cells is that it is the only device that can decouple the functions of light absorption and charge transportation during the photoelectric conversion process. Hence it is possible to individually tailor the components for obtaining a high efficiency DSSC.

The first high efficiency DSSC based on nanoparticles was developed in 1991 by Brian O'Regan and Michael Grätzel. The cell which employed a nanoparticulate titanium dioxide (TiO_2) film as the semiconductor and a ruthenium (Ru) based dye recorded an efficiency of over 7% [11]. Since then, this field has seen tremendous growth with efforts concentrated on optimizing the various components of a DSSC for improving its efficiency to make it commercially viable. The various components of a DSSC include a dye, a wide bandgap semiconductor, an electrolyte with a redox mediator, a catalyst to reduce the redox species, a substrate for the semiconductor and for catalyst deposition and a sealant. The layer details of a typical DSSC are shown in figure 1.2. Cells have been developed with various combinations of materials and electrode geometries. These include mesoporous films, nanotubes, nanowires of TiO_2 [12],[13],[14],[15] and ZnO[16],[17],[18],[19],[20],[21],[22], metal-based and metal-free organic dyes[23],[24], liquid and solid-state electrolytes[25],[26],[27], Pt and carbon based[28],[29],[30],[31],[32],[33],[34],[35],[36] counter electrodes as well as flexible[37],[38],[39] and rigid substrates.

Cover glass (0.1 mm thickness)

End sealant surlyn 1702 0.025mm

holes for fliiling electrolyte

FTO layer

Pt layer

Sealing spacer (Surlyn 1702, 0.025 mm)

nanocrystalline TiO2 film thickness 12-15um

FTO layer

Glass substrate
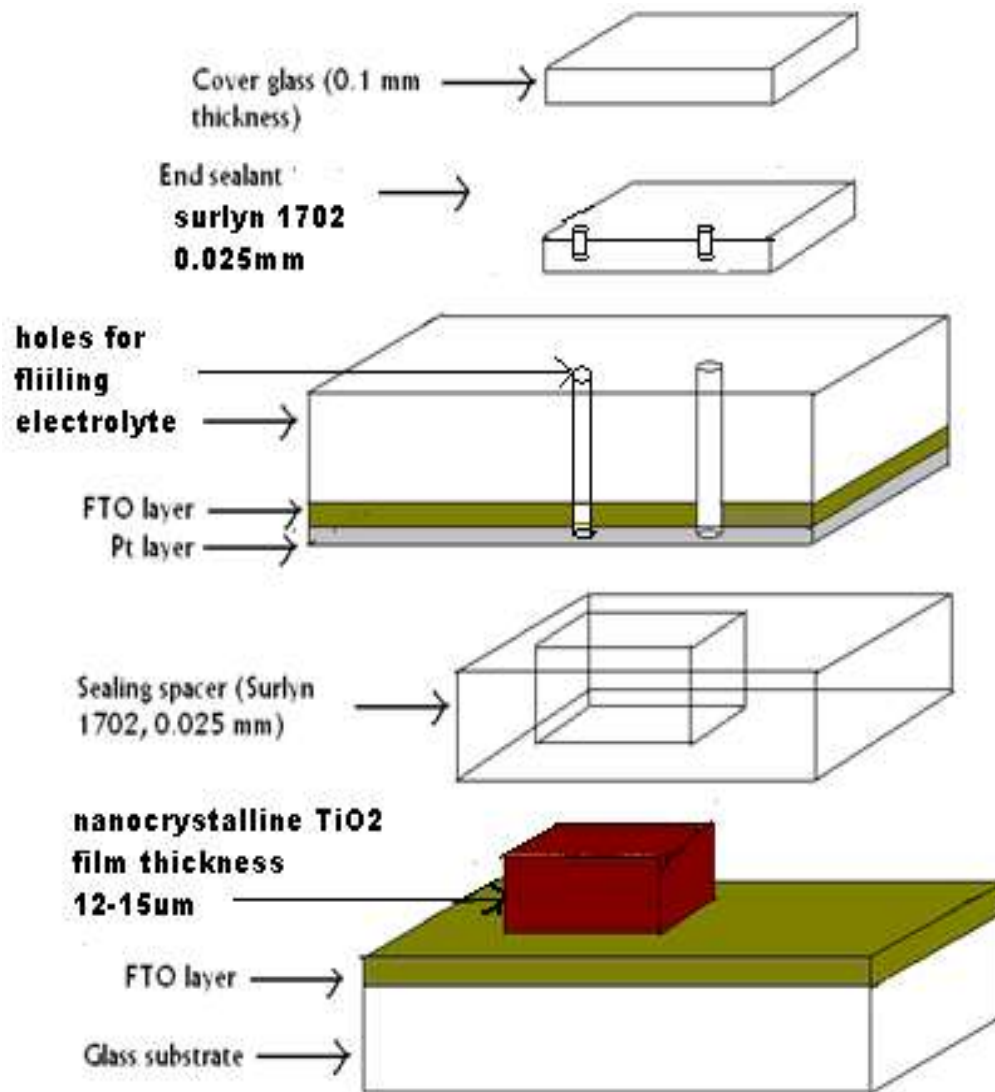
Figure 1.2 Structure of a DSSC

1.3.1 Energetics of a Dye-sensitised Solar Cell

A typical DSSC has the following three components

1. A mesoporous nanocrystalline TiO_2 film with the surface sensitised with a dye and deposited on a transparent conducting oxide (TCO) glass, which constitutes the photoanode
2. A platinized TCO glass, which is the cathode
3. A redox species (I^-/I_3^-) as the hole transporting medium in an organic solvent

Titanium dioxide (TiO_2) is a wide bandgap semiconductor with a bandgap of 3.2 eV for the anatase form. As such TiO_2 is sensitive to light of wavelength less than 400 nm only, which constitutes a mere 4% of the incoming solar radiation. In order to harvest the majority of the radiation, the surface of TiO_2 is sensitised with a dye which has a broad absorption spectrum in the visible light and near IR region. Dyes are chosen such that the LUMO level overlaps with the conduction band energy level of TiO_2. This provides the necessary driving force for the transfer of optically excited electrons from the LUMO level to TiO_2. When a cell is irradiated with sunlight from the TiO_2 side, the electrons in the HOMO level of the dye are excited to the LUMO level, which are then injected into the conduction band of TiO_2. The electrons travel through the external circuit to the counter electrode. Meanwhile, the dye is in an oxidized state after the loss of electrons. The oxidized dye rapidly reacts with I^- ions and returns to its ground state. The resulting I_3^- ions diffuse to the counter electrode where they are reduced back to I^-. The difference in the Fermi energy levels of the conduction band of TiO_2 and the redox couple, ΔV, is the open circuit potential V_{oc}. This process is illustrated in figure 1.3. The various electron and energy transfer processes occurring in a DSSC are symbolically represented below.

Anode: $S + h\upsilon \rightarrow S^*$ (photoexcitation of the dye)

$S^* \rightarrow S^+ + e^-cb$ (charge injection into conduction band of TiO_2)

$2S^+ + 3I^- \rightarrow 2S + I_3^-$ (regeneration of dye)

Cathode: $I_3^- + 2e^- \rightarrow 3I^-$ (regeneration of I^-)
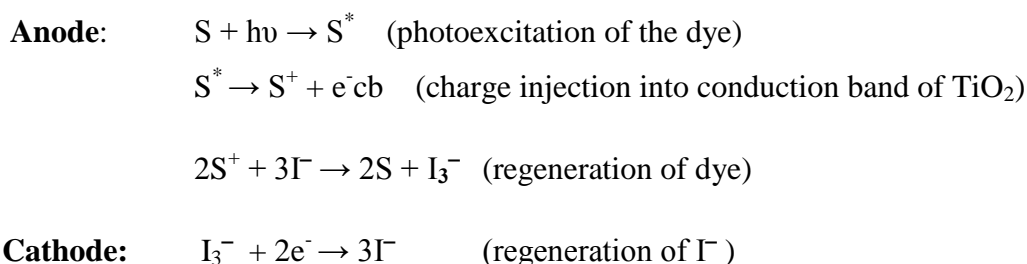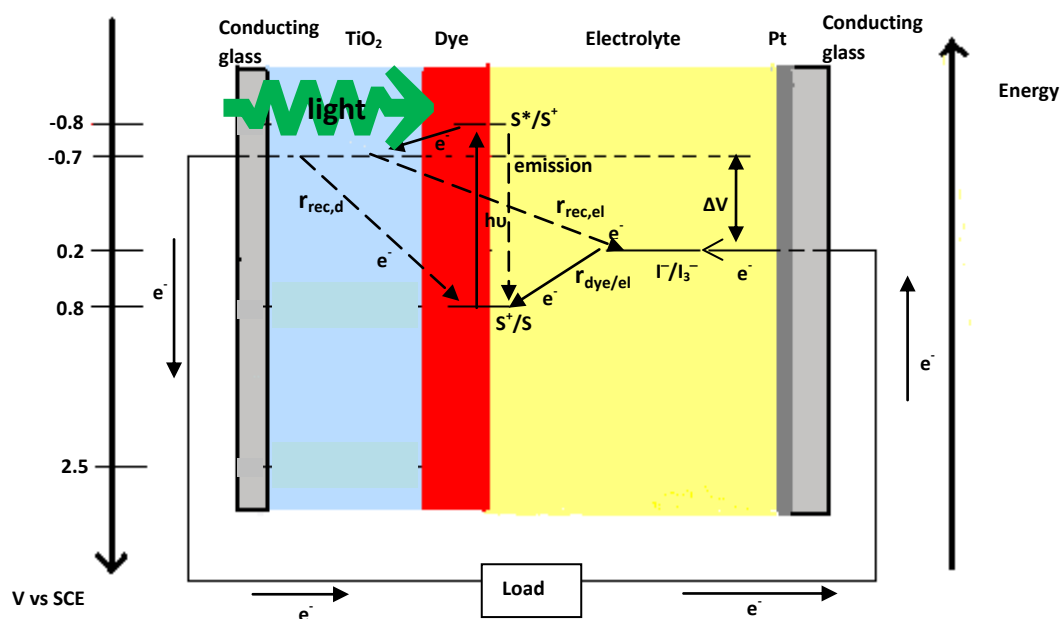
Figure 1.3 Operating principle and schematic of energy level representation of a DSSC [40].
Optical excitation of the dye is followed by injection of electrons into the TiO$_2$ conduction
band denoted by r$_{inj}$. The oxidized dye is reduced by I$_3^-$ / I$^-$ present in the electrolyte
denoted by r$_{dye/el}$. The solid arrow lines indicate the electricity generating reactions
which contribute to the efficiency of the cell. The dotted arrow lines indicate the
competing parasitic reactions which reduce the efficiency. These are recombination of
conduction band electrons with the dye cation and the oxidized species in the electrolyte,
r$_{rec,d}$ and r$_{rec,el}$ respectively and the decay of the excited state of the dye.

Parasitic reactions: $S^* \rightarrow S + h\upsilon$ (emission – decay of excited state)

$S^+ + e^-cb \rightarrow S$ (recombination)

$2e^-cb + I_3^- \rightarrow 3I^-$ (recombination)
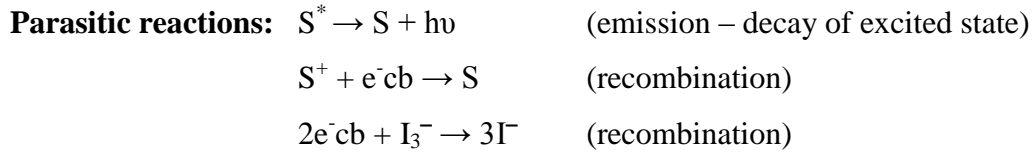
The parasitic reactions reduce the energy conversion efficiency of the cell.

In order to have a DSSC with a high overall power conversion efficiency, the light harvesting efficiency, η_{lh}, the efficiency of injection of the optically excited electron into the semiconductor, η_{inj}, and the efficiency of collection of the injected photon, η_{col}, should be close to unity. This requires that the rate of electron injection, r_{inj}, must be higher than the decay rate of the excited state to the ground state, and the rate of recombination of the dye cation with the electrons injected into the conduction band of the semiconductor, $r_{rec,d}$, should be lower than the rate of reduction of the oxidized dye by the iodide ion, $r_{dye/el}$. Typically, the time scale for electron injection into the conduction band of TiO$_2$ is in the range of femtoseconds to picoseconds, which is several orders of magnitude lesser than the lifetime of the excited state of a dye. This ensures a high quantum yield. Moreover, the oxidized dye molecules can be rapidly reduced by I$^-$ ions present at high concentrations, typically 0.5M. Thus, the recombination between the oxidized dye and the injected electrons in TiO$_2$ (given by the rate $r_{rec,d}$) can be neglected. However, due to the low diffusion co-efficient of electrons ($D_n < 10^{-4}$ cm^2 s^{-1} [41]) in TiO$_2$ film compared to that in a single crystal, recombination (given by the rate $r_{rec,el}$) can occur between the injected electrons in TiO$_2$ and I$_3^-$. This causes a significant energy loss in a DSSC. This can, however, be minimized by the addition of suitable blocking agents, thus improving the conversion efficiency. The following section gives an account of the options available for optimizing the efficiency of a DSSC.

1.3.2 Strategies for optimization of DSSC

As a DSSC is made up of many components and there are many candidates for each component, the key to achieving a high efficiency DSSC lies in optimizing the composition of each component for a particular combination. The role of each component is discussed below.

1.3.2.1 Substrates for DSSC

The most common substrate for DSSC is glass with fluorine doped tin-oxide (FTO) as the conductive coating. Sheet resistance and transparency are two important parameters for the selection of FTO glass. The lower the sheet resistance, the better the conduction; this however reduces the transparency of glass. The optimal sheet resistance is in the range of 8–15 $\Omega/\square$, for which the transmission is in the range of 65–80% [42] in the wavelength region 400–1000 nm. This is illustrated in figure 1.4.

(a)   **(b)**
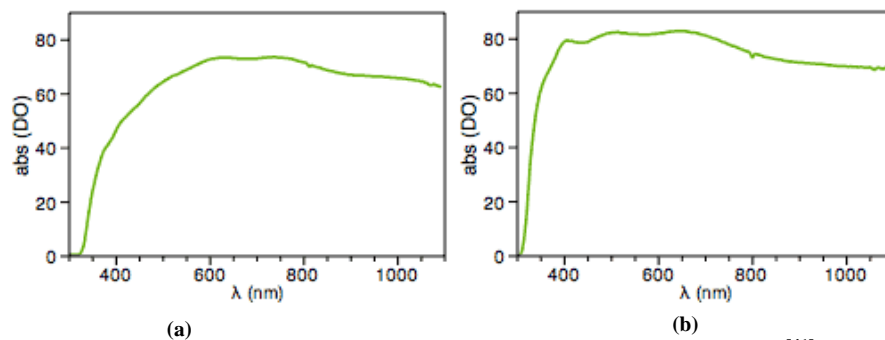
**Figure 1.4 Transmission spectrum of FTO glass of sheet resistance (a)8 $\Omega/\square$ [41] (b) 15 $\Omega/\square$ [41] .
Glass with sheet resistance of 15 $\Omega/\square$ is more transparent than 8 $\Omega/\square$ as it has higher
transmission in the visible region**

For flexible applications, plastic substrates, Ti metal and stainless steel have been used. DSSCs with plastic substrates exhibit low efficiency as photoelectrode films cannot be sintered at high temperatures. Temperature in the 450–500°C range is required for proper formation of interparticle connections by necking of particles in the films, which is crucial for high efficiency. Cells with Ti metal and stainless steel as substrates for the films have demonstrated efficiencies comparable to glass substrates. These cells are illuminated from the transparent counter electrode side, in which the electrolyte intercepts light in its characteristic region. This reduces the light harvesting efficiency of the dyed photoanode in the corresponding wavelength range and hence results in lower efficiencies compared to a transparent photoanode.

1.3.2.2 Photoelectrode

Titanium dioxide (TiO$_2$) is the undisputed choice for the photoelectrode owing to its chemical compatibility with many dyes, low cost, abundance and non-toxicity. The high efficiency DSSCs produced till date employ a mesoporous film of TiO$_2$ as the working electrode. These DSSCs have a mesoporous TiO$_2$ film with optimal thickness in the range of 12–15 μm made of TiO$_2$ nanoparticles in the size range of 10–30 nm. There are many procedures available in literature for the preparation of TiO$_2$ pastes for the film. These pastes are prepared using commercial TiO$_2$ powders or TiO$_2$ yielding precursors such as titanium alkoxides and organic binders, organic solvents and acids. The purpose of the additives is to improve the porosity of the film after it is sintered. The film is sintered in the temperature range of 450 – 500 °C for complete oxidation of the organic additives and also for internecking of particles. This procedure is adopted for glass substrates. When plastic substrates are used, organic additives are kept to a minimum and the films are sintered at temperatures less than 150 °C to prevent the decomposition of plastic substrates. However, the efficiency achieved using plastic substrates is significantly lower than that of glass substrates. This can be attributed to the poor internecking between particles at low temperatures which increases the resistance to electron mobility through the film. The different morphologies and electron transport routes are presented in figure 1.5

The other wide bandgap semiconductor that has been used is ZnO with a bandgap of 3.37 eV. ZnO offers the advantage of easy fabrication of nanowires. Electron transport in nanowires is of the order of $10^{-5} – 10^{-3}$ cm^{2}s^{-1} [40], which is two orders of magnitude faster than in nanocrystalline films ($10^{-7} – 10^{-4}$ cm^{2}s^{-1} [40]), as there is direct contact between the semiconducting oxide and the conducting substrate. ZnO nanowires are prepared by hydrothermal method[43] or chemical vapour deposition (CVD)[44] method. ZnO cells are reasonably efficient. However, ZnO has chemical compatibility issues with dyes which are commonly used with TiO$_2$. Therefore, only a narrow range of dyes can be used.

12
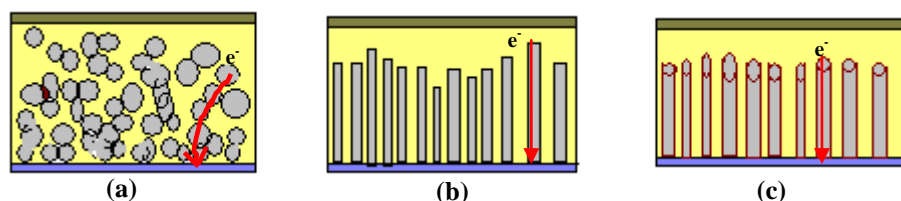
Figure 1.5 Different morphologies for photoelectrodes and electron transport route (a) mesoporous film based on nanosized particle. Electron transport route to the conducting substrate is circuitous. (b) nanowire (c) nanotube. In case of (b) and (c) transport route is shorter as there is direct contact between photoelectrode and conducting substrate

1.3.2.3 Dyes

The dye should be panchromatic, i.e., should absorb all light below 920 nm and should have a high molar extinction co-efficient. Among the metal based dyes, the Ru-based dyes N945[45], N3 and N719 yield the highest efficiencies of over 10% amongst thousands of dyes tested. However, the high price of Ru led to the quest for metal-free organic dyes. The requirements for organic dyes are that their LUMO energy level should overlap with the conduction band energy level of the semiconductor for successful injection of excited electrons; they should not contribute to charge recombination; they should have the least tendency to aggregate and they must also demonstrate long term stability. The zinc-porphyrin dye YD2–o–C8 in conjunction with Co(II/III)tris(bipyridyl)-based redox electrolyte demonstrates the highest efficiency of 11.9% [21]. Another dye, C219, coupled with Iodide/tri-iodide based redox couple[22] exhibits efficiencies of 10.3% which is on par with the Ru-based dyes.
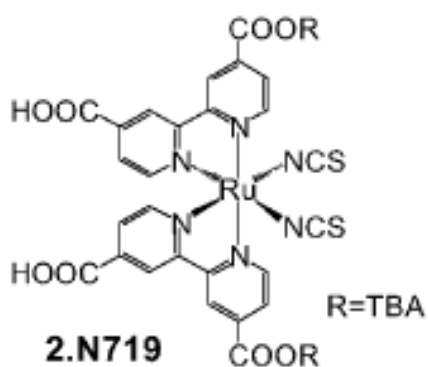
Figure 1.6 Structure of N719 dye[46]
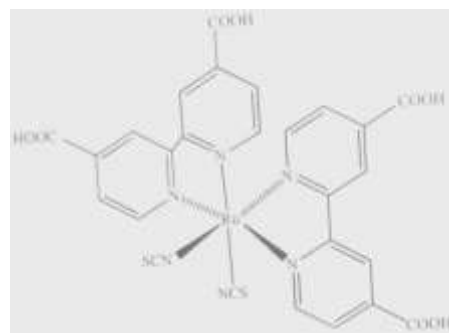
Figure 1.7 Structure of N3 dye[47]
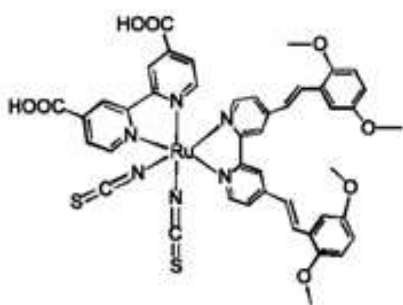
Figure 1.8 Structure of the dye N945[44]
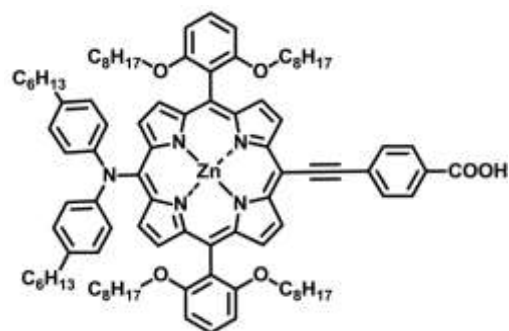
Figure 1. 9 Structure of the dye YD2–o–C8[21]
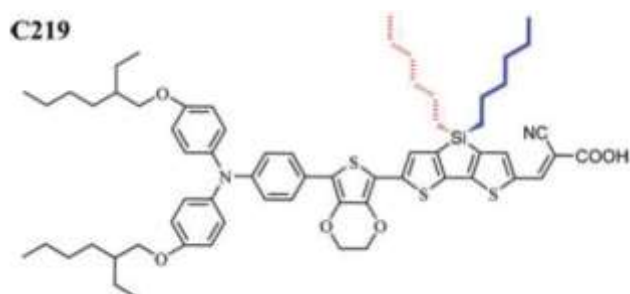
Figure 1.10 Structure of the organic dye C219[22]

1.3.2.4 Electrolytes

The I_3^- /I^- redox mediator in acetonitrile, methoxypropionitrile or valeronitrile is the most commonly used electrolyte. The solvents used should possess low viscosity to permit faster diffusion of the electrolyte species to the counter electrode for reduction. A high rate of diffusion is crucial for high efficiency DSSC because slow diffusion enhances the rate of recombination of injected electrons with electrolytes. The solvents with low viscosity are usually low boiling solvents. These solvents make for high efficiency DSSCs but a common drawback is that of leakage of the solvent. Liquid electrolyte cells are usually composed of LiI and I_2 which form the redox couple I_3^- /I^-. Compounds like tert-butyl pyridine and guanidine thiocyanate are added to suppress the recombination of photo-injected electrons in TiO_2 with the redox species. Solvent-free electrolyte systems containing room temperature ionic liquids like hexamethyl imidazolium iodide (HMII), dimethyl imidazolium iodide are the other alternatives to liquid electrolytes. These are however expensive.

1.3.2.5 Counter electrode

The counter electrode should exhibit a high catalytic activity and have a charge transfer resistance of less than 10 Ωcm^2 [48]. Platinum is the best candidate for counter electrodes. There are different methods available for the deposition of Pt. These include the electrochemical deposition[49] method suitable for plastic substrates, sputtering[50],[51] and thermal deposition. Platinum, like Ru, is expensive and contributes significantly to the cost of a DSSC. With a view to reducing the cost, carbon based counter electrodes have been used. Carbon black[28], graphene[33],[34] and carbon nanotubes[30] have shown efficiencies comparable to a Pt DSSC.

1.3.2.6 Solid state DSSC

The use of volatile electrolytes gives rise to stability problems. Solid state electrolytes were developed to counter this problem. The most commonly used solid state electrolyte is spiro-OMeTAD. Another high performing electrolyte is the plastic crystal (PC)-based electrolyte[52] for a nanofiber TiO_2 structure. The state-of-the-art solid state cell is the perovskite-based DSSC which uses perovskite as the light

absorber instead of metal-based dyes or organic dyes, and PTTA/spiro-OMeTAD as the hole transporting medium[53].

1.3.2.7 Sealant

Sealants are crucial for the prevention of the loss of the electrolyte and the ingress of air and moisture which can degrade the life of a DSSC. Commercial sealants include thermal adhesives like Surlyn and Bynel which can be heat sealed in the temperature range of 100–130 °C. Other sealing options include glass frit sealing at a high temperature of 500 °C in which case the dye and the electrolyte are pumped into the cell after the sealing.

1.4 Commercialization of DSSC

Development of DSSC modules with efficiencies of atleast 10% and a lifetime of 20 years is important for commercial viability of DSSC. These modules also have to undergo the following tests prescribed by IEC 61215, IEC 61646, JIS C-8938 and ASTM E 1171 to be certified for their performance:

- Thermal-cycling test: cycling between 85 °C and -40 °C at 100 °C/hour maximum rate (to assess the module's ability to withstand exposure to several environmental conditions during transportation and/or storage)
- Temperature-humidity cycling test: cycling between +85 ±2 °C and -40 ± 3°C at 85% ± 5% relative humidity (RH), at 100 °C/hour maximum rate (to determine the deterioration level for use and/or storage in a short time under conditions of temperature change in high relative humidity)
- Light soaking: exposure of the solar cell to continuous illumination of solar radiation for 1000 hours

Dyesol, 3G Solar, G24 Innovation, Aisin Seiki Co. Ltd. and Toyota Central R&D laboratories, Fujikura Ltd., Peccell Technologies Inc., Sharp Co., Sony Co., KIST[54] are the centres involved in the development of DSSC modules. Larger modules can be

16
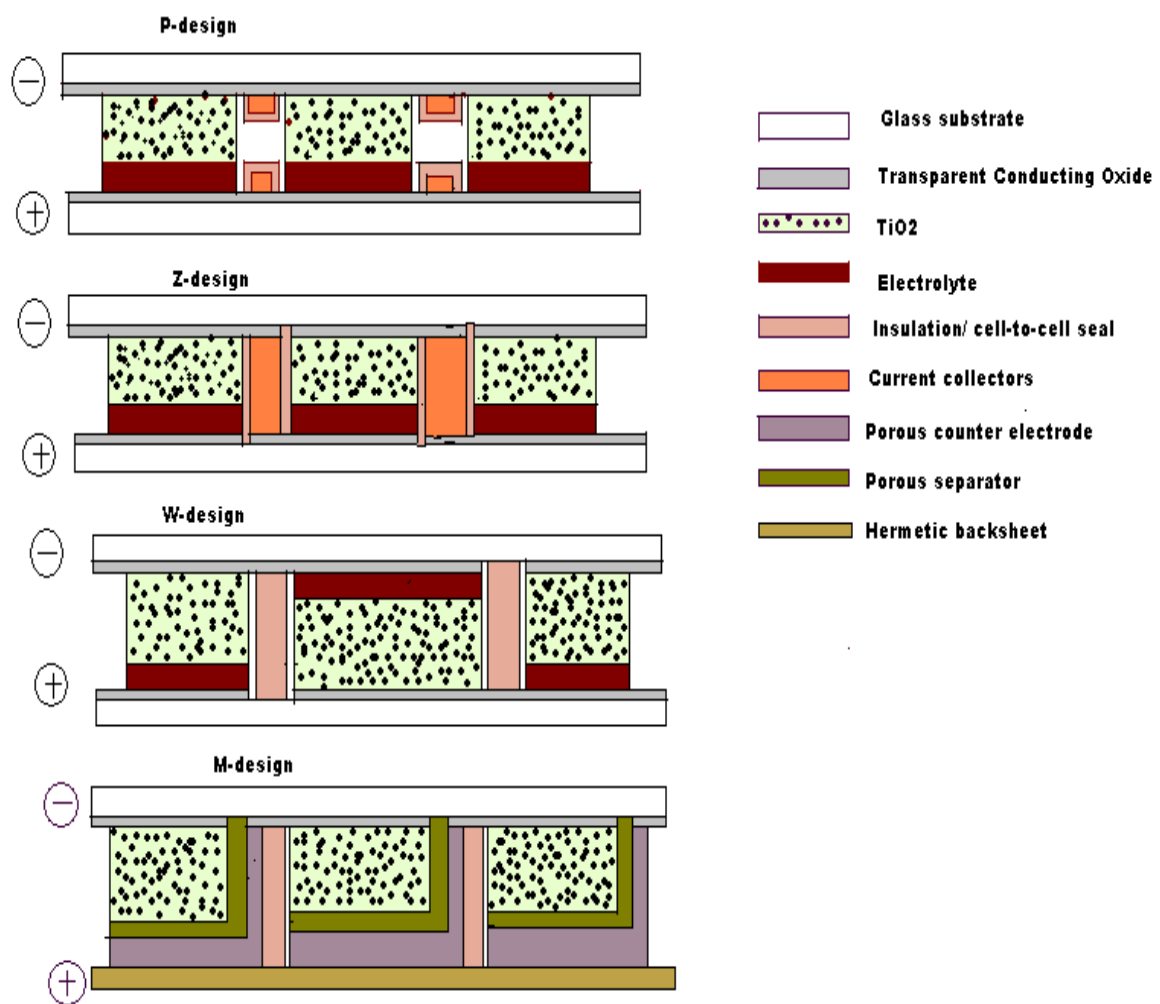
Figure 1. 11   DSSC module designs

used in Building Integrated Photovoltaics (BIPV) and smaller modules can be used for low density applications like chargers for mobile handsets.

1.4.1 Module designs [55]

There are four main DSSC module designs – P-design, Z-design, W-design, M-design – as shown in fig. 1.11. Each design has its own advantages and disadvantages.

P-design module is a **parallel connected module**. This design offers the advantage of higher performance for the same electrode width when compared with Z-design[55]. However, the design requires more conductive material which can make the panel expensive. **Z-design** has the advantage of short cell-to-cell series connections which enable the use of less conductive, corrosion resistant metals. **W-design** module has the advantage that it does not require additional electrical interconnections, thus leading to lower costs. However, the major disadvantage is that the cells are alternatively front and back illuminated and back illuminated cells have a low efficiency owing to photon absorption by the electrolyte. Moreover, each substrate contains both the anode and the cathode, so optimum processing conditions for each element is compromised. In the **M-design** module, only one conductive substrate is required as the porous counter electrode itself acts as both the catalyst for electrolyte reduction and the current collector. This leads to a significant cost reduction in the components. However, the establishment of a proper connection of the porous counter electrode with the TCO is an issue that needs to be addressed.

1.5 Objective

This thesis presents studies on fabrication and characterisation of TiO_2 based dye-sensitised solar cells. Chapter 1 gives an overview of different photovoltaic cell technologies and a review of the state-of-the art DSSC technology. Chapter 2 describes the techniques used for characterisation of DSSC. Chapter 3 describes the fabrication of TiO_2 based dye-sensitised solar cells. Chapter 4 presents the analysis of measurements obtained by the characterisation techniques. Finally, chapter 5 summarises the work done and suggests directions for future work.

18

Chapter 2

Techniques for electrical characterisation of dye-sensitised solar cells

This chapter describes the techniques, standard reporting conditions and instrumentation used for electrical characterisation of DSSCs. Current-Voltage (IV), Quantum Efficiency (QE) and Impedance Spectroscopy (IS) measurements have been traditionally used to characterize DSSCs. IV measurements yield only the absolute values of current, voltage and efficiency. QE and IS studies allow us to identify the behaviour of DSSCs pertaining to their various components and hence it is possible to deduce the various means of energy losses which affect their efficiency.

2.1 I-V Measurements

I-V curves of solar cells are obtained by exposing the solar cells to simulated sunlight and measuring the electrical parameters using appropriate hardware. The various parameters are listed below.

- **Short-circuit current density**, j_{sc} (mA/cm^2) and **Open-circuit voltage**, V_{oc} (Volts) – the highest possible current and voltage that can be obtained in a solar cell, respectively
- **Maximum power point**, P_{max} (mW/cm^2)
- **Fill factor**, FF – the ratio of the maximum power generated to the product of V_{oc} and j_{sc} . $FF = P_{max} / (V_{oc} \times j_{sc})$
- **Efficiency**, η – the ratio of the maximum power generated to the power incident on a solar cell

The schematic of the I-V curve of a solar cell is shown in figure 2.1
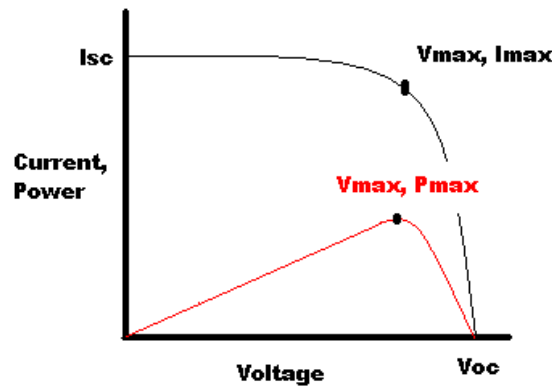
Figure 2.1 Schematic of I-V curve of a solar cell

2.1.1 Instrumentation for I-V measurement

The standard reporting conditions for I-V measurements are an ambient temperature of 25 °C, with a total irradiance of 100 mW/cm^2 at A.M 1.5 conditions and the spectral irradiance characteristics, namely the spectral match, the non-uniformity of irradiance and the temporal instability of irradiance, conforming to the specifications set by IEC 60904-9 Edition 2 (2007), JIS C 8912, and ASTM E 927-05. The performance of a solar simulator is rated as Class A, B or C for each of the above spectral irradiance characteristics. Class AAA is the highest rating for a solar simulator. The values for class AAA standard are listed in table 2.1.

Table 2.1   Spectral irradiance characteristics for Class AAA solar simulator

Organization	IEC	JIS	ASTM
Performance Parameter	60904-9-2007	C 8912	E927-05
Spectral Match (fraction of ideal percentage)	0.75 – 1.25	0.75 – 1.25	0.75 – 1.25
Non-Uniformity of Irradiance	2.00%	$< \pm 2\%$	2%
Temporal Instability	0.5% STI $< 2.0\%$ LTI	$< \pm 1\%$	2%

Oriel Class AAA Solar Simulator was used as light source and a 4-probe Keithley 2420 sourcemeter was used for I-V measurements. Troubleshooting measures are presented in Appendix A.IV.

2.2 Quantum Efficiency

Quantum efficiency measurements are spectrally resolved, i.e., they are measured as a function of wavelength, λ, of light. The measurement is done at short circuit conditions. QE is defined as the ratio of the number of photogenerated carriers to the number of incident photons of a specific wavelength.

$$QE(\lambda) = j_{sc} / qI_0 \qquad \text{(eq 2.1)}$$

where, j_{sc} is the short circuit current density, q is the elementary charge, and I_0 refers to the photon flux.

There are two components of QE: the external and the internal quantum efficiency, EQE and IQE respectively. EQE includes the optical losses due to reflection and transmission of light and can be expressed as the product of three physical processes:

$$EQE\ (\lambda) = \eta_{lh}\ (\lambda) \times \eta_{inj}\ (\lambda) \times \eta_{col}\ (\lambda) \qquad \text{(eq 2.2)}$$

where, $\eta_{lh}\ (\lambda)$ is the light harvesting efficiency of the sensitised oxide layer, $\eta_{inj}\ (\lambda)$ is the efficiency of electron injection from the sensitiser into the oxide and $\eta_{col}\ (\lambda)$ is the electron collection efficiency. EQE is also referred to as incident photon to electron conversion efficiency (IPCE). IQE accounts for the last two terms only.

$$IQE\ (\lambda) = \eta_{inj}\ (\lambda) \times \eta_{col}\ (\lambda) = EQE\ (\lambda) / \eta_{lh}\ (\lambda) \qquad \text{(eq 2.3)}$$

While measuring QE of solar cells, it is important to adjust the cell position such that the incident light falls within the active area of the solar cell. Otherwise, QE will be underestimated because j_{sc} decreases while I_0 remains the same.

In DSSC, QE measurements are useful for studying the behaviour of the adsorbed dye on the photoanode. QE values of DSSC are high near the absorption maximum for a dye. For a state-of-the-art DSSC with N719 dye, the absorption max occurs at 540 nm and the IPCE is more than 80% [56]. This is shown in figure 2.2. Cells which exhibit low IPCE have high charge recombination.
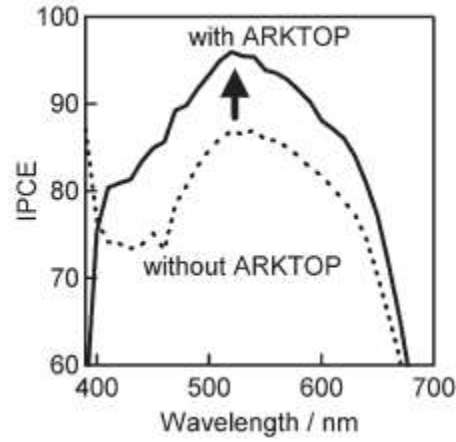
Figure 2.2 DSSC with IPCE more than 80% at absorption max λ=540 nm [56]

2.2.1 Instrumentation for QE measurement

The measurement set up for a single-beam system is shown in figure 2.3. Chopped monochromatic light is first directed onto a calibrated reference cell with a known EQE which is followed by the test cell during the second scan. Two lock-in amplifiers with variable transimpedance gain measure currents j_{cell} and j_{ref} separately and convert and amplify them to voltage signals v_{cell} and v_{ref}, respectively. The ratio v_{cell}/v_{ref} is calculated and is used to determine the EQE of the test cell.

$$EQE\ (\lambda\ )_{cell} = EQE\ (\lambda\ )_{ref} \times (v_{cell}\ /\ v_{ref}) \qquad (eq\ 2.4)$$

The wavelength dependent quantum efficiency of the cells was measured using a Newport IPCE/QE kit. The system consists of the following parts:

i)   a 285 W Xe arc lamp as the source of white light, 300–1100 nm

ii)   a chopper to chop light

iii)   a monochromator with two gratings

iv)   a wavelength filter with 3 filters

v)   a silicon detector head with variable time constant and transimpedance gain; calibrated in the range 200–1100 nm

vi)   a test cell connected to a lock-in pre-amplifier with variable time constant and transimpedance gain

vii)   Merlin® to control the chopper and also to power the detector and the amplifier

viii)   a computer system connected to the above parts except the lamp. The system contains the Tracq Basic® software to control the operation of the parts and to perform calculations.

There are three variable parameters in this measurement, namely the chopper frequency— 8–110 Hz, the time constant— 0.01–100 sec, and the integration time; their influence on quantum efficiency was also studied. There is a fourth parameter which is the gain of the detector and pre-amplifier in the range $10^4 - 10^9$ V/A. The operating instruction manual states that higher gain values could damage the amplifier. So, the value of the gain was fixed at 10^4 V/A.

Chopper frequency:

Quantum efficiency is inversely proportional to the chopping frequency f. At low frequencies, there is sufficient time for the cell to build a current during illumination and also for the current to decay during the dark period, whereas at high frequencies, the cell does not reach its full potential owing to a rapid change in illumination. This results in a lower quantum efficiency as compared to that obtained at low frequencies, as shown in figure 2.4.

Time constant and integration time

There is an optimum value for the time constant and the integration time that allows us to record the true behavior of cells. The graphs for the same are presented in figure 2.5 (a) – (b).

24
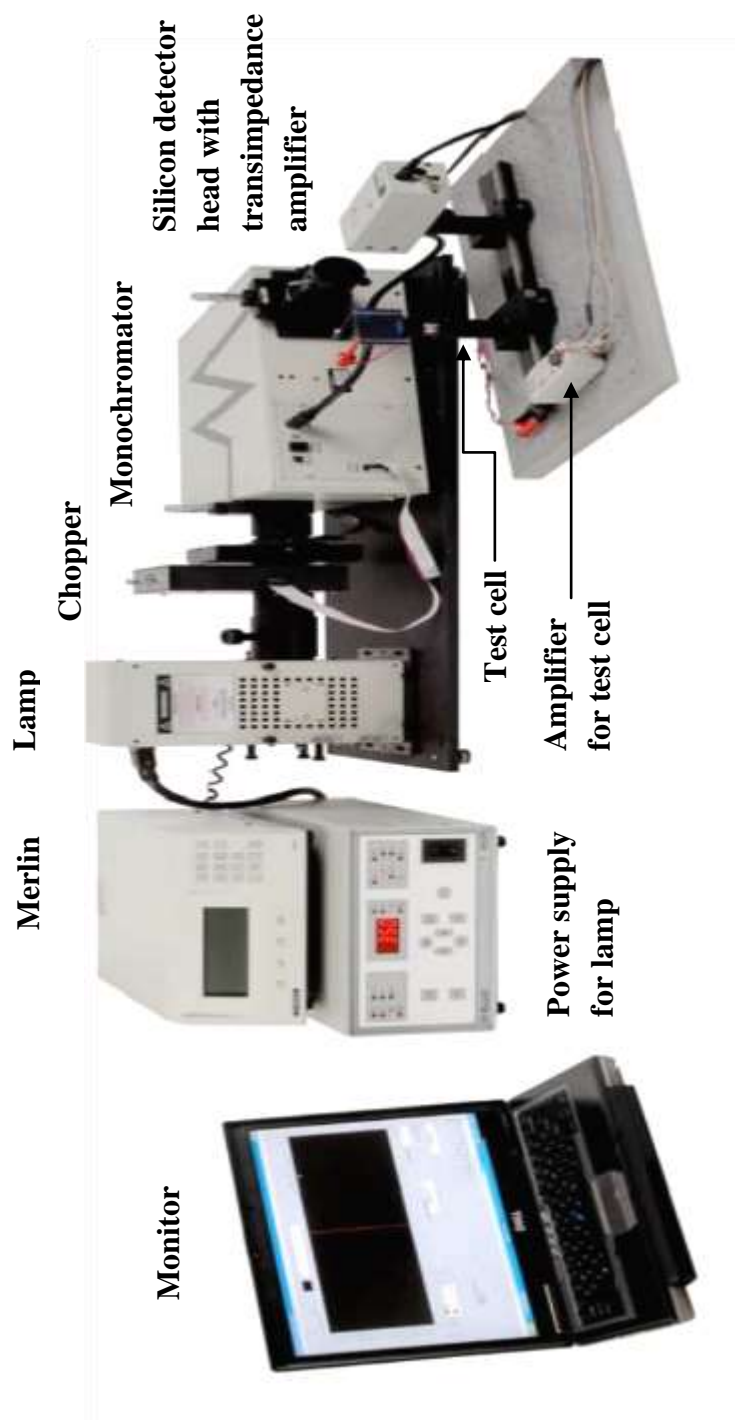
Figure 2. 3 Measurement setup for QE – Newport IPCE/QE kit

Dependency of QE on chopper frequency
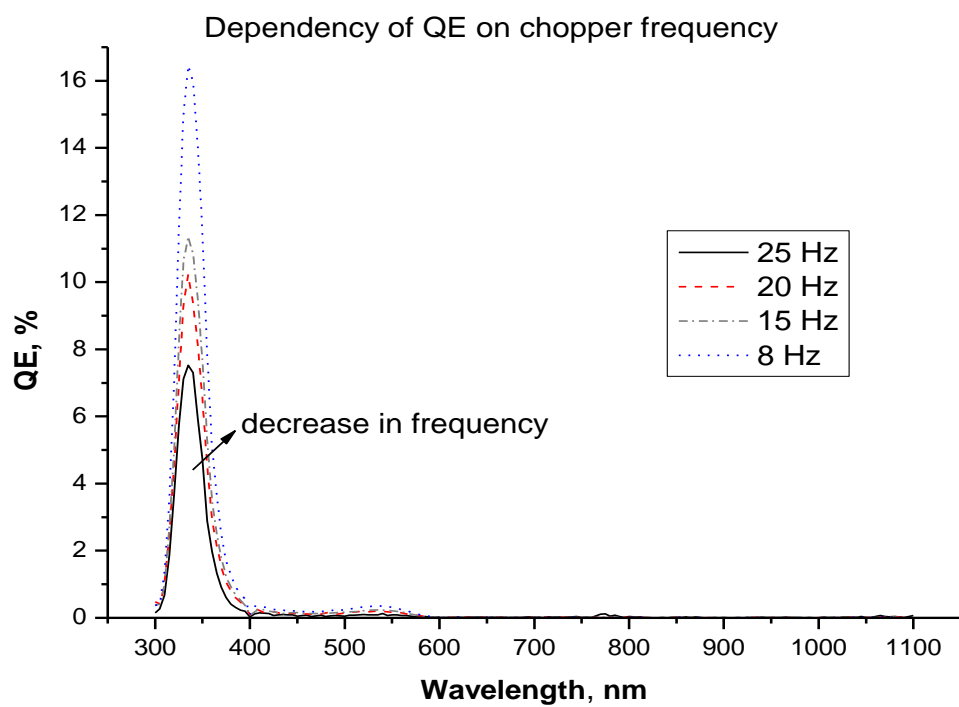
**Figure 2.4 Graph showing the effect of chopper frequency on QE.
QE is high at low frequencies.**
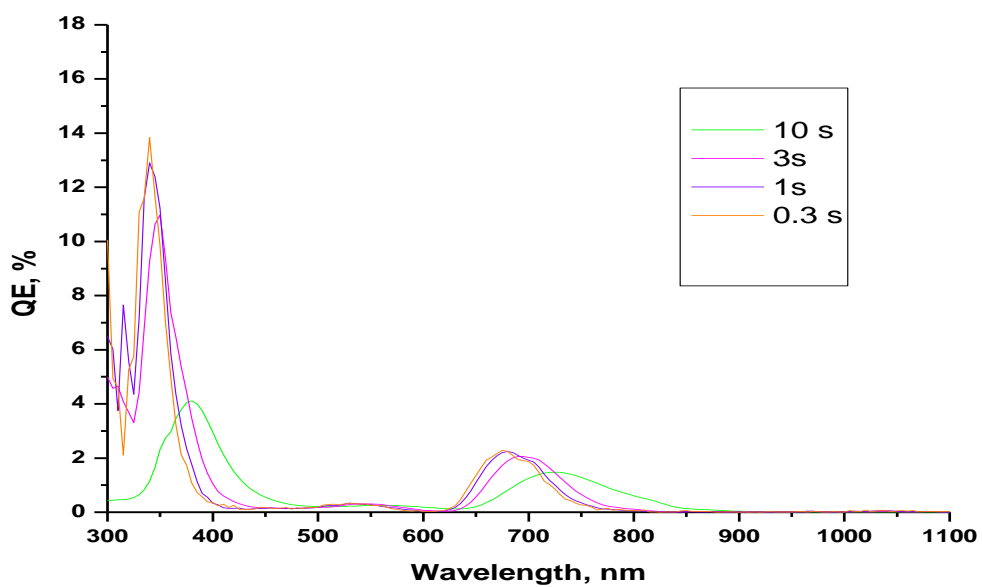
Figure 2.5(a) Graph showing the variation of QE with time constant.
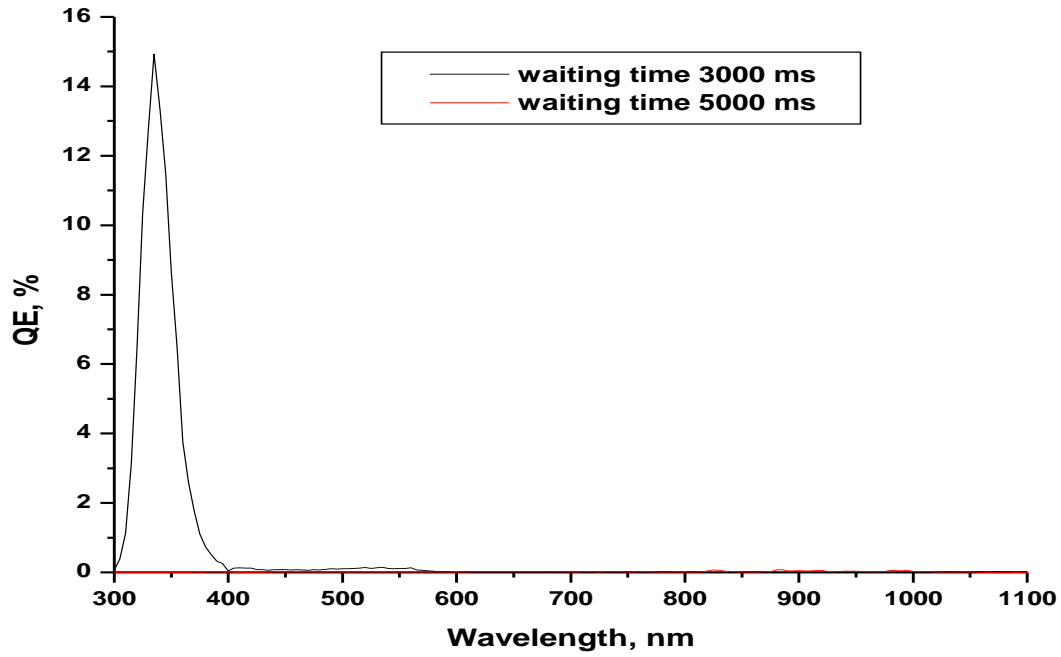
Figure 2.5(b) Graph showing the variation of QE with waiting time. QE response is close to zero for a waiting time of 5000 ms.

So, for the QE measurement, the chopper frequency was set at 8 Hz, the time constant was 1 sec, the integration time was 3 sec and the gain was set at 10^4 V/A.

The procedure for QE measurements and troubleshooting of the same is described in Appendix A.III.

2.3 Electrochemical Impedance Spectroscopy

Impedance spectroscopy (**IS**)[57],[58] is done in a system with electrical components. It consists of a measurement of the AC electrical current, $\hat{J}(\omega)$, at a certain angular frequency, ω, when a certain AC voltage $\hat{E}(\omega)$ is applied to the system, or vice versa, a measurement of $\hat{E}(\omega)$ at an applied $\hat{J}(\omega)$. The impedance is given as

$$Z(\omega) = \hat{E}(\omega) / \hat{J}(\omega) \qquad \text{(eq 2.5)}$$

The symbol ŷ over a quantity y indicates that ŷ is:

    i)   the complex amplitude of a sinusoidal (AC) perturbation of y and

    ii)   a small perturbation

The magnitude of ŷ is chosen such that the impedance is linear, i.e., $\hat{J}(\omega)$ is linear with $\hat{E}(\omega)$ or vice versa, so that $Z(\omega)$ is independent of the amplitude of perturbation. Typically, this amplitude is in the range of 5 mV – 10 mV. The IUPAC convention for representing impedance is Z = Z' + iZ" where Z' and Z" are the real and imaginary components of the impedance, respectively.

During an impedance measurement, the system is ideally kept at a fixed steady state by maintaining constant temperature, illumination intensity, etc., and $Z(\omega)$ is measured by scanning over a range of frequencies from 1 mHz to 1 MHz with 10 – 12 measurements per decade. By scanning over a range of frequencies, we obtain a changing response– the impedance spectrum– that can be treated by several methods— analytical, numerical, visual inspection— in order to provide the physical picture of the dynamics of the system; this can be modeled using resistances, capacitances, etc. When the frequency, ω, is very low, we are close to steady state conditions and obtain exactly the DC resistance, $\mathbf{R_{dc}}$.

$$\mathbf{Z(0) = E(0) /\ J(0) = R_{dc}} \qquad \text{(eq 2.6)}$$

However, when ω becomes higher, certain processes in the system are unable to respond to the faster applied perturbation. $Z(\omega)$ therefore contains contributions from processes happening faster than the current frequency ω being considered. The impedance spectrum so obtained is checked for consistency with the Kramer's-Kronig (KK) relations. KK relationship relates the real and imaginary parts of the impedance obtained experimentally. The equation is given by the formula

$$\qquad \text{(eq 2.7)}$$

$$\boldsymbol{Im\ Z(\omega) = \frac{2\omega}{\pi} \int_0^\infty \frac{Re\ Z(x) - Re\ Z(\omega)}{x^2 - \omega^2} dx}\ [59]$$

In practice, the frequency range is finite, and so, the equation is approximated as

$$\boldsymbol{Im\ Z(\omega) \approx \frac{2\omega}{\pi} \int_{xmin}^{xmax} \frac{Re\ Z(x) - Re\ Z(\omega)}{x^2 - \omega^2} dx}\ ^{[59]} \qquad \text{(eq 2.8)}$$

where x is the frequency, with *xmin* and *xmax* being the lowest and the highest frequency in the experimental frequency range. The theoretical values calculated from the equation are compared with the values obtained experimentally. When the experimental values satisfy the KK relations, the system is said to be stable to the applied AC perturbation; otherwise the data is discarded. Non-conformity to KK relations can be due to errors in the data acquisition procedure of the instrument[59] .

In the field of electrochemistry, impedance spectroscopy is a useful tool to investigate interfacial charge transfer events, such as those occurring in fuel cells, corrosion of iron, etc. This technique uses the three-electrode setup for the analysis of an electrochemical cell. An electrode is a conducting or semiconducting solid in contact with an electrolyte solution. The three electrodes are the working electrode (WE), the counter electrode (CE) and the reference electrode (RE). **Working electrode** is the electrode where reactions are being studied. **Counter electrode** is the electrode that completes the current path in the cell. In most experiments, the CE is simply a current source or sink, and so relatively inert materials like graphite and platinum can be used. **Reference electrode** serves as a reference for potential measurements. The reference electrode is placed in between the WE and CE. The WE and RE constitute one half of the cell; the CE and RE form the other half of the cell. An ideal reference electrode should be reversible and reproducible. This implies that the species which can cross the phase boundary of the reference electrode should exist in equilibrium in both the phases of the half cell, and this equilibrium should not be disturbed during the measurement. However, this ideal case is difficult to realise. So, for practical purposes, a conductive material which exhibits only a small deviation from the ideal case for the experiment in consideration is chosen as the reference electrode. In an electrochemical system, the following elements are used to model the different characteristics observed in an impedance spectrum.

- Resistor, **R** –   –⋀⋀⋁–   – its impedance is independent of the frequency of perturbation. It has only the real part in the impedance spectrum. $Z = R$. The unit is Ω.

- Capacitor, **C** – ╫ – its impedance is dependent on the frequency. It has a purely imaginary part in the impedance spectrum. $Z = 1/(i\omega C)$. Voltage lags the current; therefore phase angle θ is negative. The unit is Farad, **F**.

- Constant phase element (CPE), $\mathbf{Q_n}$ – 《 —— for electrodes having a rough surface, C is replaced by CPE. $Z = (i\omega)^{-n}/ Q_n$. The value of Q is represented using $\mathbf{Y_0}$ and **n**, where $Y_0 = Q_n$. The unit of Y_0 is **Siemens.sec^n**

- Warburg element, W – this is typically used when there is electrolyte diffusion to the counter electrode.

In a typical DSSC, the dyed-TiO_2 film coated on a transparent conducting substrate is the working electrode as photoexcitation of the dye and the injection of the excited electrons into the conduction band of TiO_2 occur here. Platinum coated on another transparent conducting substrate is the counter electrode and is also a catalyst for the reduction of I_3^- ions to I^- ions. The gap between the working and the counter electrodes is in the range of $25 - 60$ μm. So, it is not possible to introduce the reference electrode in the electrolyte in this gap. Hence, the setup reduces to a two-electrode system. The electrochemical workstation used for the IS measurement does not recognize the two-electrode set up; so the reference electrode is also connected to the Platinum electrode.

When a DSSC is illuminated and connected to the IS recording instrument, the DC voltage applied to the cell is the open-circuit voltage and the perturbation is, say, a 5mV sinusoidal AC signal. At open-circuit under illumination, the net current through the cell is zero. All the photo-injected electrons in the TiO_2 conduction band are intercepted by the I_3^- ions. The oxidized dye is regenerated by I^- ions. The counter electrode is kept at equilibrium, because there is no net current flowing through it. When an AC perturbation is applied, there is net electron flow through the external circuit or a net electron flow within the cell, as shown in figure 2.6 [60]. These processes manifest themselves as impedances of varying magnitude, being characteristic of the different components of the cells.
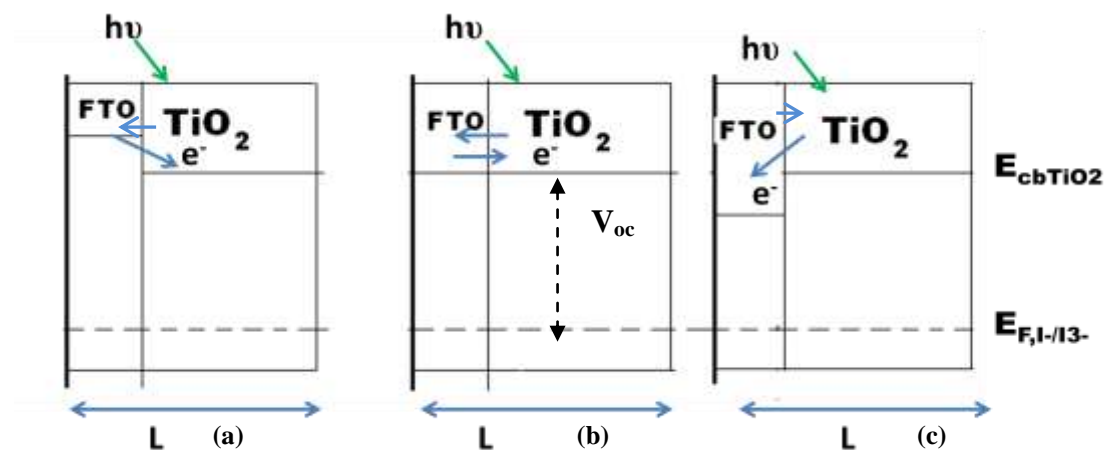
Figure 2.6 Schematic mode of photoanode at different voltages. (a) E >V_{oc} —net electron flow into the cell. (b) E = V_{oc} — net current is zero. (c) E < V_{oc} — net electron flow in the external circuit . L is the thickness of the films.[60]

The figure 2.7(a) shows the impedance spectrum of a typical DSSC and figure 2.7(b) shows its equivalent circuit. There are two semicircles. The smaller semicircle occurs in the high frequency range of $10^5 – 10^6$ Hz and represents the charge transfer at the Pt/I_3^-/I^- interface; the bigger semicircle occurs in the frequency range of $1 – 10^4$ Hz and represents the charge transfer at the TiO$_2$/ I_3^-/I^- interface and the third arc in the low frequency range is due to the diffusion resistance of the electrolyte. The series resistance **Rs** includes the sheet resistance of FTO, the resistance of the counter electrode and the resistance of the electrolyte. **Rct** is the charge transfer resistance and **C** is the capacitance at the respective electrode/electrolyte interface. In case of DSSCs with acetonitrile based solvents, the third, low-frequency arc merges with the bigger central semicircle, owing to the high diffusion co-efficient in acetonitrile [61].
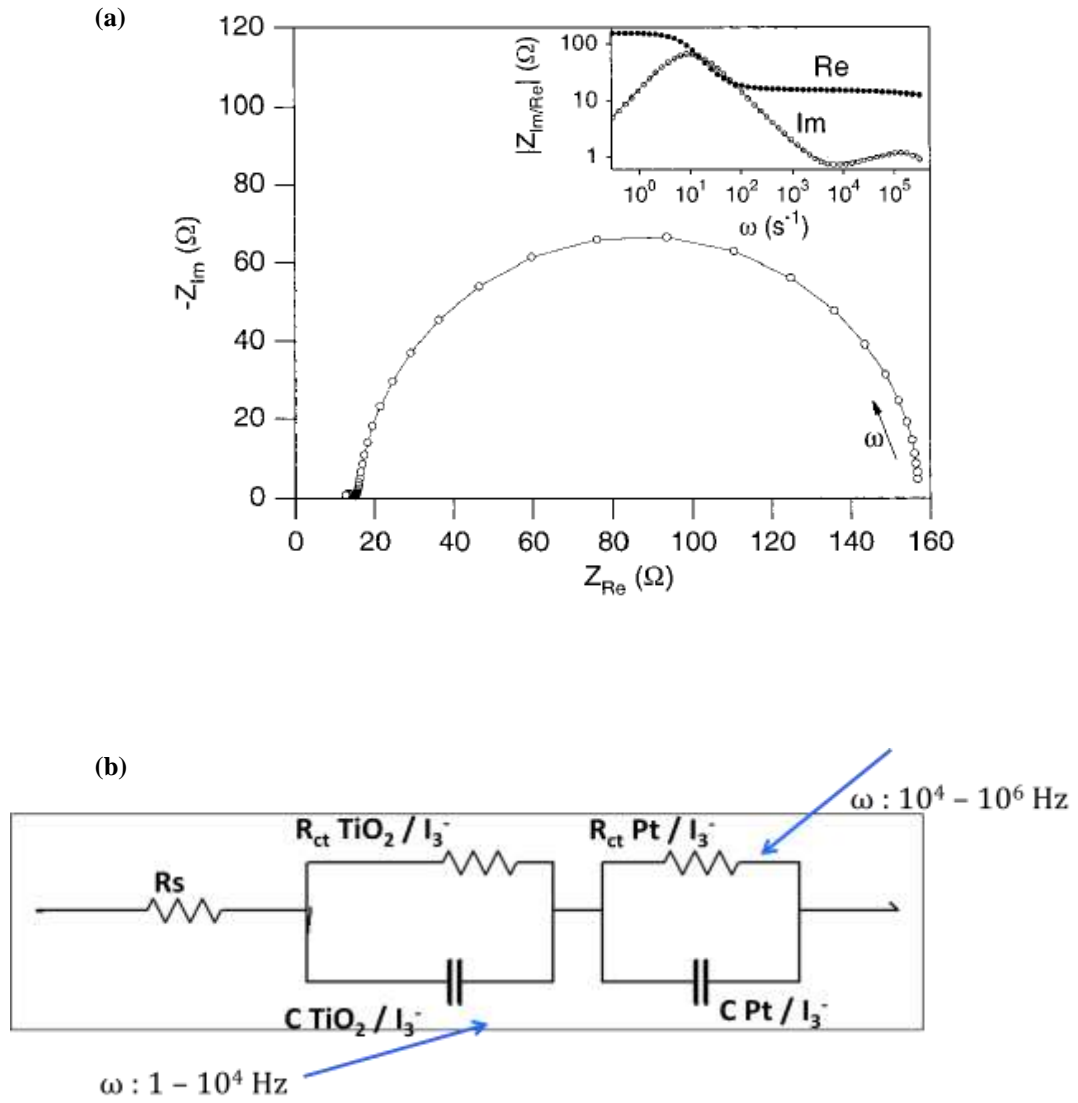
Figure 2.7(a) Impedance spectrum of a typical DSSC[62]. b) Equivalent circuit of the DSSC

2.3.1 Instrumentation for IS

The figure 2.8 shows the setup for IS measurement. Oriel AAA solar simulator was used as the light source and CHI 608D electrochemical analyser was used for impedance measurements. The working electrode was connected to the TiO_2 electrode; the counter and reference electrodes to the Pt electrode. The perturbation was a 5 mV sinusoidal AC signal above the open circuit potential; the scan range was $1–10^5$ Hz with 12 components per frequency decade. The equivalent circuit was modeled to fit the impedance spectrum using in-built software in CHI 608D. The consistency of the experimental impedance data was checked by using the electrochemical fitting software ZSimpwin. The procedure for taking IS measurements and troubleshooting is described in the sections A.I and A.II of Appendix A.

(a)

(b)

(c)

(d)

Light source

Working electrode

Reference electrode

Counter electrode

Electrochemical WorkStation
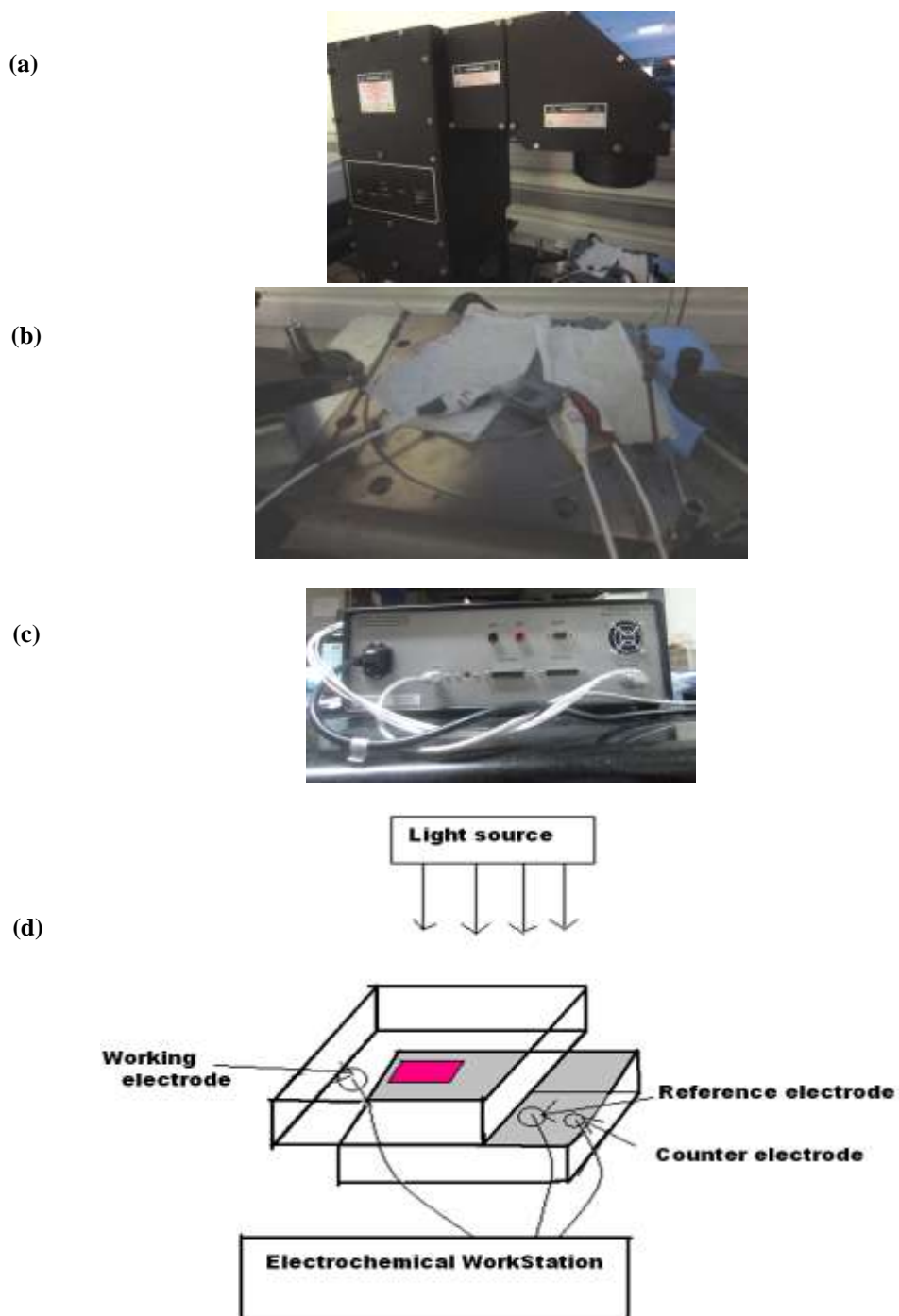
Figure 2.8 Setup for IS measurement. (a) Oriel AAA solar simulator. (b) DSSC cell placed on solar simulator cell stage and connected to three electrodes. (c) Electrochemical workstation CHI 608D for measuring IS. (d) Schematic diagram of the set up

Chapter 3

Fabrication of TiO$_2$ based dye-sensitised solar cells

This chapter describes the procedure for the preparation of TiO$_2$ based dye-sensitised solar cells. Two different procedures were followed— one for making low cost cells and the other for making high efficiency cells. The low cost cells were prepared without any organic additives in the TiO$_2$ film and using Eosin-Y as the dye and carbon soot as the counter electrode. The high efficiency cells were prepared using organic additives in the TiO$_2$ film, with N719 as the dye and Platinum as the counter electrode.

3.1 Dye-sensitised solar cells prepared without organic additives for TiO$_2$ paste

3.1.1 Materials used

Ethanol, titanium tetraisopropoxide, P25 TiO$_2$ powder with a specific surface area of 50 ± 15 m^2/g were used for the preparation of the TiO$_2$ paste for TiO$_2$ films. P25 TiO$_2$ was received as a gift from Evonik Degussa. The substrate was an FTO glass slide with a sheet resistance of 15 $\Omega/\square$ purchased from Solaronix. A dye solution consisting of 0.5 mM Eosin-Y in ethanol was used for staining the TiO$_2$ films. (The structure of Eosin-Y is shown in figure 3.1). The electrolyte was a solution of 0.5M KI, 0.05 M I$_2$ in acetonitrile. The dye and the electrolyte solutions were stored in air-tight glass vials wrapped by aluminium foil and sealed tightly by parafilm to prevent the ingress of moisture and they were kept in a dessicator in the dark to avoid exposure to light. Carbon soot and platinum were used as the counter electrodes. Glass beakers, glass pipettes, plastic spatulas and plastic forceps were used for handling the materials. Steel items were avoided as they might rust and rust could

contaminate the samples. In cases where plastic spatulas could not fit into the containers, materials were transferred into weighing bottles by tapping the container. In order to minimize contamination, the materials were always directly transferred into weighing bottles and no butter paper was used. Glass items were cleaned using detergent, tap water, distilled water, toluene, acetone and ethanol in order. Plastic items were cleaned using detergent, tap water, distilled water and ethanol in order.

FTO glass slides measuring 5 cm * 5 cm were cut into smaller glass slides of sizes 2.5cm * 2.5cm. A diamond pencil was used for drawing lines on glass and the glass slides were broken along the lines manually. Lines were marked on the FTO-free side. The glass slides were cleaned by ultrasonication for 5 minutes each in toluene, acetone and ethanol. The glass slides were then treated with ozone for 15 minutes in a UV ozone chamber and were immediately used for cell preparation.

3.1.2 Techniques for characterisation

The dye solution was characterised by UV-Vis absorption spectra; the films were characterised by optical profilometer, SEM and UV-Vis absorption spectra; the finished cells were characterised by QE, IV and EIS measurements. The films used for UV-Vis characterisation and cell characterisation were different. The films which had been exposed to light during the measurement of UV-Vis absorbance undergo oxidation. So, for the purpose of the cell assembly, a freshly dyed-TiO_2 film which had not been exposed to UV-Vis light was used.
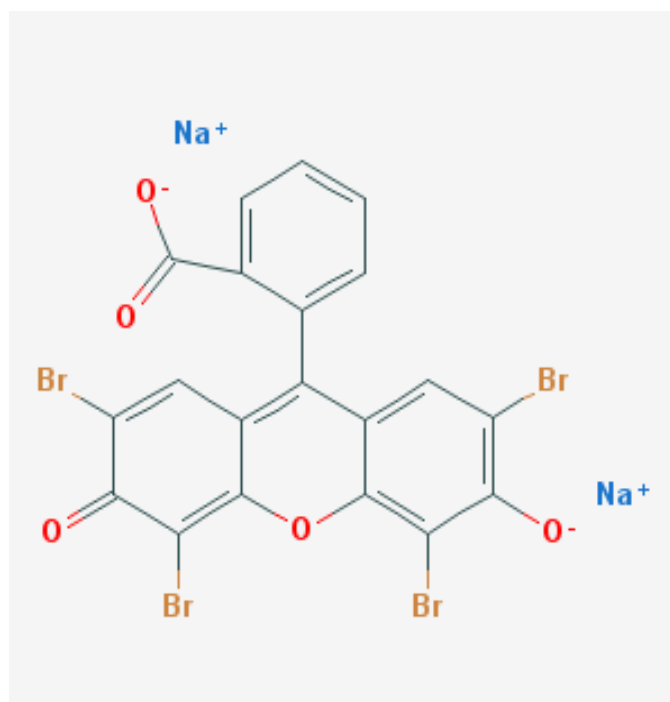
Figure 3.1 Structure of Eosin-Y [63]
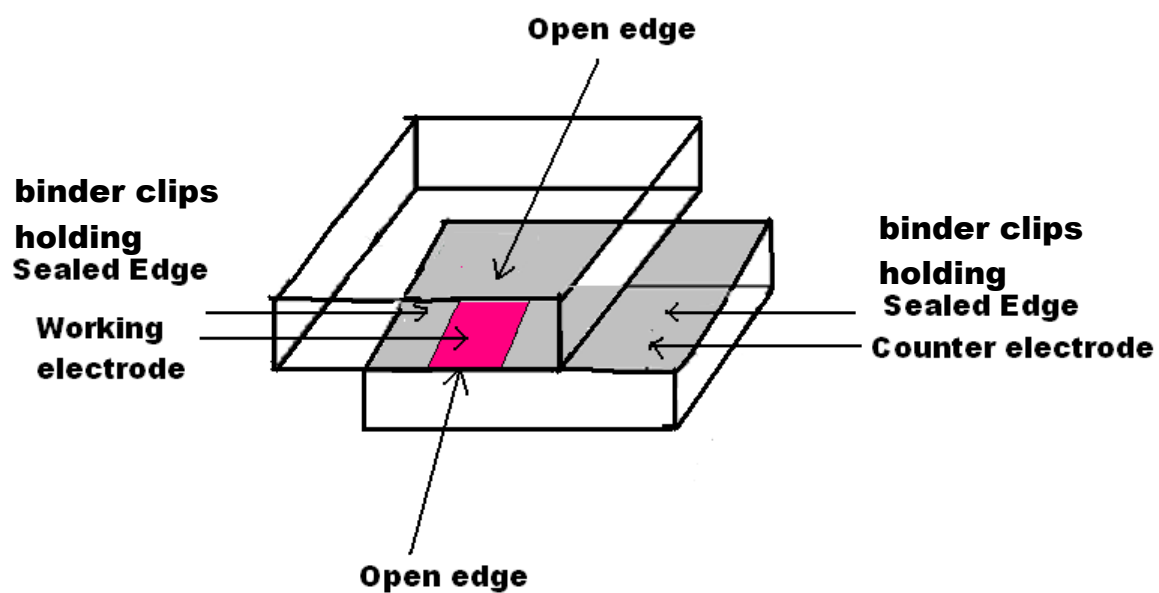
Figure 3.2 Cell design of cells prepared without organic additives in TiO$_2$ film.

3.1.3 Fabrication of cell

The active area of each cell was 1 cm^2. The cells were made following the procedure of Takechi et al[64]. The figure 3.2 shows the design of the cell. A TiO_2 suspension in ethanol was prepared with or without the addition of titanium tetra isopropoxide. 1 gm of TiO_2, 4.3 ml of ethanol with or without 0.143 ml of titanium tetra isopropoxide were mixed together in a glass beaker and sonicated in an ultrasonic bath. The suspension was spread on the FTO glass substrate over an area measuring 1cm * 1cm as one single coating using a glass slide. The area of the film was chosen such that one edge of the TiO_2 film was along the edge of the FTO glass substrate. The glass slide was covered with cello tape at the spreading edge to prevent the bare rough edge of the glass slide from scratching the FTO glass substrate. The region around the spreading area was masked with 50 μm thick Claro® cello tape prior to spreading. Cello tape serves as a reference for the thickness of the films. The film was allowed to dry for 2 min, the cello tape was removed and the film was sintered at 150 °C for 30min in a hot air oven. It is common knowledge that sudden exposure to high temperatures results in an uneven thermal stress and causes breakage of glass and cracking in films. So, the temperature was ramped up from 25 °C to 150 °C in 15 min at the rate of 10 °C/min. This was the least ramping rate available in the instrument. All the films prepared using Ti(OPr)$_4$ peeled off the substrate, while films prepared without Ti(OPr)$_4$ adhered to the substrate only in some trials. These films too had cracks as observed figures 3.3(a) – (b). The thickness of the films was in the range of 30–50 μm as shown in figures 3.3(a) – (b). For the dye sensitization step, the film was reheated to 100 °C to remove adsorbed water and immediately immersed in 0.5 mM Eosin-Y solution in ethanol in a glass beaker for 24 hrs. The glass beaker was covered with aluminium foil and tightly sealed with parafilm to prevent the ingress of moisture and stored in a dessicator in the dark to prevent exposure to light. The dyed TiO_2 film was taken out of the dye solution and rinsed with ethanol to remove unadsorbed dye molecules and the cell was immediately assembled. The two opposite edges around the TiO_2 film were masked with cello tape measuring 50 μm, leaving the other two opposite edges free for introducing the electrolyte. Cello tape being an

insulator prevents short circuiting of the bare working electrode and the counter electrode when they are clamped together. The TiO_2 working electrode and carbon soot counter electrode or platinum counter electrode were clamped together with the help of binder clips. The electrolyte was introduced into the cell through the free edge of the assembled cell. The electrolyte spread to the entire active cell area by capillary action.

3.1.4 Preparation of counter electrode

Carbon soot or sputtered Platinum was used as the material for the counter electrode. Carbon soot was deposited on the FTO side by holding the glass over a candle flame for 10 sec. Platinum of thickness 100 nm was sputtered onto the FTO side in an Anelva RF sputtering unit employing 80W RF power.

3.1.5 Optimization of process conditions

3.1.5.1 Effect of sonication time

Sonication serves the dual purpose of dispersing the TiO_2 particles homogeneously and evaporating ethanol by means of heat dissipation during sonication. Initially the suspension was sonicated for 30 min as mentioned in the procedure. The suspension was however free flowing and no paste was formed as mentioned in the procedure. The suspension was sonicated for another 30 min; still no paste-like consistency was observed. When left for longer periods in the sonication bath, all the ethanol from the suspension had evaporated due to the heat generated by sonication and cracks of TiO_2 film were observed in the beaker itself. So, the time of sonication was fixed at 1 hr.

3.1.5.2 Effect of titanium tetraisopropoxide

In the trials involving $Ti(OPr)_4$, many small aggregates were formed in the suspension. The films made using the suspension had many cracks after sintering. The films also peeled off the substrate. Since the aggregates acted as the centre for origination of the cracks, titanium tetra isopropoxide which was the source of the aggregates was not added in the subsequent trials.

3.1.6 Interpretting optical profilometer images

The figures 3.3(a)–(b) show the thickness at different regions of the edges of the films. The thickness in the interior of the film could not be measured because of the small field of view. The field of view was 1.6 mm * 1.6 mm, whereas the geometrical film area was much larger, 1 cm * 1 cm. The thickness was measured along two edges of the TiO_2 film. It is observed that the film has many cracks near the edge. Also, the height varies along the edge. It is in the range of 30–50 μm. Claro® cello tape of thickness 50 μm was used as the reference for thickness during the preparation of TiO_2 films. So, the sections closer to the edge display a maximum height of 50 μm. Thickness greater than 50 μm indicates that the TiO_2 flakes have not adhered to the surface firmly. The sections away from the edge display lower maximum heights. So, the sections whose edge thickness is less than 50 μm indicate that the portion of the film close to the actual edge observed during the preparation has peeled off the substrate after sintering. From these observations, it can be concluded that the film surface is rough and the geometrical film area does not exactly measure 1 cm * 1 cm.
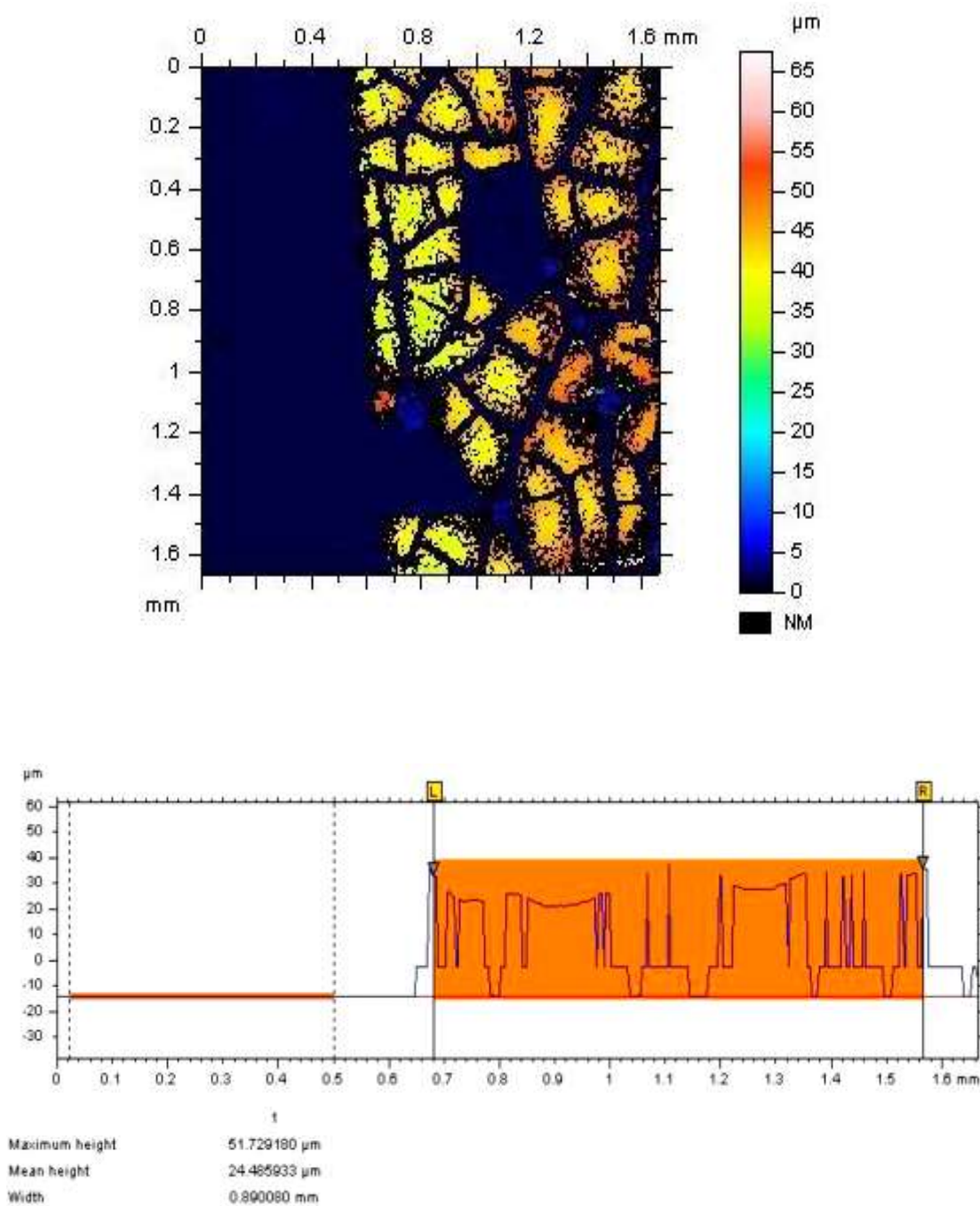
Figure 3.3(a) Cell 1 prepared without the use of organic additives and Ti(OPr)$_4$ – Optical profilometer image showing the thickness of edge 1 of the TiO$_2$ film. The base FTO substrate is at the -14 μm level. The maxiumum height from the base is 51 μm.
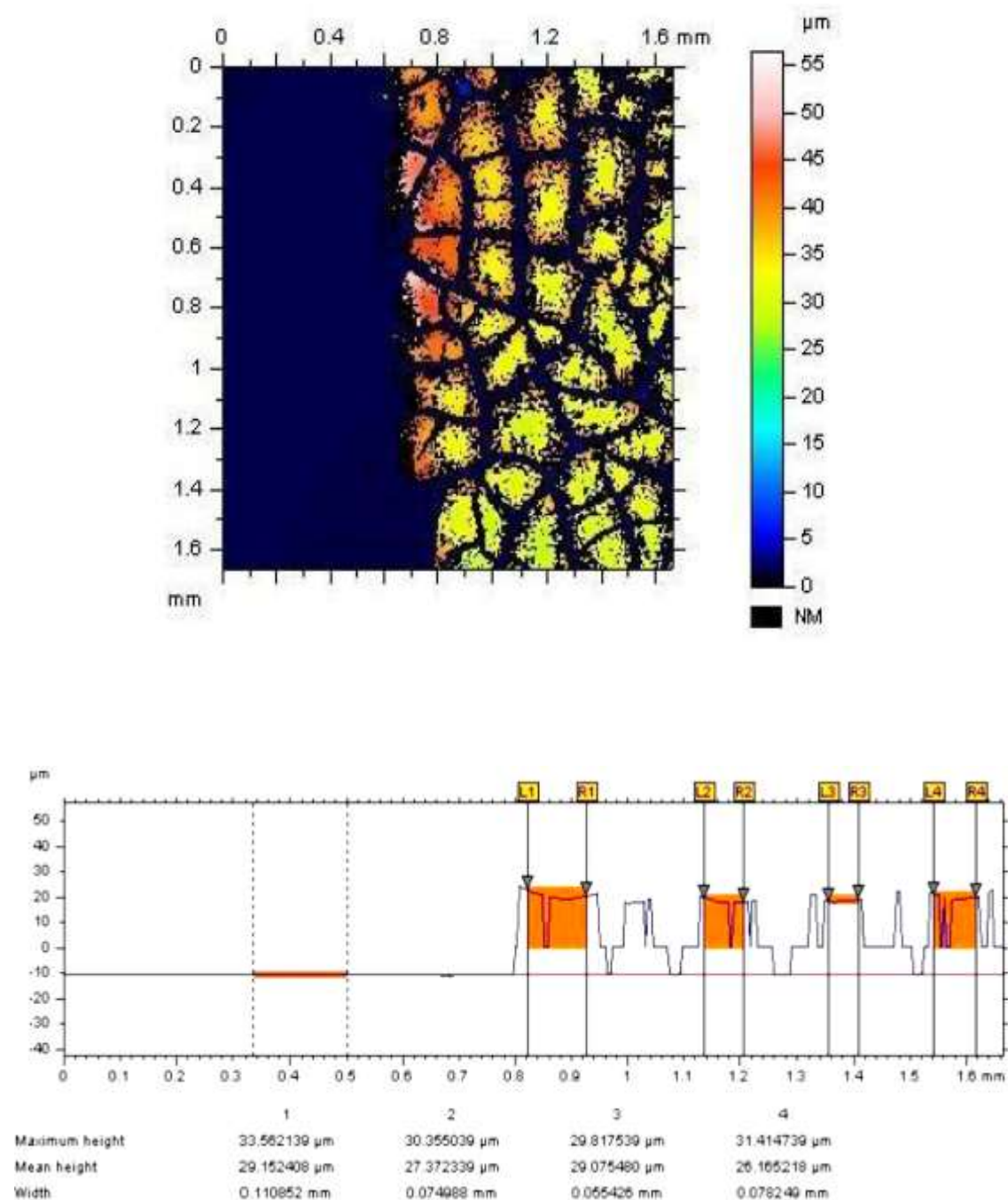
Figure 3.3(b) Cell 1 prepared without the use of organic additives and Ti(OPr)$_4$ – Optical profilometer image showing the thickness of edge 2 of the TiO$_2$ film. The base FTO is at the -10 μm level. The maximum height from the base is 33 μm.

3.2 Dye-sensitised solar cells prepared with organic additives for TiO$_2$ paste

3.2.1 Materials used

The dye-sensitised solar cells were fabricated using Degussa P25 TiO$_2$, sputtered Pt of thickness 100 nm or thermally deposited Pt, fluorine doped tin-oxide (FTO) glass of sheet resistance 15 $\Omega/\square$ and N719 dye purchased from Solaronix. The active area of the cell was a square measuring 1 cm^2. The TiO$_2$ paste was made using P25 TiO$_2$, water, acetic acid, ethanol, ethyl cellulose and terpineol. A dye solution consisting of 0.5 mM N719 in ethanol was used for staining the TiO$_2$ films. The electrolyte was a solution of 0.5 M LiI, 0.05 M I$_2$, 0.5 M tert-butylpyridine in acetonitrile. The dye and the electrolyte components are hygroscopic. So, weighing was done in glove box with N$_2$ atmosphere. Ethanol and acetonitrile were purged with N$_2$ using a sparger to remove any dissolved oxygen or moisture and used immediately for the preparation of the solutions. Staining of TiO$_2$ films and assembly of cells were carried out in a clean room with humidity below 45%.

3.2.2 Techniques for characterisation

The characterisation techniques are the same as those mentioned in section 3.1.2.

3.2.3 Drilling of holes

The figure 3.4 shows the setup for drilling of holes. Holes were drilled on FTO glass substrates before depositing or sputtering platinum. The glass was placed on a stable wooden base covered by lint-free Kim wipes. Lint-free Kim wipes prevent the direct contact of glass with wood and protect it from scratches. Drilling was done from the FTO-free side. The FTO coated side was on Kim wipes. Holes of approximately 1mm diameter, spaced 1 cm apart, were drilled in the FTO glass in a factory or using high speed Bosch drilling tool for glass. The speed was 30,000 rpm. Diamond drill bits of approximately 1 mm diameter were used for drilling holes. Water was used to cool the diamond drill bit while drilling. This prolongs the life of the bit. It was observed

that using the same drill bit to drill more than two holes resulted in blunting of tips and breakage of glass. Therefore a drill bit should be used for only one or two holes.
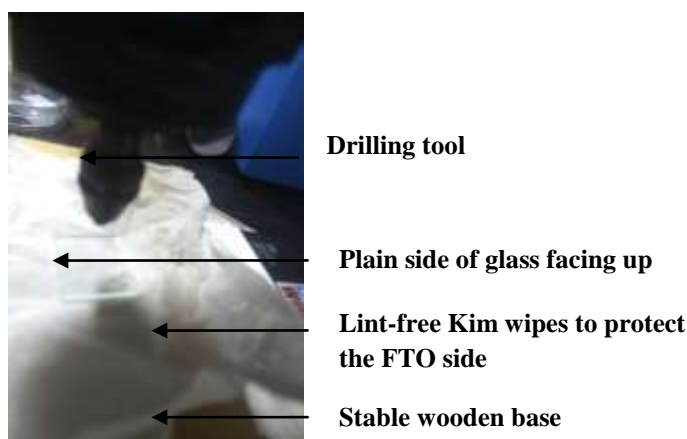
Figure 3.4 Setup for drilling of holes in glass

3.2.3 Cell fabrication

The active area of the cell was 1 cm^2. The TiO_2 paste for the working electrode was prepared by following the procedure of Seigo et al[65]. 3 grams of TiO_2 and 0.16 ml of acetic acid were mixed in a mortar and ground for 1 min. This was followed by addition of 0.17 ml of water and grinding for 1 min. This procedure was repeated five times. To this mixture 5 ml of ethanol was added in 20 steps with each addition followed by grinding for 1 min. The paste was then transferred to a beaker using ethanol. The mixture was sonicated in an ultrasonic bath for 5 min with each sonication cycle consisting of 2 seconds of work followed by 2 seconds of rest. Then, 3.6 grams of terpineol was added and the mixture was sonicated for 5 min. Finally, 0.5 grams of ethylcellulose in ethanol was added and the mixture was sonicated for 5 min. Ethylcellulose should be completely dissolved in ethanol and then added to the mixture. The suspension was placed in an oven to evaporate ethanol. The resulting paste was ground with a pestle. The TiO_2 paste was spread on FTO by spin coating at 1000 rpm for 20 sec. After spin coating, the film was heated to 125 °C. The spin coating followed by heating was repeated three times. Finally the film was sintered at

450 °C for 30 minutes in a hot air oven. The oven temperature was ramped up from 25 °C to 450 °C at the rate of 10°C/minute. This was the lowest setting available in the instrument. The SEM image of the sintered film is presented in figures 3.8 and 3.9. The thickness of two films is shown for representation in figure 3.9 and 3.10. The average thickness of TiO_2 film was 20 – 22 $\boldsymbol{\mu}$m. The cracks found in these films, however, are not as large as the cracks found in the films prepared without organic additives. The counter electrode was sputtered platinum of thickness 100 nm or platinum deposited by decomposition of Platisol.

For the dye sensitization step, the TiO_2 film was reheated to 100 °C for 15 min to remove any adsorbed water and soaked in a 0.5 mM N719 dye solution in ethanol for 24 hours. Prior to cell assembly, the sputtered platinum electrode was sintered at 400°C for 10 minutes in a hot air oven to remove any adsorbed organic impurities. After being removed from the dye solution, the two electrodes were immediately heat-sealed together by means of Surlyn film of thickness 25 $\boldsymbol{\mu}$m placed around the active area. The cell was heat-sealed at a temperature of 100 °C. The cell was allowed to cool and then the electrolyte was introduced into the cell through the holes by means of capillary action. The region around the holes was cleaned using ethanol to remove excess electrolyte. The holes were then sealed with Surlyn film and glass cover slip. The figures 3.5(a) — (d) represent the steps in the assembly of the cells. The assembled cells were then characterized by QE, IV and EIS measurements.

3.2.4 Assembling Surlyn film

Surlyn film serves the dual purpose of sealing and preventing short-circuiting of the two electrodes. The film with the required inner dimensions should be cut out based on the geometry of the TiO_2 film. This implies that the Surlyn film should be prepared before staining the TiO_2 film.

3.2.5 Preparation of counter electrode

The counter electrode Pt was prepared by either thermal decomposition of liquid Platisol® at 385 °C or by sputtering platinum onto the FTO glass in the RF sputtering unit employing 80W RF power. The average thickness of sputtered platinum was 100 nm. The morphology of the sputtered Pt film and the Platisol Pt is shown in figures 3.6 and 3.7 respectively.

3.2.6 Optimization of sealing conditions for cells

In literature, the time used for sealing is 20 seconds. A range of sealing times starting from 20 s – 15 min were followed. The cells with Surlyn film between the electrodes were placed in a hot air oven at 100 °C, with the Pt electrode at the bottom and the dyed-TiO$_2$ electrode at the top. Metallic weights measuring 3 kg were kept on top of the dyed-TiO$_2$ electrode to provide pressure during sealing. The number of weights was limited by the space in the oven. The arrangement was maintained for 20 seconds to 5 min. The figure 3.11 shows the QE measurement of the cell prepared without the optimization of time for sealing. It is observed that the QE is decreasing with time. This is due to the loss of electrolyte due to improper sealing. Therefore, to improve sealing, a different arrangement was used in the subsequent trials. The electrodes were placed on a hot plate instead of an oven and no weights were used. An iron box set at 100 °C was used to heat the glass substrate containing the dyed-TiO$_2$ electrode . The optimum time for sealing was found to be 15 min. After filling electrolyte, the holes were heat sealed within 10 sec to prevent the evaporation of the electrolyte.
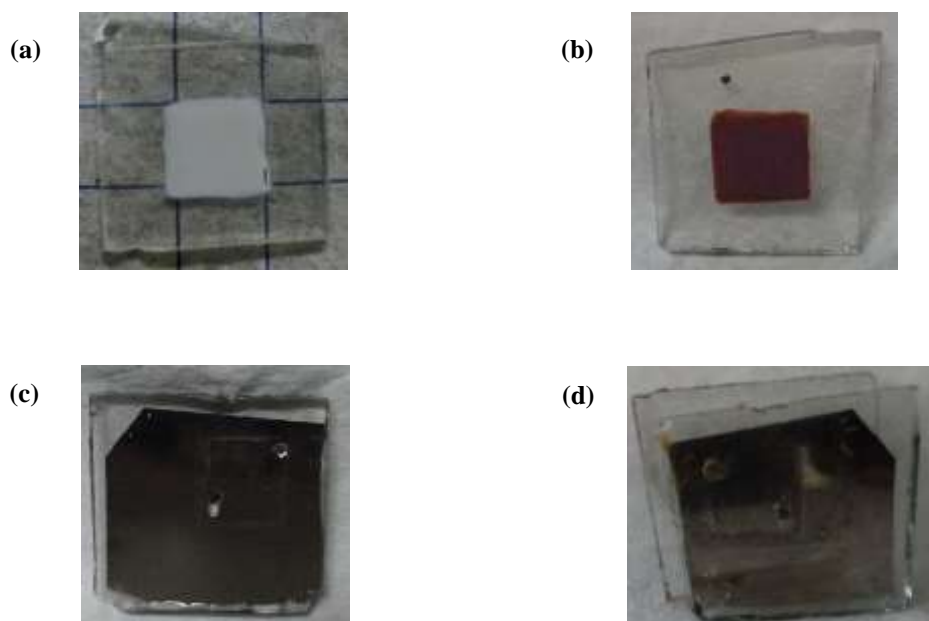
Figure 3.5 Pictures of a) TiO₂ film prepared with organic additives and sintered at 450 °C for 30 min. b) N719 dyed TiO₂ film. c) 100 nm sputtered Pt on FTO. The glass has 1 mm diameter holes for introducing electrolyte in the cell. d) Cell filled with electrolyte and heat sealed with Surlyn film at 100 °C.
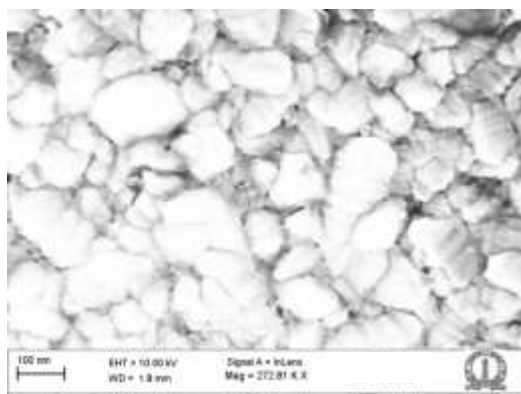
Figure 3.6 SEM image of Pt film sputtered on deposited on FTO glass
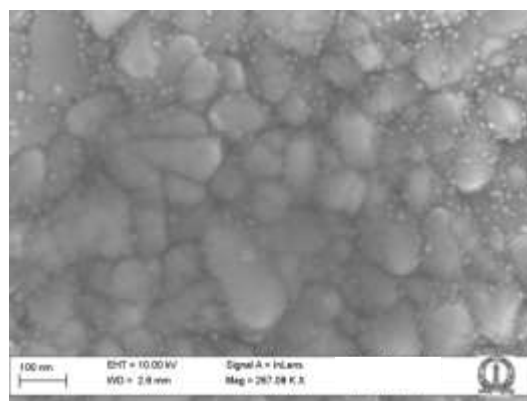
Figure 3.7 SEM image of Pt deposited by thermal decomposition of Platisol on FTO glass. The small white particles are Pt particles.
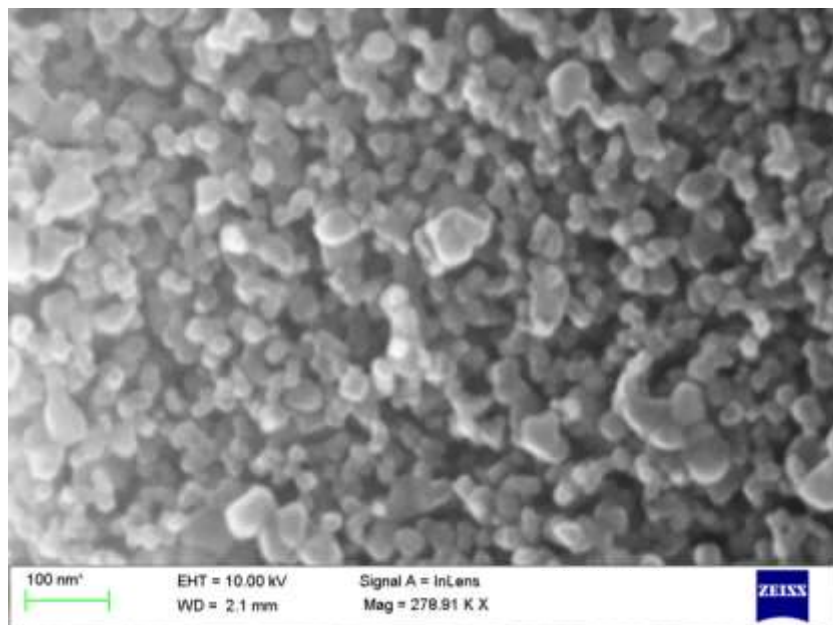
Figure 3.8 TiO$_2$ film prepared with organic additives and sintered at 450 °C .
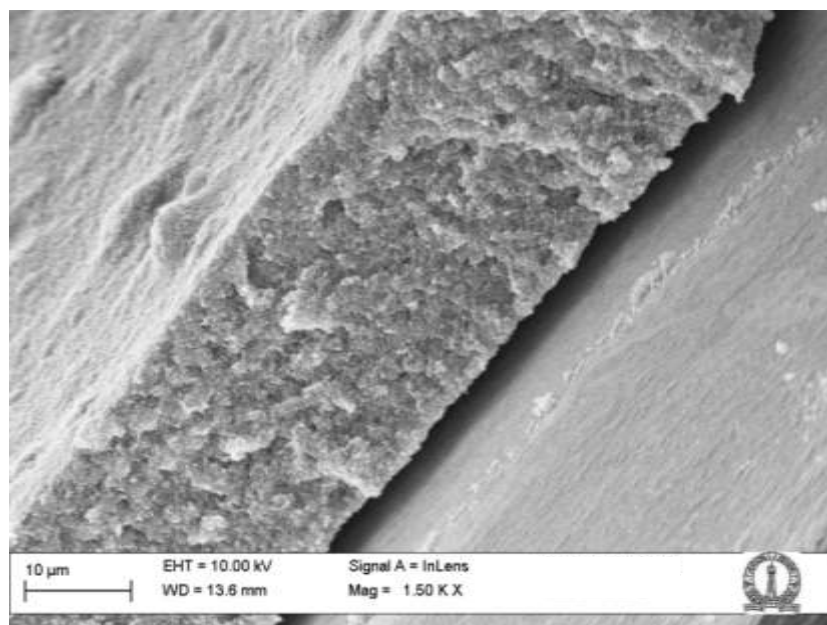
Figure 3.9 Cross sectional SEM image showing thickness of TiO$_2$ film. TiO$_2$ film is viewed at 5°. Thickness is measured normal to the viewing angle. Thickness is ∼20 μm.
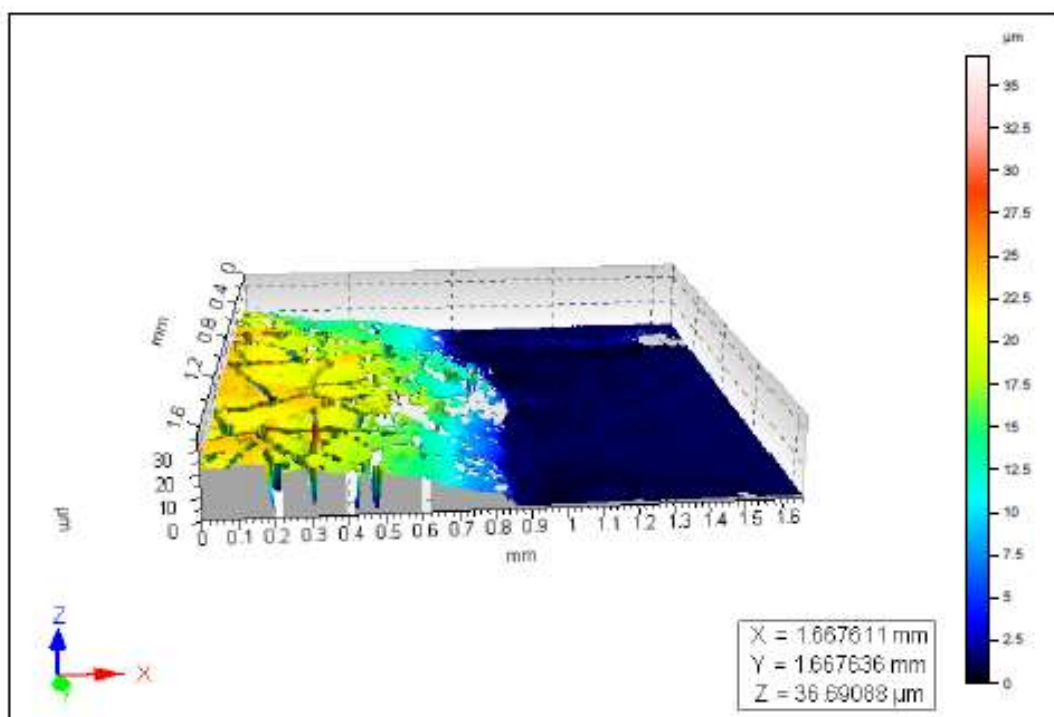
Figure 3.10   3D rendering of optical profilometer image of film 2. The thickness is ≈ 22μm.
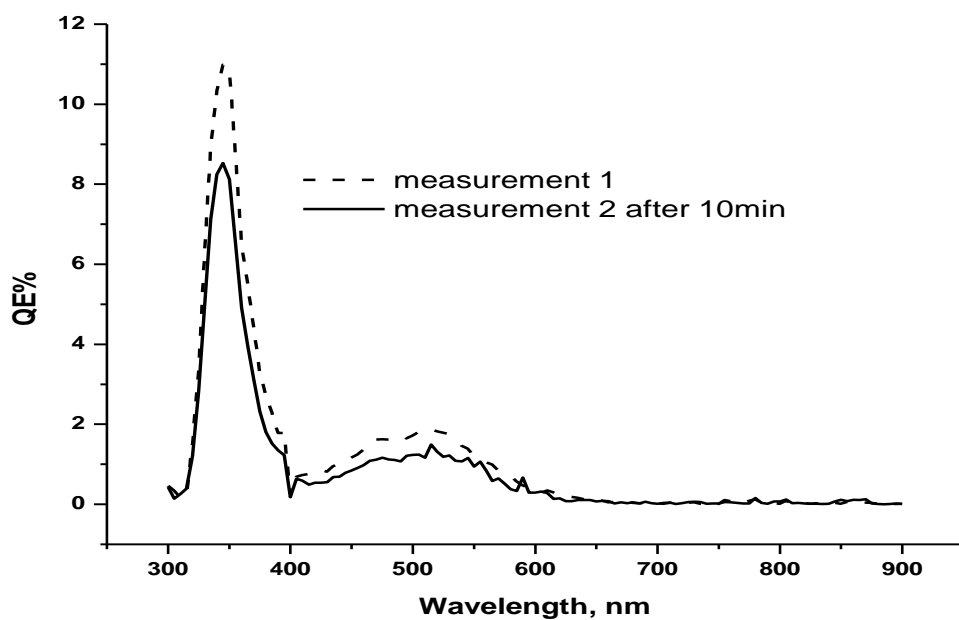
**Figure 3.11 QE values of cell sealed at 100 °C for 5 min in hot air oven.
The decrease of QE values with time suggest that electrolyte is
leaking due to improper sealing.**

Chapter 4

Results and Discussion

This chapter presents the QE, I-V, IS measurements and the sheet resistance values of the cells fabricated as mentioned in Chapter 3. The values so obtained are compared for different counter electrodes and the reasons for differences in their performance are also discussed here.

4.1 Cells fabricated without organic additives in TiO$_2$ paste

The figure 4.1 shows the absorption spectra of Eosin-Y solution in ethanol. The absorbance of the solution increases with an increase in concentration in accordance with Lambert-Beer's law.

$$A = \varepsilon\, l\, c$$

where, A is the absorbance, ε is the molar absorption co-efficient, l is the path length of light and c is the concentration of the solution.

4.1.1 Effect of electrolyte loss, film cracks and thickness on QE and I-V values

The figure 4.2 shows a plot of Absorbance versus Wavelength of Eosin-Y dyed TiO$_2$ film and QE versus Wavelength for the carbon soot based cell. Two distinct features can be observed here. The first one is that the absorbance is high in the dye characteristic region 450 – 600 nm, whereas QE in the same region is very low. The second feature is that QE values in measurement 2 are lower than in measurement 1. Measurement 2 is done 10 min after measurement 1.

There can be three reasons for the low value:

1. Low light harvesting efficiency, η_{lh} − This is due to the fact that in the UV-Vis spectra measurement setup, light is incident directly on the dye coated TiO_2, whereas in the QE measurement setup, the light is incident on the glass first and then penetrates through the film to reach the dye coated TiO_2 surface. There are reflection losses and transmission losses in the glass. The transmission spectrum of FTO glass is shown in figure 1.4. The average thickness of the edge of the TiO_2 film is $30 - 50$ μm as shown in figure 3.3(a)–(b); the light that travels through the thick TiO_2 can also undergo reflection. All these contribute to the low light harvesting efficiency in the dye characteristic region.

2. Low electron collection efficiency, η_{col} − The film has a large number of cracks, as observed in the optical profilometer. The electrolyte fills these cracks and I_3^- ions intercept the injected electrons reaching the FTO substrate. This recombination results in a low electron collection efficiency.

3. **Low electron injection efficiency, η_{inj}** − I^- ions in the electrolyte reduce the oxidized dye S^+ to S. When the amount of I^- ions is low, the electrons injected into the TiO_2 film recombine with the oxidized dye. This recombination leads to the low electron injection efficiency. The 2nd QE measurement is done 10 min after the 1st measurement and is lower than the first one. QE values decreasing with time suggest that the concentration of I^- ions also decreases with time. This decrease is due to the loss of electrolyte through the open ends in the cell.

Therefore, we can conclude that high thickness, cracks in the film and electrolyte loss contribute to low QE values.

4.1.2 Effect of carbon soot counter electrode vs Pt

The figures 4.3 through 4.5 show a comparison of the QE, I-V and IS values of a carbon soot counter electrode with those of a Pt counter electrode.

UV- Vis absorption spectrum of Eosin Y in ethanol at various concentrations
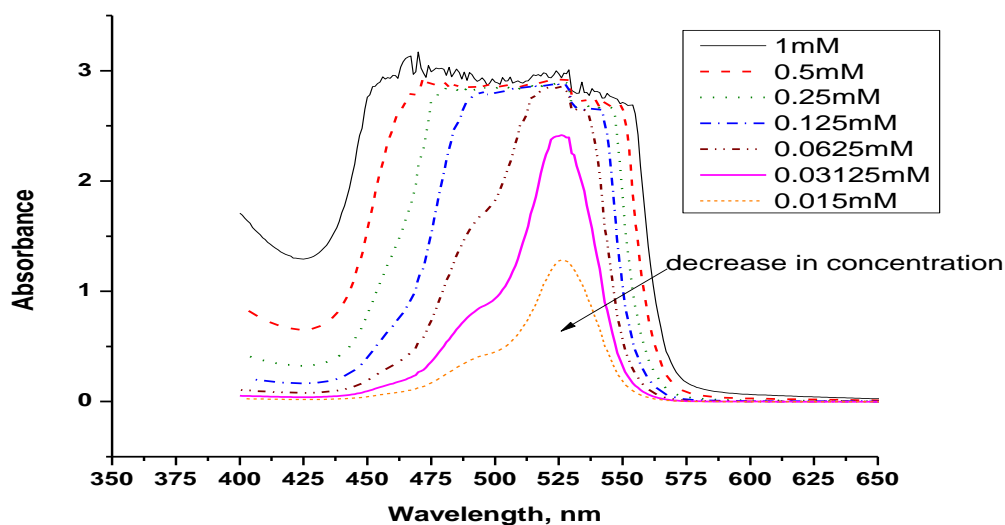
Figure 4.1 UV-Vis absorption spectrum of Eosin-Y in ethanol at various concentrations. The baseline correction was done using ethanol.
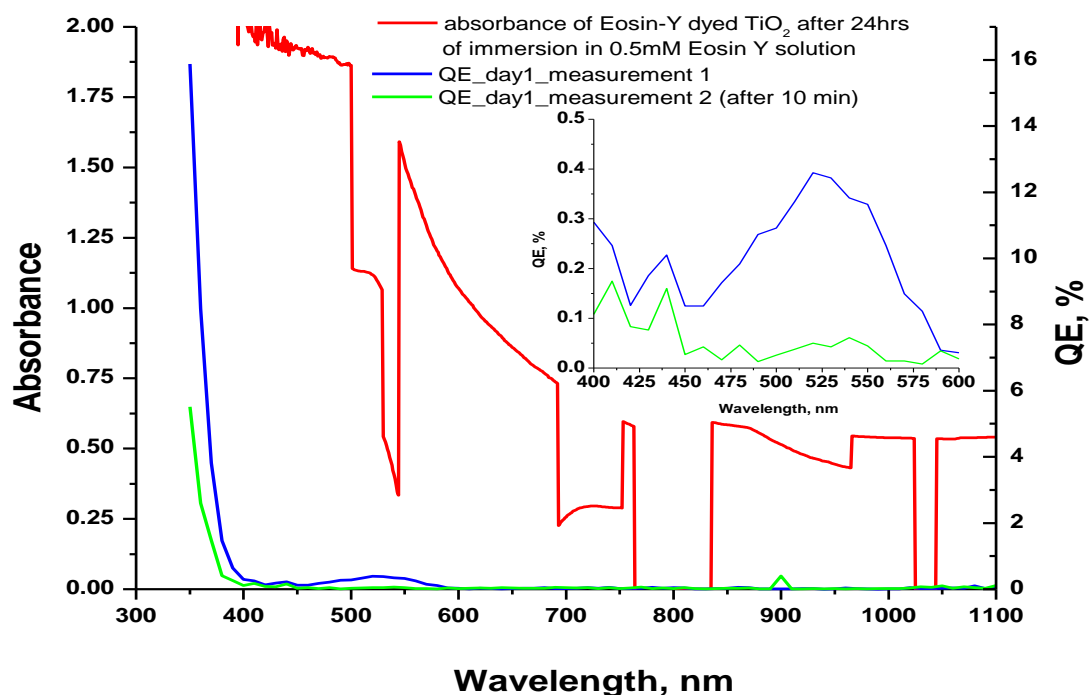
Figure 4.2 Graph – Left axis showing absorbance spectra of Eosin-Y TiO$_2$ film. The baseline correction was done using plain FTO glass. Right axis shows the QE measurements of Eosin-Y dyed cell with carbon soot counter electrode– Measurements 1 and 2 done at an interval of 10 min. Inset graph shows Eosin-Y characteristic. Absorbance shows high value in the dye characteristic region 450 – 600 nm whereas QE in the same region is very low.
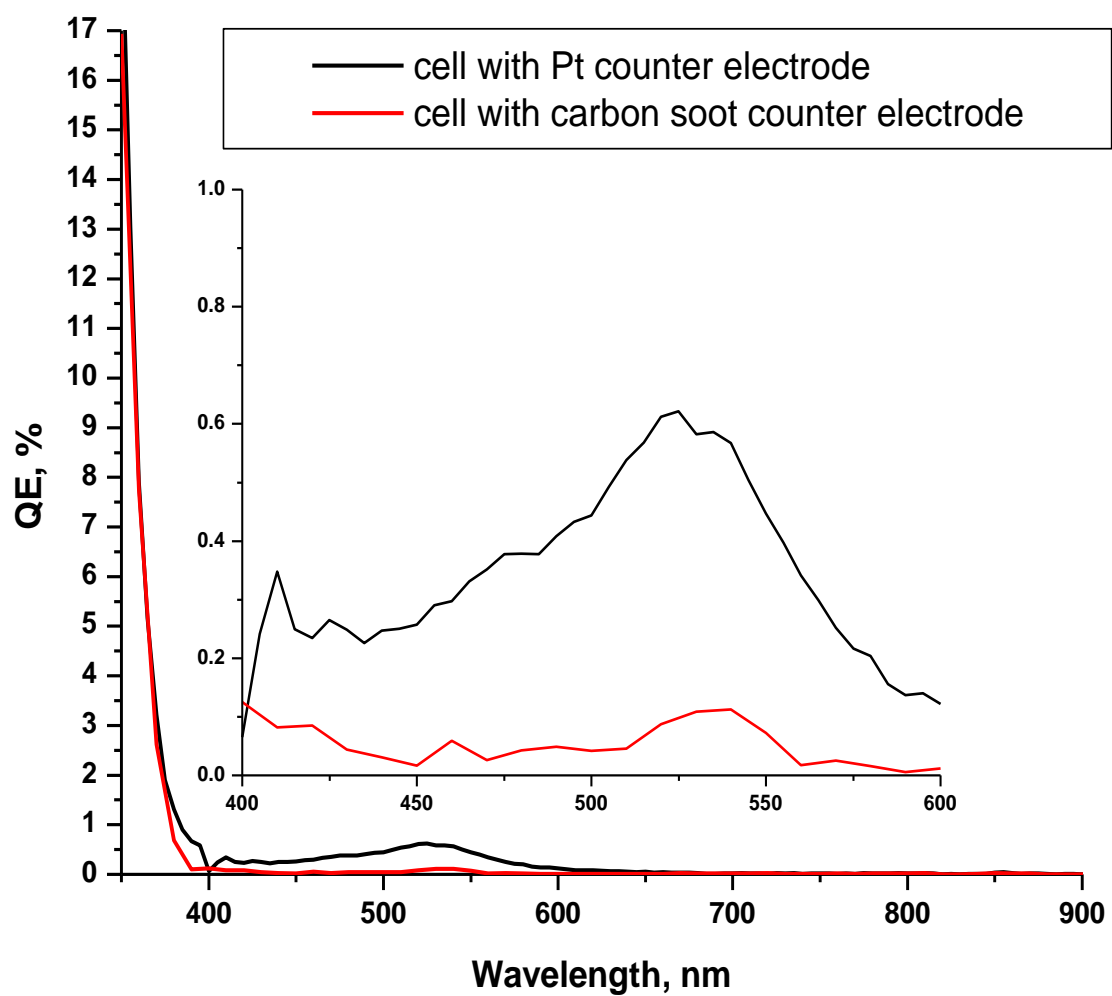
Figure 4.3 Graph comparing QE of carbon soot counter electrode with Pt counter electrode. The QE response in the region below 400 nm is that of TiO$_2$. The QE response in the region 400 – 600 nm is that of the dye. The cell with Pt counter electrode has a higher QE than its carbon counterpart.
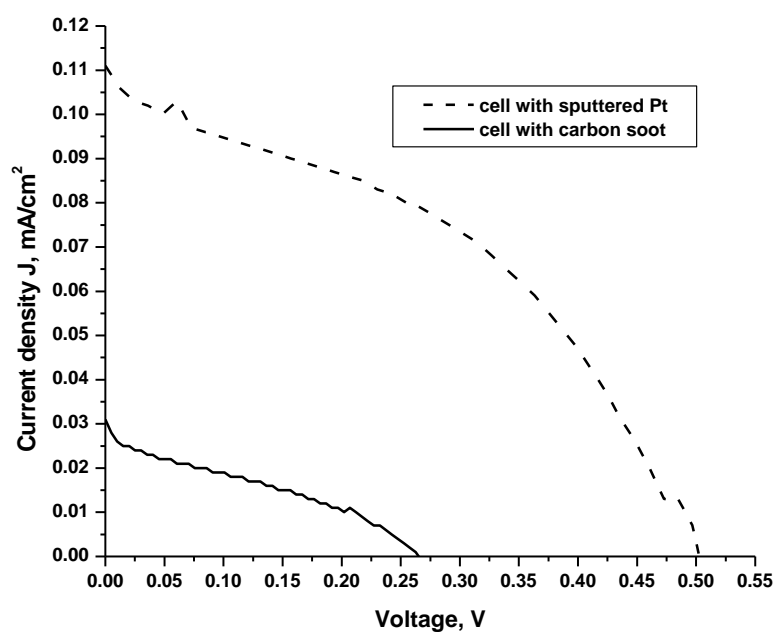
Figure 4.4 Graph comparing I-V of carbon soot counter electrode with Pt counter electrode. The cell with Pt counter electrode has higher J_{sc} of 0.11 mA/cm^2 and V_{oc} of 0.501 V than its carbon counterpart which has J_{sc} of 0.03 mA/cm^2 and V_{oc} of 0.264 V.

Table 4.1   Table comparing I-V characteristics of Eosin-Y carbon soot counter electrode with Pt counter electrode (referred from fig. 4.1)

Parameters	Pt counter electrode cell	Carbon soot counter electrode cell
V_{oc} (V)	0.501	0.264
J_{sc} (mA/cm^2)	0.11	0.03
J_{max} (mA/cm^2)	0.069	0.014
V_{max} (V)	0.323	0.165
P_{max} (mW/ cm^2)	0.022	0.002
Fill Factor (%)	40.47	30.59
Efficiency(%)	0.022	0.002
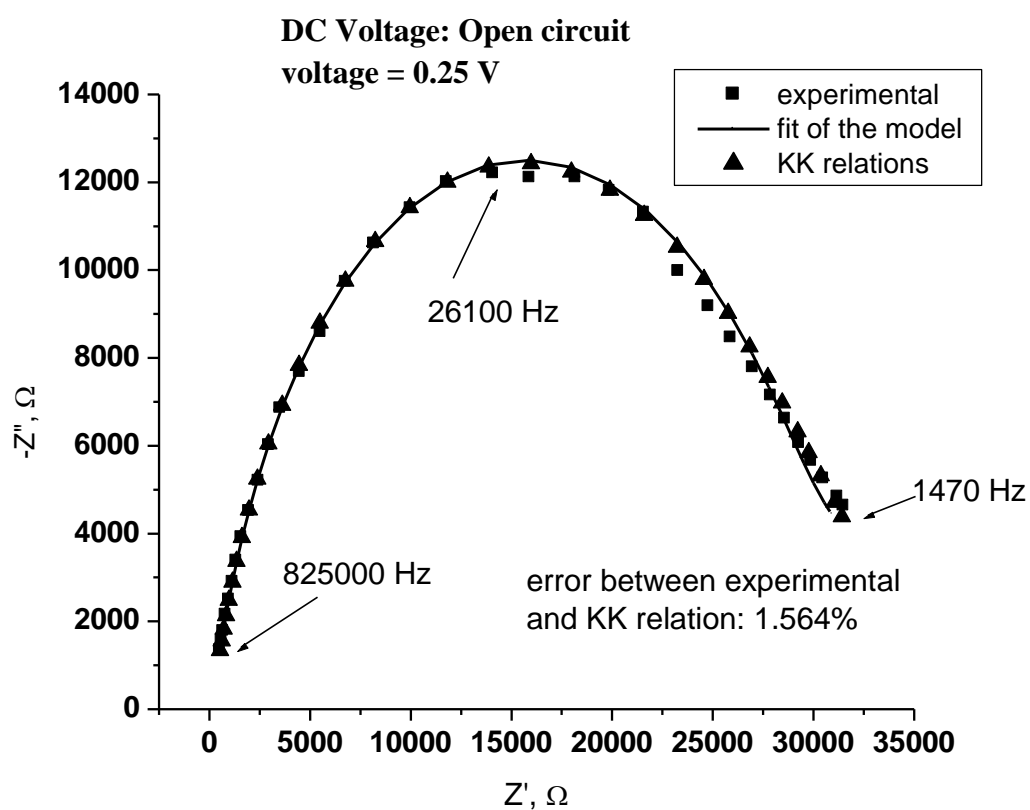
Figure 4.5(a) Cell with Eosin-Y as dye and carbon soot as counter electrode. Nyquist plot of experimental versus fit of the model and values calculated by KK relations.
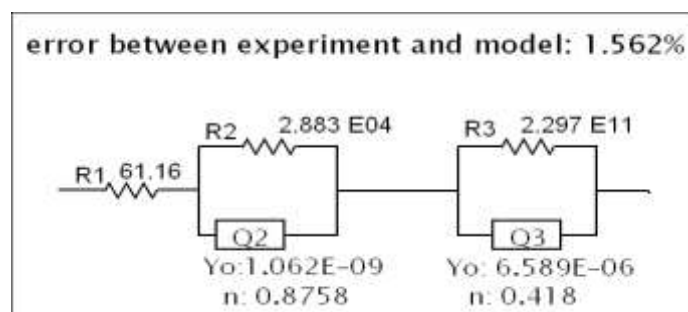
Figure 4.5 (b) Equivalent circuit of the experimental values in fig. 4.5(a)

DC Voltage: Open circuit
voltage = 0.501 V
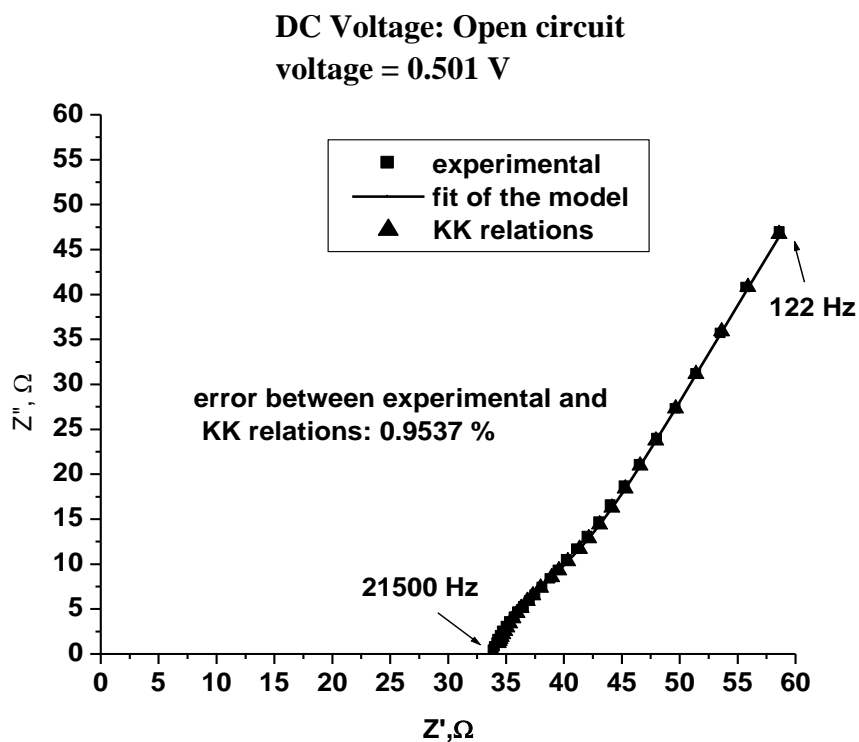
Figure 4.5(c) Cell with Eosin-Y as dye and Pt as counter electrode. Nyquist plot of experimental versus fit of the model and values calculated by KK relations.
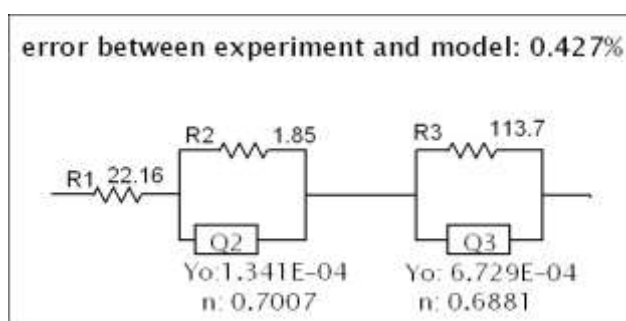
Figure 4.5(d) Equivalent circuit of the experimental values in fig 4.5(c)

Table 4.2 Comparison of parameters of equivalent circuit of Eosin-Y dyed cell with carbon soot and Pt counter electrodes (referred from fig. 4.5(a) — (d))

Parameter	Eosin-Y dyed cell with carbon soot as counter electrode	Eosin-Y dyed cell with Pt as counter electrode
Series resistance R1, Ω	61.16	22.16
Charge transfer resistance at counter electrode/ electrolyte interface R2, Ω	2.883×10^4	1.85
Charge transfer resistance at TiO$_2$ electrode/ electrolyte interface R3, Ω	2.297×10^{11}	113.7

The QE measurements in figure 4.3 show that the carbon soot based DSSC exhibits a very low peak value of QE, 0.1% in the dye characteristic region 450 – 600 nm; for the Pt-based cell it is 6 times higher, 0.6%. The I-V measurements (figure 4.4 and table 4.1) show that the cell containing Pt as the counter electrode exhibits a larger J_{sc} value of 0.11 mA/cm^2, a higher Voc of 0.501 V and a higher efficiency of 0.022% than the cell using carbon soot which has a J_{sc} of 0.03 mA/cm^2 and an efficiency of 0.002%. This can be attributed to the fact that sputtered Pt of thickness 100 nm covers the surface homogeneously, whereas carbon soot particles do not firmly adhere to the FTO surface and have a tendency to dislodge from the FTO surface, thereby leaving the electrolyte in contact with the FTO surface. FTO is a poor catalyst for reduction of I_3^- ions. In the IS measurements shown in figures 4.5(a) – (d), the impedance data satisfy the KK relations. For the Pt-based cell, the charge transfer resistance at the Pt electrode is 1.85 Ω; for the carbon cell it is 4 orders of magnitude higher, $\sim$ 29000 Ω. The low value of charge transfer resistance implies a lesser resistance to the reduction of I_3^- ions, and so the Pt cell has a much higher efficiency than the carbon soot cell.

4.2 Cells fabricated with organic additives in TiO$_2$ paste

The figure 4.6 shows the absorbance of N719 dye solution in ethanol and the absorbance of N719 dyed TiO$_2$ film as a function of the soaking time in 0.5 mM N719 dye solution in ethanol. Absorbance of N719 dyed TiO$_2$ film saturates after 15 hrs.

Absorbance of N719 dyed TiO$_2$ film as a function of time of immersion in dye

— TiO$_2$ film immersed in N719 dye for 1hr
— TiO$_2$ film immersed in N719 dye for 2hr
— TiO$_2$ film immersed in N719 dye for 3hr
— TiO$_2$ film immersed in N719 dye for 15hrs
— 0.5mM N719 dye in ethanol
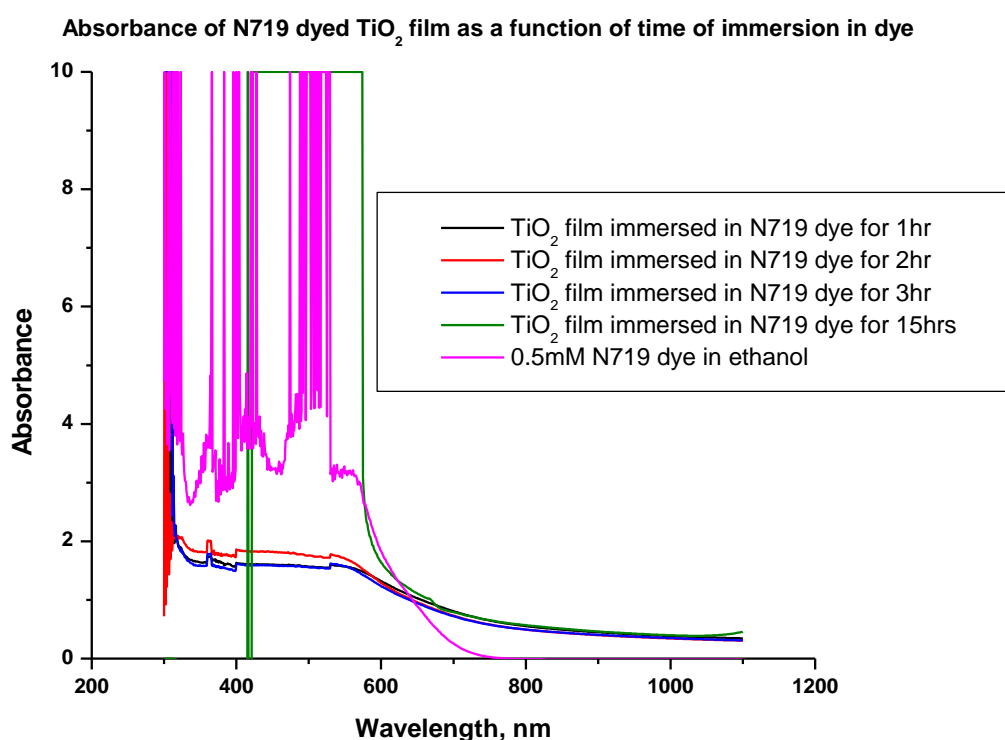
Figure 4.6 Graph showing absorbance of N719 dyed TiO$_2$ film as a function of time of soaking in dye; the base line correction was done using plain FTO glass. Absorbance increases with time.

4.2.1 Effect of Pt obtained by thermal decomposition of Platisol vs sputtered Pt

The QE, I-V and IS values of thermally deposited Pt and sputtered Pt are compared in the graphs presented in figures 4.7 through 4.9.
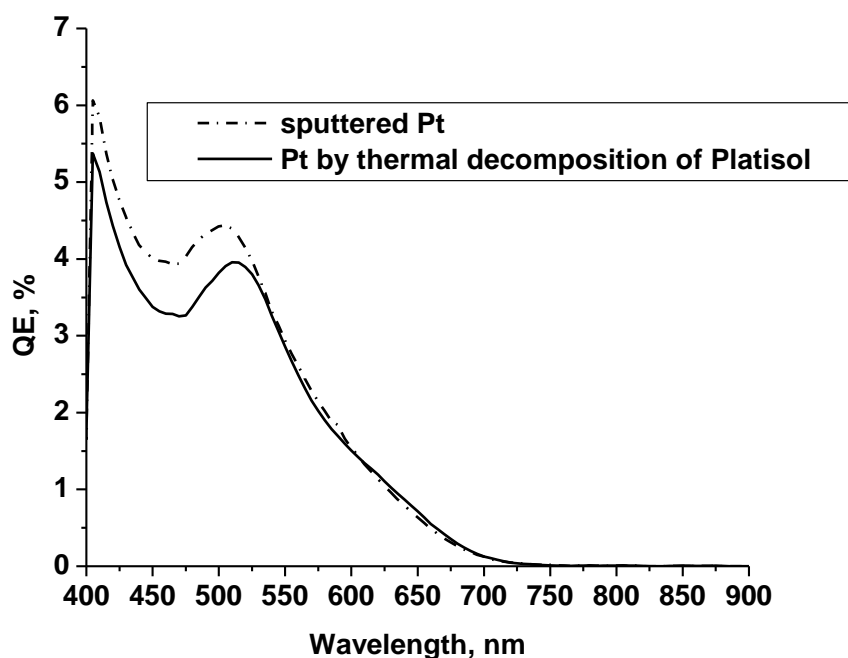
Figure 4.7 Graph comparing QE values of Pt deposited by thermal decomposition of Platisol and sputtered Pt cells. In the dye characteristic region of 400 – 700 nm, QE of sputtered Pt is only marginally higher than that obtained by thermal decomposition of Platisol.
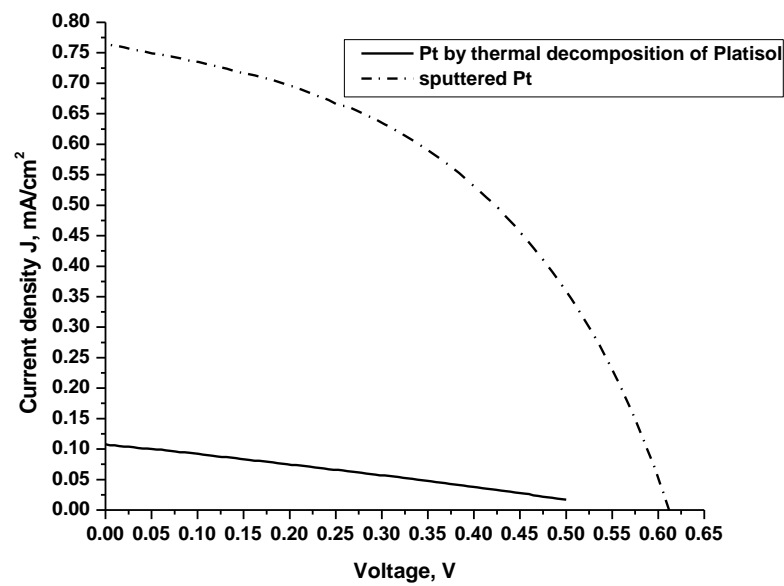
Figure 4.8   I-V curve comparing Pt deposited by thermal decomposition of Platisol and sputtered Pt cells . J_{sc} of sputtered Pt cell is 7 times greater than Jsc of Platisol Pt cell

Table 4.3   Table comparing I-V curve parameters of N719 dyed cell with Pt deposited by thermal decomposition of Platisol and sputtered Pt film (referred from fig. 4.8)

	N719-dyed cell with thermally deposited Pt	N719-dyed cell with sputtered Pt film
V_{oc} (V)	0.585	0.61
J_{sc} (mA/cm^2)	0.108	0.764
J_{max} (mA/cm^2)	0.303	0.526
V_{max} (V)	0.057	0.404
P_{max} (mW/cm^2)	0.017	0.213
Fill Factor (%)	30.6	45.7
Efficiency(%)	0.017	0.213
Sheet resistance, $\Omega/\square$	12.49	1.2
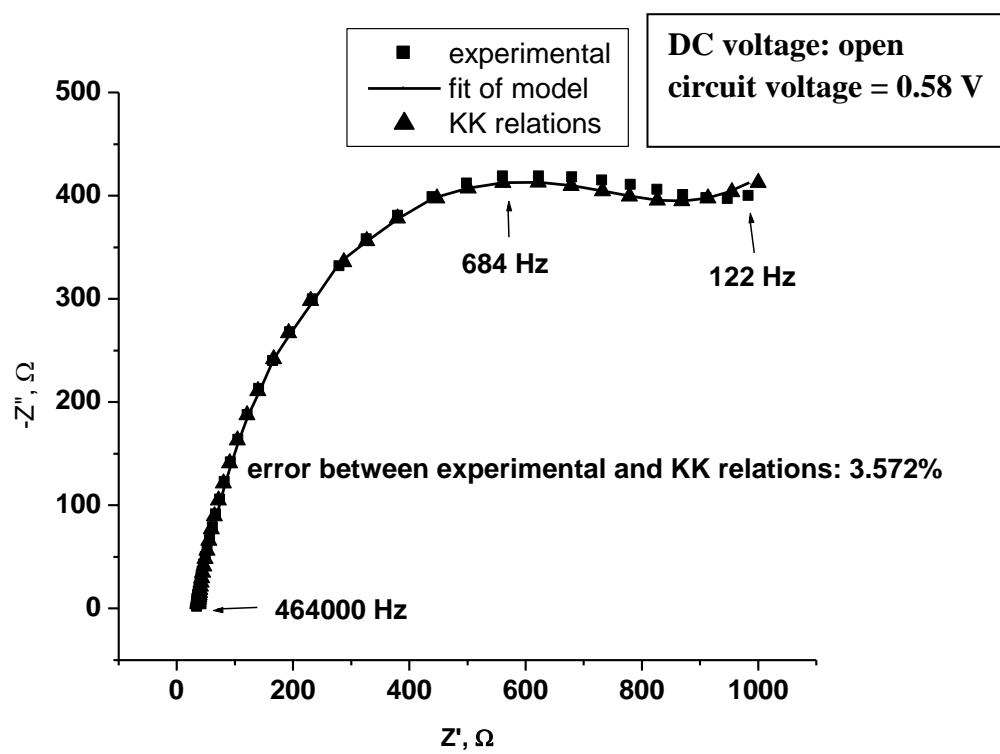
Figure 4.9(a) Cell with Pt deposited by thermal decomposition of Platisol as counter electrode. Nyquist plot of experimental versus fit of the model and values calculated by KK relations.
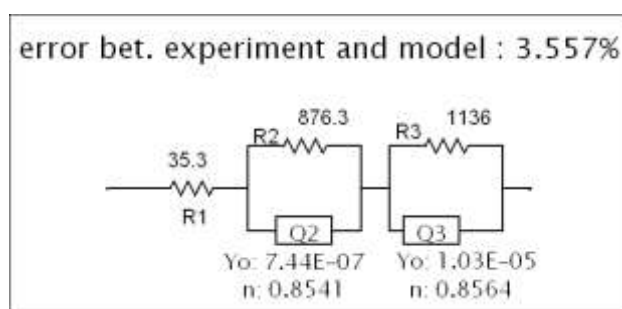
Figure 4.9(b) Equivalent circuit for the experimental values in fig 4.9(a)
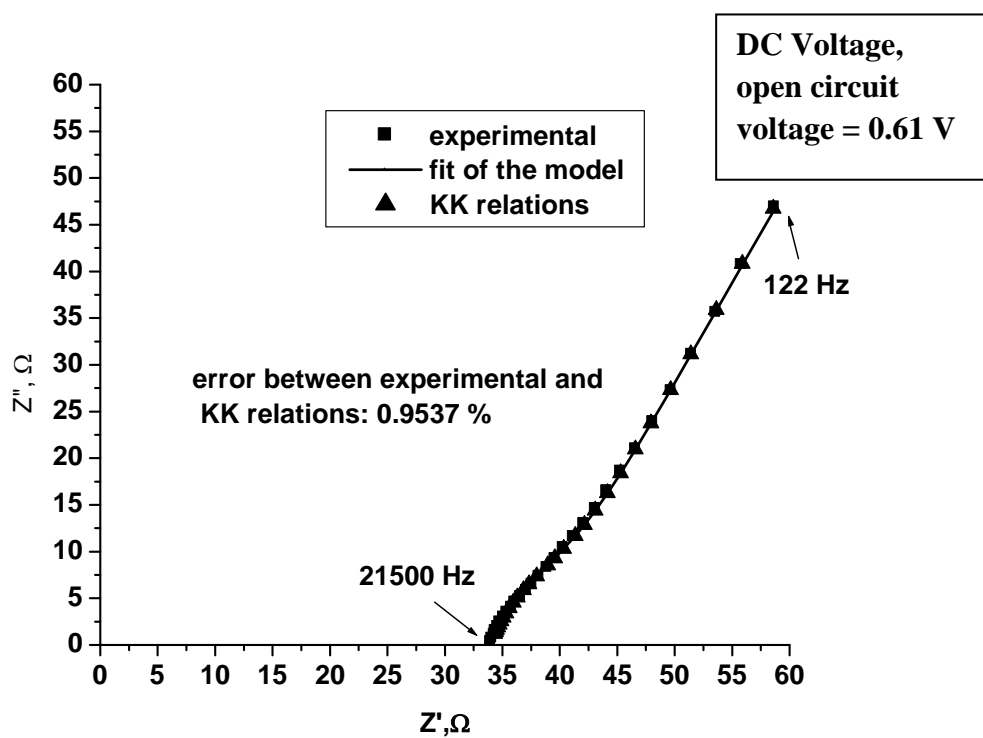
Figure 4.9(c) Nyquist plot of cell with sputtered Pt as counter electrode. Experimental versus fit of the model and values calculated by KK relations.
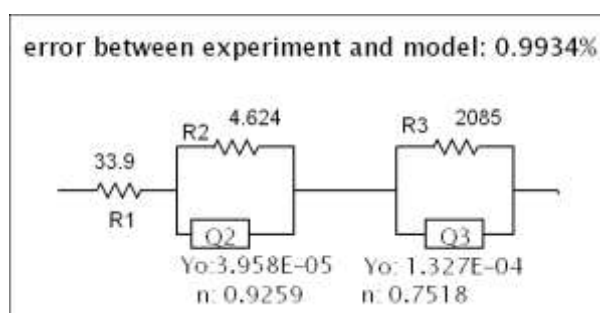
Figure 4.9(d) Equivalent circuit for the experimental values in fig 4.9(c)

Table 4.4   Comparison of parameters of equivalent circuit of N 719 dyed cell with sputtered Pt film and Pt obtained by thermal decomposition Platisol (referred from fig. 4.9 (a) — (d))

Parameter	N719 dyed cell with Pt obtained by thermal decomposition of Platisol as counter electrode	N719 dyed cell with sputtered Pt as counter electrode
Series resistance R1, Ω	35.3	33.4
Charge transfer resistance at counter electrode/ electrolyte interface R2, Ω	876.3	4.624
Charge transfer resistance at TiO$_2$ electrode/ electrolyte interface R3, Ω	1136	2085

In the QE graph shown in figure 4.7, the peak value of QE in the dye characteristic region is 4.5% for sputtered Pt based DSSC; this is only marginally higher than the QE value of Pt obtained by thermal decomposition of Platisol for which QE is 4%. The I-V and impedance spectrum graphs, however show significantly different values for sputtered Pt and Platisol Pt cells. In the I-V curve, shown in figure 4.8, sputtered Pt yields a higher J_{sc}, 0.764 mA/cm^2 and V_{oc}, 0.61V and consequently a higher efficiency, η 0.21%, than thermally deposited Pt, with J_{sc} 0.107 mA/cm^2, V_{oc} 0.585V, η 0.017%. Correlating with the sheet resistance values in the table 4.3, a 10 time decrease in sheet resistance from 12.49 Ω/□ for Platisol Pt to 1.2 Ω/□ for sputtered Pt increases the efficiency by a factor of 10. The difference in sheet resistance values has significant consequences on the parameters obtained in impedance measurements,

shown in figures 4.9(a)–(d) and table 4.4. A high sheet resistance of 12.49 $\Omega/\square$ for Pt deposited by thermal decomposition of Platisol gives rise to a high resistance, R2, 876 Ω, for the reduction of I_3^- ions at the counter electrode of the cell. A lower sheet resistance value for sputtered Pt leads to a lower resistance, R2, 4.624 Ω for the reduction of I_3^- ions at the Pt electrode. The charge transfer resistance at TiO_2/electrolyte interface, R3, for the two cells, shows opposite behaviour to that at the Pt electrodes. For the Platisol Pt cell, R3 is 1136 Ω which is lesser than R3 for sputtered Pt cell, 2085 Ω. This is also a consequence of charge transfer at the Pt electrode/electrolyte interface. When the I_3^- ions encounter a high resistance for reduction at the counter electrode, there is a larger tendency for I_3^- ions to recombine with the photo-injected electrons in TiO_2; so the resistance associated with recombination is lesser. Therefore, R2 in Platisol Pt cell is lesser than R2 in sputtered Pt cell. The impedance data of both the types of cells satisfy KK relations which means they are stable to the applied AC perturbation.

4.2.2 Performance of sputtered Pt based DSSC

The time related performance of two cells based on sputtered Pt counter electrode is discussed here. The graphs of cell 1 are presented in figures 4.10 through 4.12. The graphs of cell 2 are presented in figures 4.13 through 4.15.
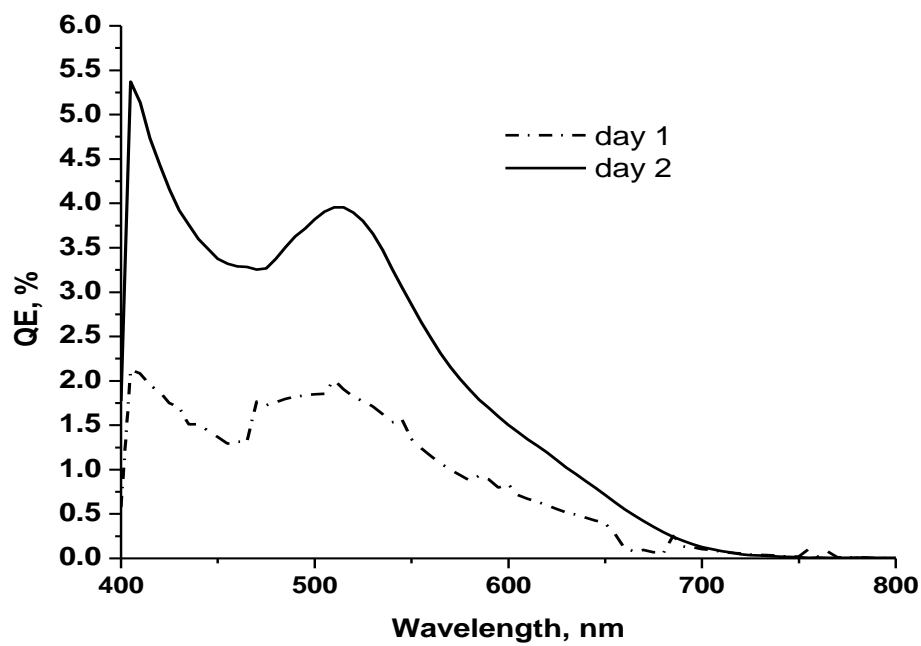
Figure 4.10 QE values of cell 1 on day 1 and day 2. On day 2, the values are 50% lower than values on day 1.
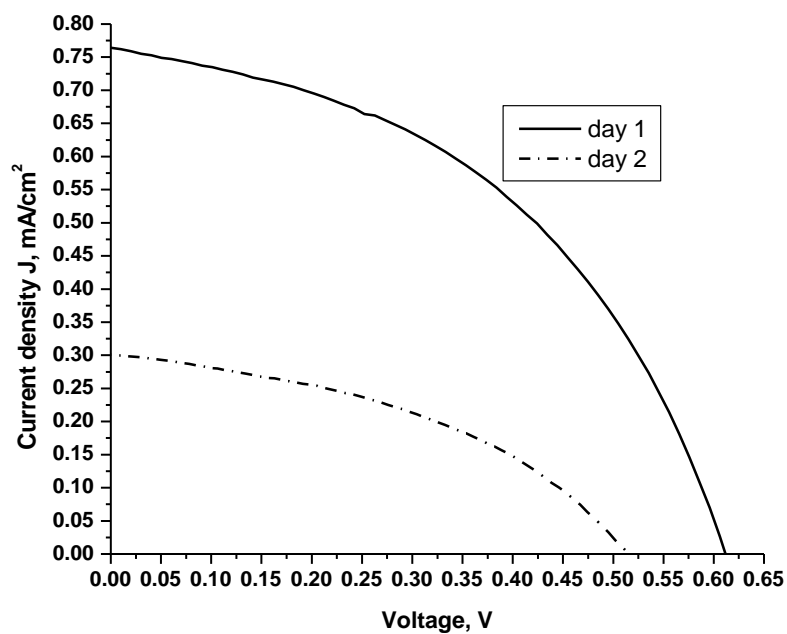
Figure 4.11 Cell 1 I-V curve comparing the values obtained on day 1 and day 2. On day 2, Jsc has reduced by over 50% of Jsc on day 1.

Table 4.5   Table showing the I-V curve values of Cell 1 on day 1 and day 2
(referred from fig. 4.11)

	Day 1	Day 2
V_{oc} (V)	0.61	0.514
J_{sc} (mA/cm^2)	0.765	0.301
J_{max} (mA/cm^2)	0.53	0.198
V_{max} (V)	0.4	0.33
P_{max} (mW/cm^2)	0.213	0.065
Fill Factor (%)	45.6	41.87
Efficiency(%)	0.213	0.065

DC Voltage: Open circuit
voltage = 0.62 V
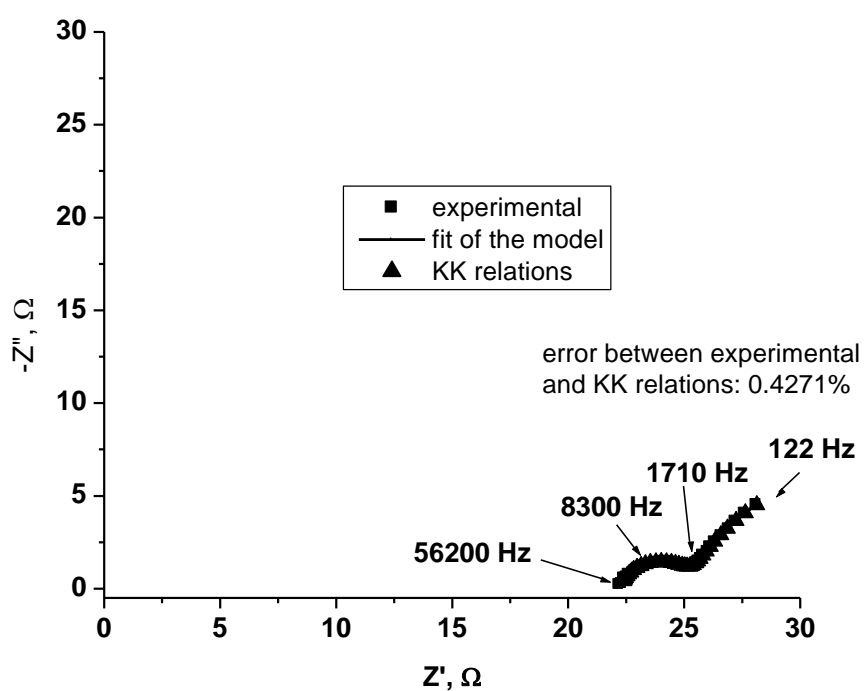
Figure 4.12(a) Cell 1 with sputtered Pt as counter electrode. Values on day 1. Nyquist plot of
experimental versus fit of the model and values calculated by KK relations.

68

Figure 4.12(b) Equivalent circuit of experimental values in fig 4.12(a)

DC Voltage: Open circuit voltage = 0.51 V

Figure 4.12(c) Cell 1 with sputtered Pt as counter electrode. Values on day 2. Nyquist plot of experimental versus fit of the model and values calculated by KK relations

Figure 4.12(d) Equivalent circuit of experimental values in fig 4.12(c)

Table 4.6   Cell 1 N719 dyed cell with sputtered Pt electrode. Comparison of parameters of equivalent circuit on day 1 and day 2 (referred from fig 4.12(a)—(d))

Parameter	Day 1	Day 2
Series resistance R1, Ω	22.3	23.1
Charge transfer resistance at counter electrode/ electrolyte interface R2, Ω	2.81	1.3
Charge transfer resistance at TiO$_2$ electrode/ electrolyte interface R3, Ω	21.85	118.1
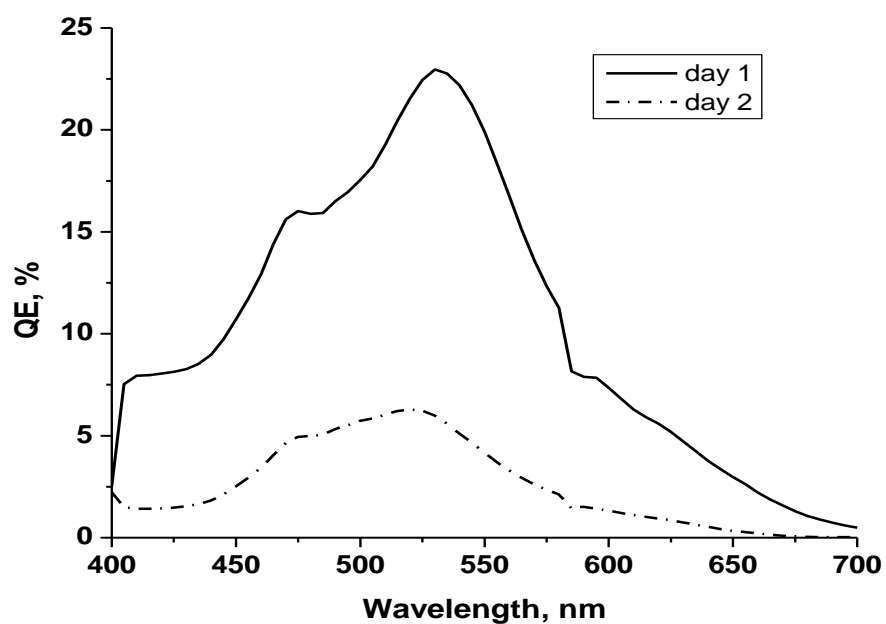
Figure 4.13 Cell 2 Graph comparing QE values on day 1 and day 2. On day 2, in the dye characteristic region of 400 – 600nm, the peak has reduced to 20% of the peak value on day 1.
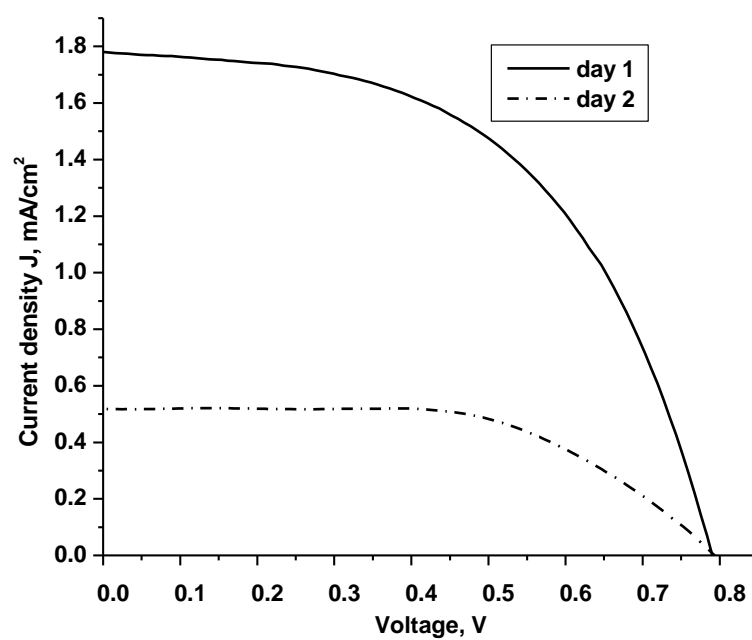
Figure 4.14 Cell 2 I-V curve on day 1 and day 2. V_{oc} is the same 0.8V on both the days. However, on day 2, J_{sc} has reduced to 30% of the value measured on day 1.

**Table 4.7 Table showing the I-V curve values of Cell 2 on day 1 and day 2
(referred from fig. 4.14)**

	Day 1	Day 2
V_{oc} (V)	0.79	0.793
J_{sc} (mA/cm^2)	1.78	0.518
J_{max} (mA/cm^2)	1.38	0.466
V_{max} (V)	0.542	0.521
P_{max} (mW/cm^2)	0.748	0.242
Fill Factor (%)	53.19	59.06
Efficiency(%)	0.748	0.242
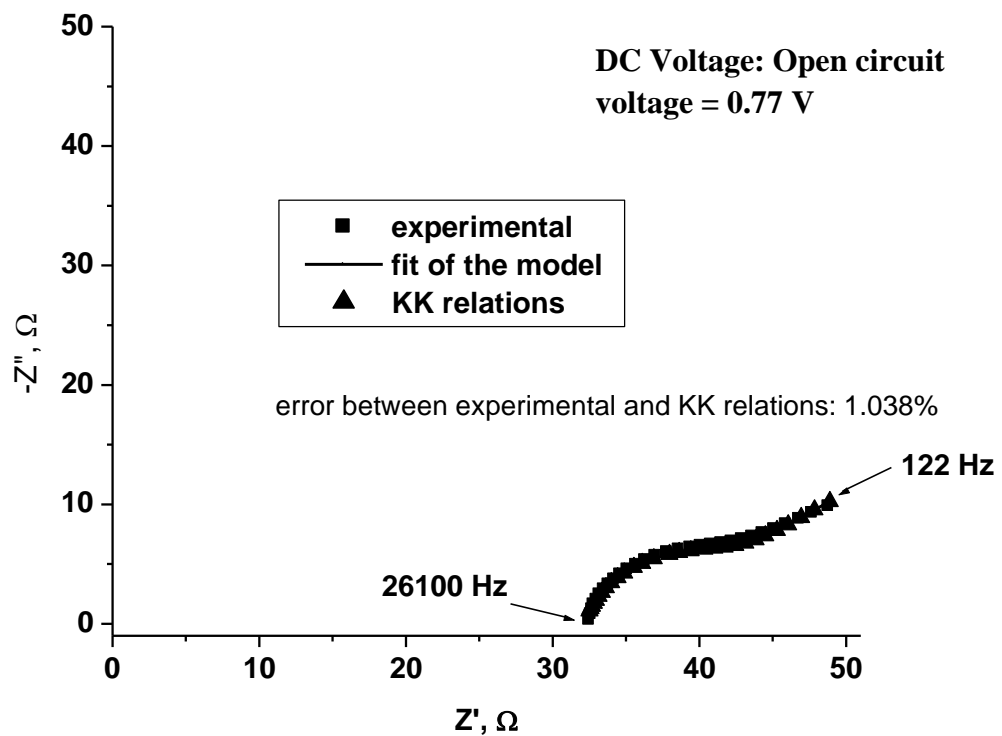
Figure 4.15(a) Cell 2 with sputtered Pt as counter electrode. Values on day 1. Nyquist plot of experimental versus fit of the model and values calculated by KK relations
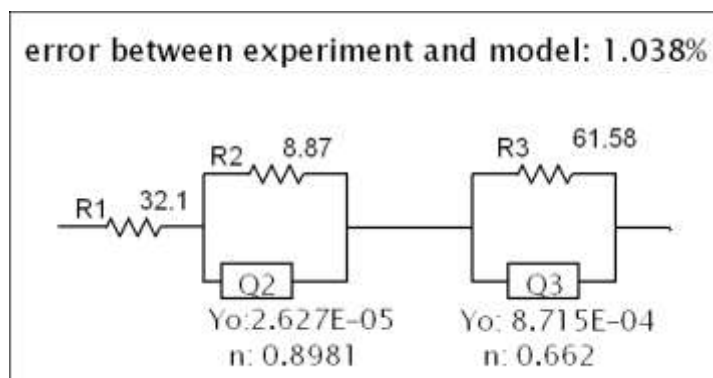
Figure 4.15(b) Equivalent circuit of the experimental values in fig 4.15(a)

DC Voltage: Open circuit voltage = 0.79 V
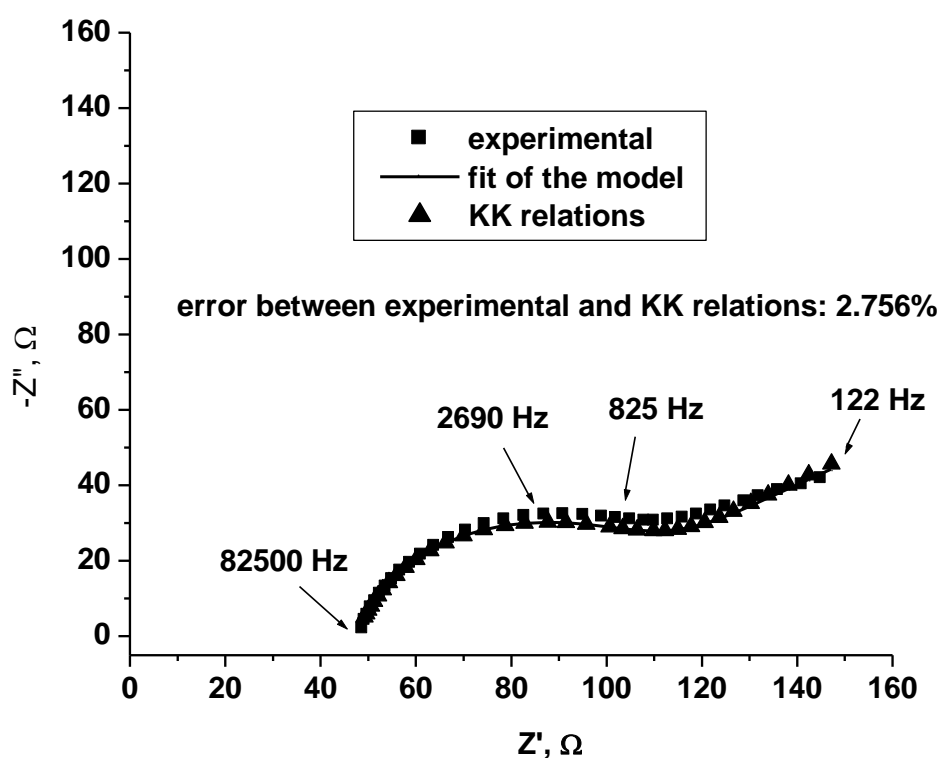
Figure 4.15(c) Cell 2 with sputtered Pt as counter electrode. Values on day 2. Nyquist plot of experimental versus fit of the model and values calculated by KK relations.
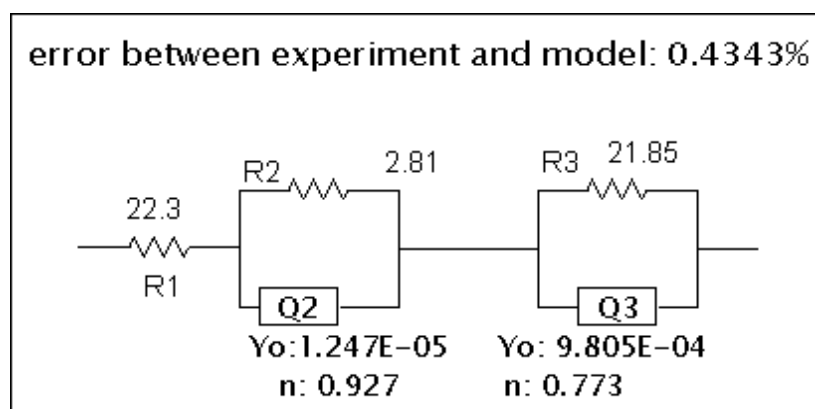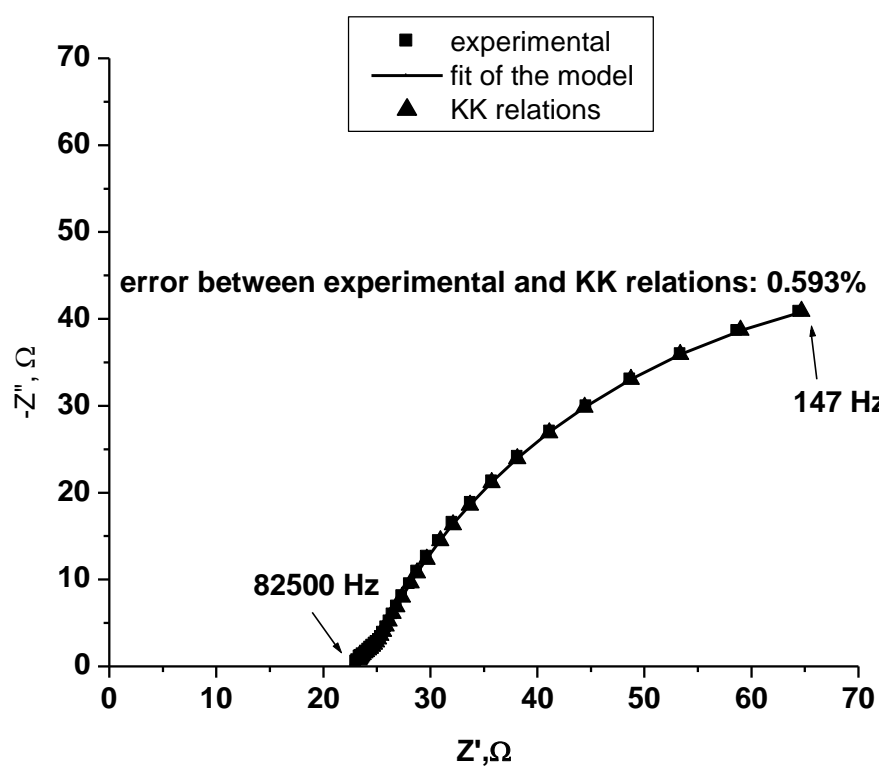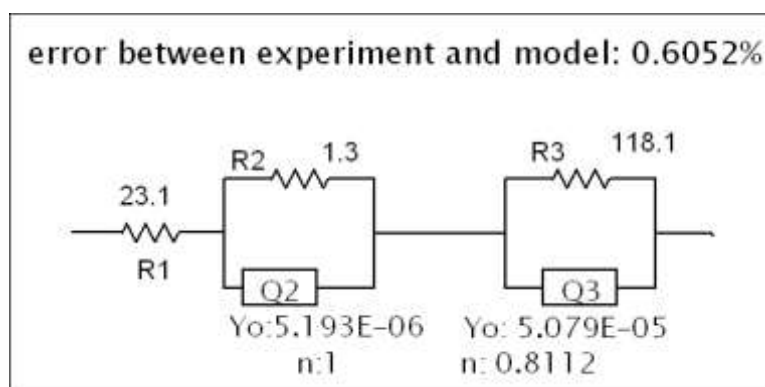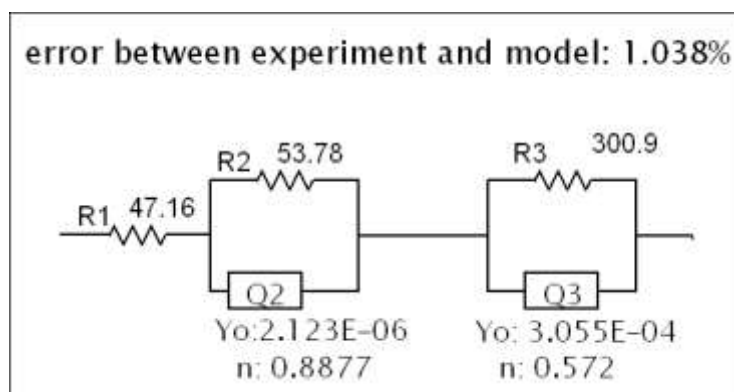
Figure 4.15(d) Equivalent circuit of the experimental values in fig 4.15(c)

Table 4.8   Cell 2 N719 dyed cell with sputtered Pt electrode. Comparison of parameters of equivalent circuit on day 1 and day 2 (referred from fig 4.15(a) — (d))

| Parameter	Day 1	Day 2
Series resistance R1, Ω	32.1	43.16
Charge transfer resistance at Pt electrode/ electrolyte interface R2, Ω	8.87	53.78
Charge transfer resistance at TiO_2 electrode/ electrolyte interface R3, Ω	61.58	300.9

Studying the performance of the two cells, it is found that the cells display different maxima for each of the parameter measured. The time related behaviour is also different. For cell 1, from figure 4.10, the maximum QE value on day 1 is in the range 4–5.5%, while on day 2, it has dropped to 2%, a 50% reduction from the initial value. For cell 2, referring to figure 4.13, the QE value is 25% on day 1, 5 times higher than that for cell 1; on day 2, the QE values have reduced to 1/4th the initial value, to 5%.

For cell 1, the reduction in QE is only one-half the initial value. The QE value of the liquid electrolyte cells reported in literature is greater than 60% [55] for which the cell thickness is 12 – 15 μm. In the current study, the thickness of the cells is over 20 μm. Higher thickness of TiO$_2$ films implies a longer travel route for the photo-injected electrons, greater than the path length of electrons. The **path length** is the distance travelled by electrons before their recombination with the oxidized dye or I$_3^-$ ions. This leads to a higher recombination of electrons before reaching the FTO substrate and hence a lower quantum efficiency.

In case of the IV curves, for cell 1, the change in V$_{oc}$ with time is significant, as seen in figure 4.11 and table 4.5. V$_{oc}$ is 0.61 V on day 1; on day 2 it has reduced by 16% to 0.514 V. J$_{sc}$ has reduced by more than 50% from 0.765 mA/cm^2 on day 1 to 0.301 mA/cm^2 on day 2. Efficiency, η, has reduced to 1/3rd its initial value, from 0.213% to 0.065%. For cell 2, referring to figure 4.13 and table 4.7, V$_{oc}$ has remained the same for 2 days, at 0.79 V, but J$_{sc}$ has reduced from 1.8 mA/cm^2 to 0.518 mA/cm^2, which is just 30% of the initial value. Efficiency follows a similar trend; it has decreased from 0.748% to 0.242%. Typical values of η reported in literature are 9.2 – 10% [64],[55] for cells with a thickness of 12–14 μm and an active area of 0.25 cm^2. In the current study, the active area of the cells is 1 cm^2. A higher active cell area increases the sheet resistance, so the efficiency scales down accordingly. In the current study, a higher active cell area coupled with a higher thickness of 20–22 μm for TiO$_2$ films leads to low efficiencies. The decrease in efficiency with time is due to the loss of the electrolyte, because the electrolyte is the only fluid and volatile component in the cell, capable of leaking out. This is also confirmed by the impedance data.

The impedance data of both the cells satisfy KK relations, as seen in figures 4.12(a),(c) and figures 4.15(a),(c). In both the cells, the charge transfer resistance at each of the electrodes increases with time, as shown in tables 4.6 and 4.8. For cell 1, on day 1, R2 at the Pt electrode is 2.81 Ω; R3 at TiO$_2$ electrode is 21.85 Ω. On day 2, R2 is 1.81 Ω; R3 is 118 Ω. For cell 2, on day 1, R2 at the Pt electrode is 8.87 Ω; R3 at the TiO$_2$ electrode is 61.58 Ω. On day 2, the R2 and R3 values have increased nearly 6 times to 53.78 Ω and 300.9 Ω, respectively. This increase can be attributed to the loss of the electrolyte. When the amount of the redox electrolyte is high, there are a lot of

I_3^- ions to intercept the photo-injected electrons. So, the resistance to charge transfer at the TiO_2 / electrolyte interface is low. Similarly, at the Pt electrode, there are a large number of I_3^- ions that accept the electrons reaching the electrode. So the resistance to charge transfer at the Pt electrode/electrolyte interface is low. Therefore, on day 1, the resistance to charge transfer is lesser. When the amount of electrolyte is low, there are fewer I_3^- ions. So, the resistance to charge transfer at the respective electrodes is high. Hence, on day 2, the resistance to charge transfer is higher. In literature, the values reported for the specific charge transfer resistance at the Pt/electrolyte interface is $2.1\Omega cm^2$ [66] for sputtered Pt thickness of $2-3$ nm, and a charge transfer resistance of $20-150$ Ω [67] at the TiO_2/electrolyte interface.

4.3 Conclusion

DSSCs with TiO_2 films prepared without organic additives and sintered at low temperatures yield low efficiencies due to the presence of a large number of cracks in the films. Spreading of TiO_2 paste in a single coat with a glass rod and having 50 μm thick cellotape as the reference for thickness yields films with high thickness and uneven surface. Multiple spin coating of TiO_2 paste without any reference for thickness yields films with thickness in $20-22$ μm range. Platinum based DSSC yields a higher efficiency than a carbon soot based DSSC as Pt offers less resistance to reduce I_3^- ions, as shown by IS measurements. Among the two methods used for depositing Pt, sputtered Pt film DSSC exhibits a higher efficiency than thermally deposited Pt owing to its lower sheet resistance. This is also confirmed by IS measurements which show that sputtered Pt film offers less resistance to the reduction of I_3^- ions. DSSCs suffer from the problem of instability. Electrolyte loss has been found to be the reason for instability. Therefore, sealing of DSSCs should be improved to prevent the loss of the electrolyte.

Chapter 5

Summary and future work

The dye-sensitised solar cells prepared using organic additives for TiO_2 films have fewer cracks than the cells prepared without using organic additives for TiO_2 films. The counter electrode with sputtered Pt of 100 nm exhibits higher efficiencies compared to Pt deposited by thermal decomposition of Platisol and carbon soot. Therefore in the future, the performance of solar cells should be investigated with sputtered Pt of thickness less than 100 nm and the optimum thickness should be found out. Sealing should be improved by following better surface treatment techniques for FTO glass so that the sealant can adhere properly to the FTO glass.

Appendix A

I. Procedure for EIS measurement using CHI 608D workstation

Step 1: Place the solar cell with the dyed TiO_2 face up on the solar simulator cell stage.

Step 2: Connect the working electrode, WE, – green – to the dyed-TiO_2 substrate. Connect the counter and reference electrodes, CE and RE respectively, to the Pt counter electrode of the cell. The electrodes of the instrument should never touch the metallic cell stage. Otherwise it can cause a short circuit.

Step 3: Connect the workstation to a computer.

Step 4: Connect the workstation to a UPS. Turn on the main power supply first. Then turn on the power button in the instrument. Open the CHI 608D software installed in the computer.

Step 5: Turn on the solar simulator. (Solar simulator operation should be learnt from a different operator)

Step 6: Go to **"Control→ open-circuit potential".** Record the open circuit potential. Click OK.
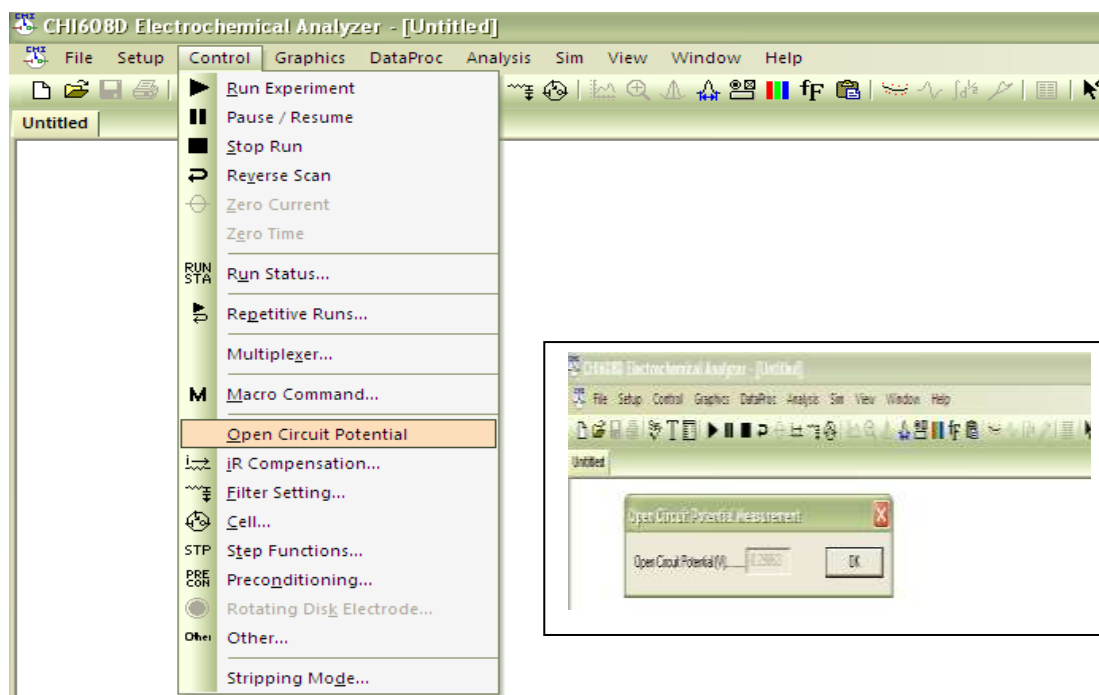
Step 7: Go to "**Setup→ Technique**".
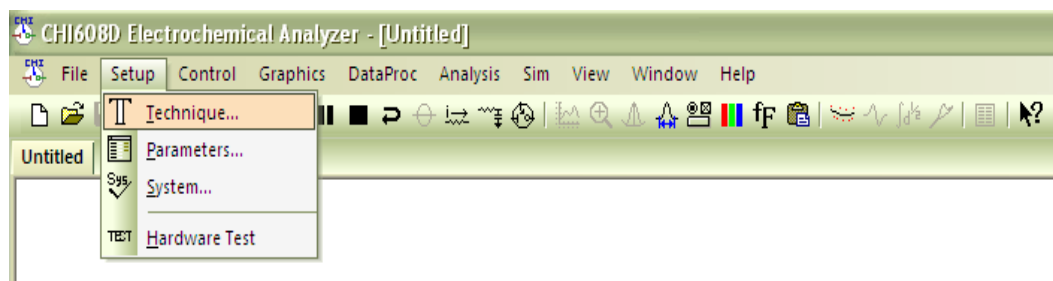
Step 8: Select **A.C Impedance**. Click **OK.** Enter the parameters. Init E = open circuit potential. High Freq = 1000000. Low Freq = 0.01. Amplitude should be between 0.005 and 0.01 V. After entering all the parameters click OK.
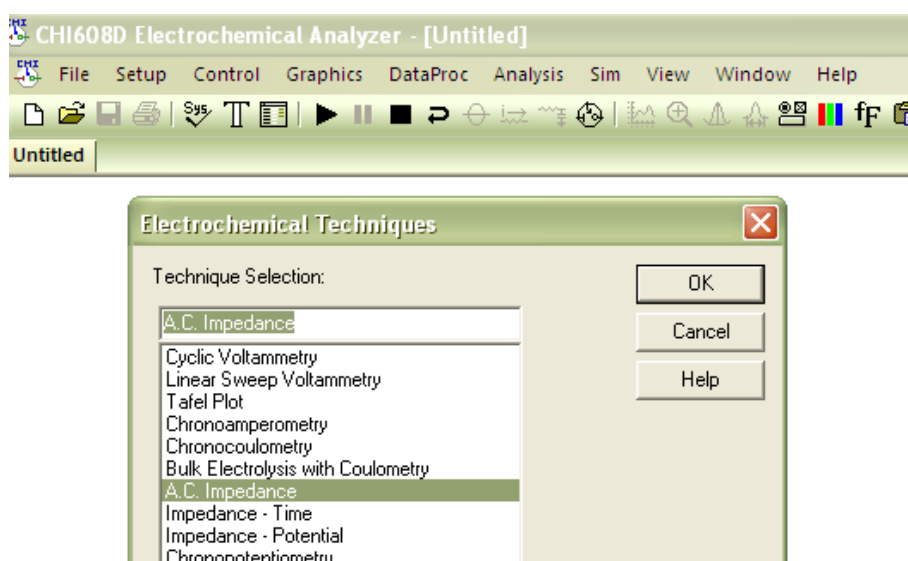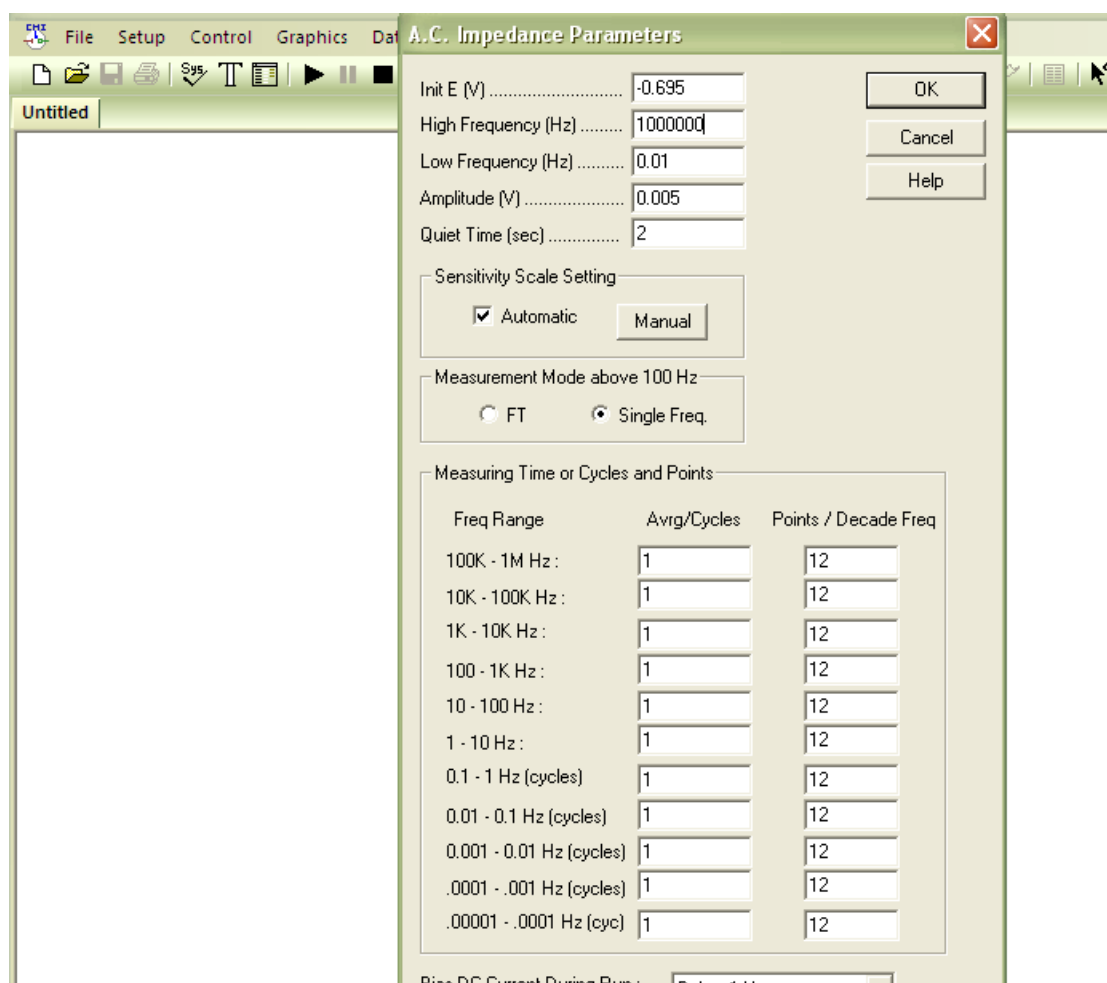
Step 9: Click " Run icon" The scan starts. The progress of the scan being indicated by the timer is shown below.

Freq=1.00Hz Z=1.152e+005 Phase=20.6 AutoSens=1e-007
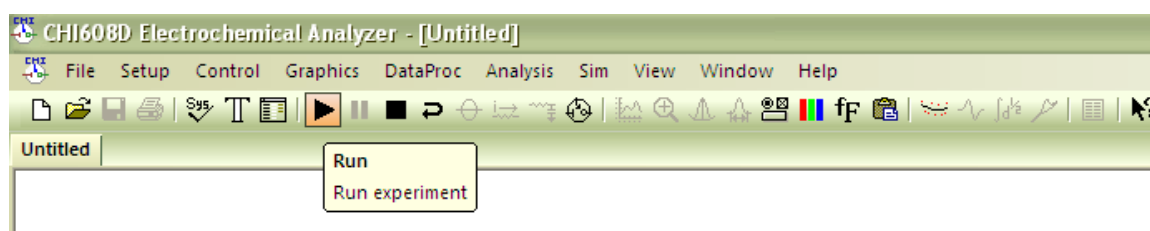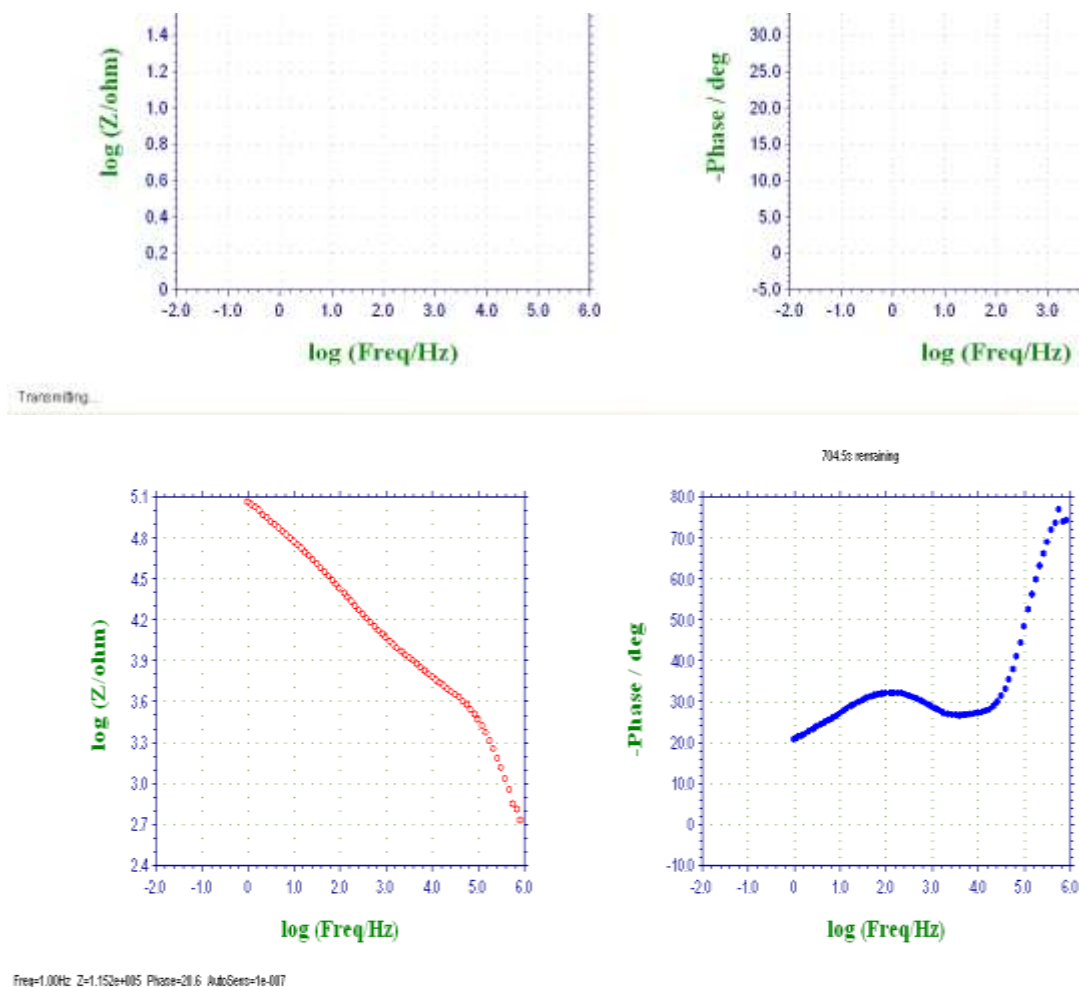
Step 10: When the timer stops, it indicates the end of the scan. Turn off the solar simulator. Go to **"File→ Save as"** and save as both "XYZ.bin" and "XYZ.text" files.
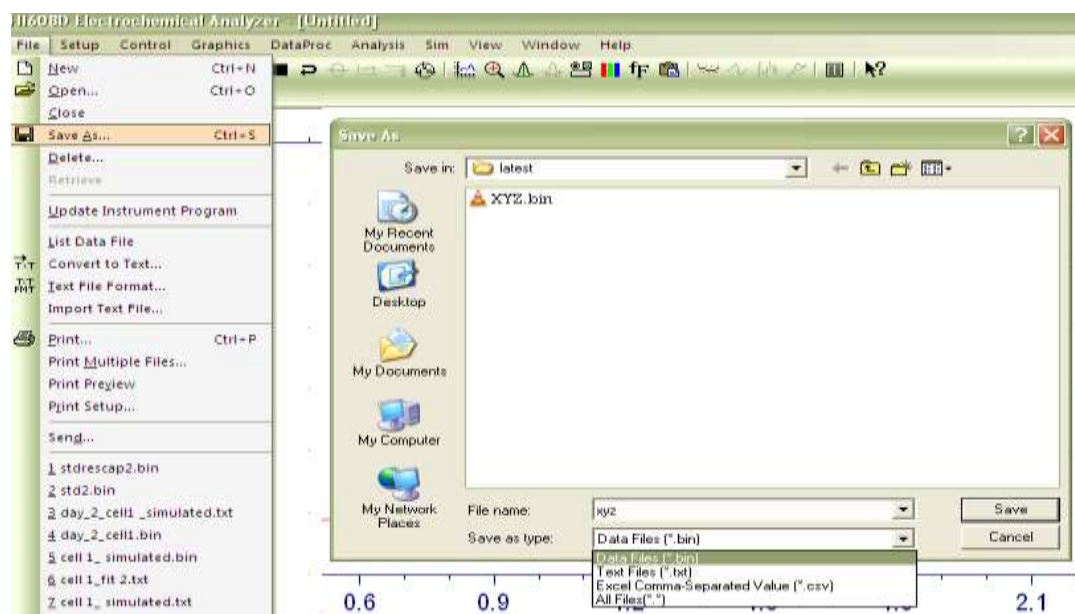
Fitting of equivalent circuit

Step 1: Open **"XYZ .bin"** file.

Step 2: Go to "**Sim→ Mechanism"**.

Step 3: Select the electrical components from the icon bar and place them on the white screen. Connect all the elements.
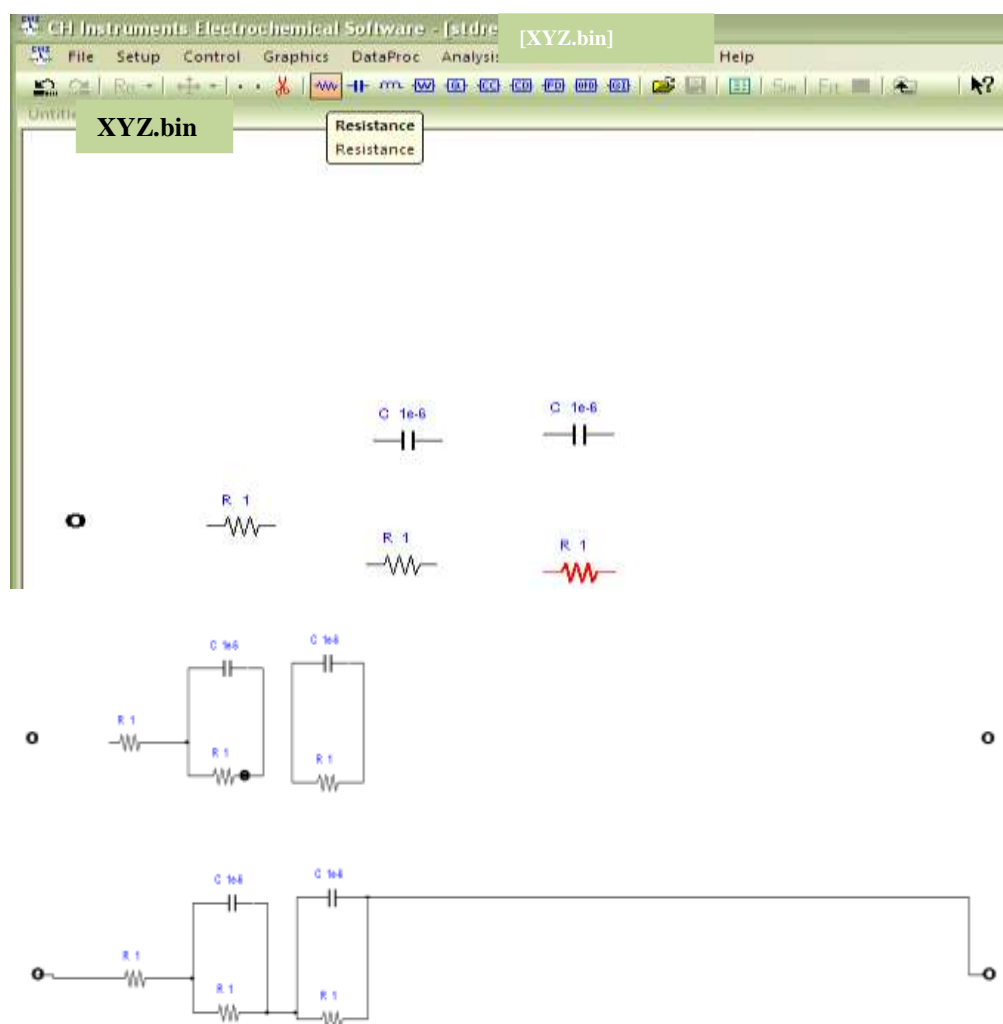
Step 4: Double-click on each element. Enter initial guess in "**Value**". Click OK.

Step 5: Click "**Param".**
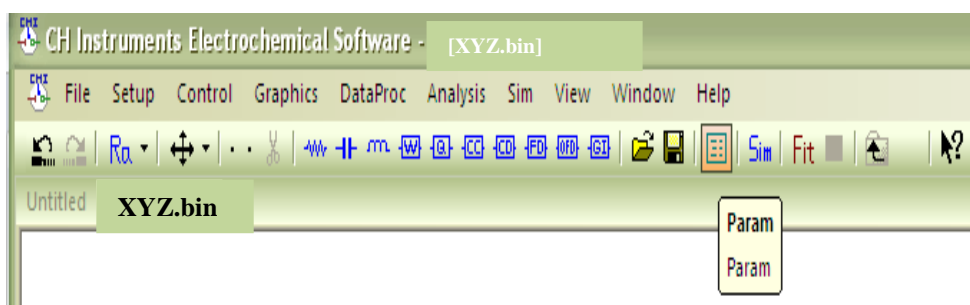
Step 6: Check whether the parameters are the same as entered in "**A.C. Impedance Parameters**". Then Click OK.
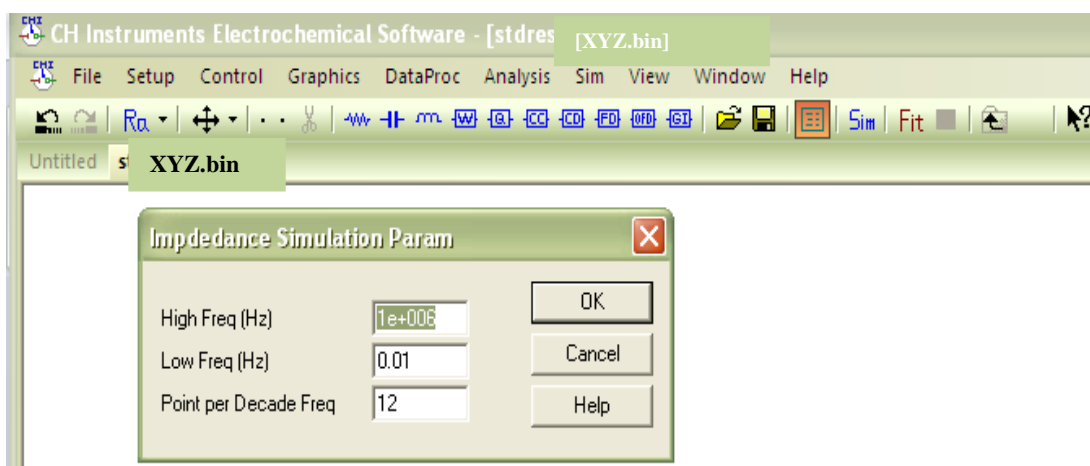
Step 7: The electrical model is now ready to be fit. Click on **"Fit".**
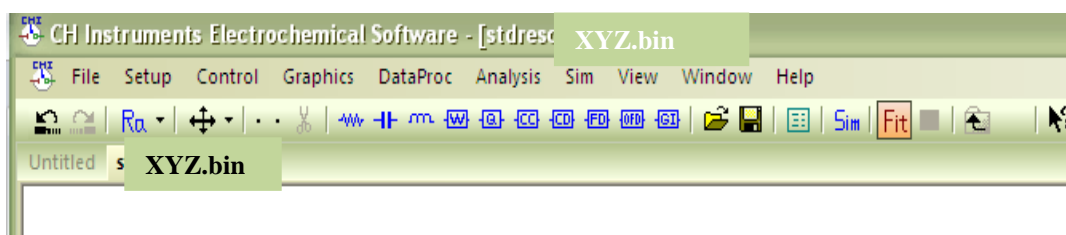
 Step 8: The fitting goes on for some time. This is indicated by the timer on the white space. When the timer stops, this indicates the end of fitting. Save the model by choosing save icon from icon bar. It gets saved as "XYZ_fit.imp file".

Step 9: Go to **"Sim"**. Simulate the model. The spectrum appears as shown. Save the simulated spectrum as both **"XYZ_fit_sim.bin"** and **"XYZ_fit_sim.txt".**

Step 10: Close the current window. To check whether the simulated spectrum fits with the experimental spectrum, **"File→ Open→ XYZ_fit_sim.bin".** Then click **"Sim"** in the icon bar. If the simulation is a perfect fit, save the results, otherwise repeat steps 1–10, changing the initial guess or electrical elements till a perfect fit is obtained.

Step 11: After successful fitting, save the results. Close the software. Press the button on the instrument off. Green light stops glowing. Turn off the main power supply.

Note: The ".imp" file can only be opened in the **"Sim→ Mechanism"** window. The open icon is found in the icon bar. The circuit model cannot be copied directly from ".imp" file to MSword. The model has to be redrawn in the software *ProfiCAD*. The model should be "Export"ed as a .jpg file and then copied to Word. *ProfiCAD* is a non-commercial home-use software.

II. Troubleshooting CHI 608D workstation

The operator should always check the instrument first on the standard electrical circuit provided with the instrument and then proceed with the test cell. The method for making an impedance measurement is described in section I. A photograph of the standard electrical circuit and its impedance spectrum is shown in figures A.1 and A.2.

Figure A.1 The three electrodes of the workstation connected to the standard electrical circuit.
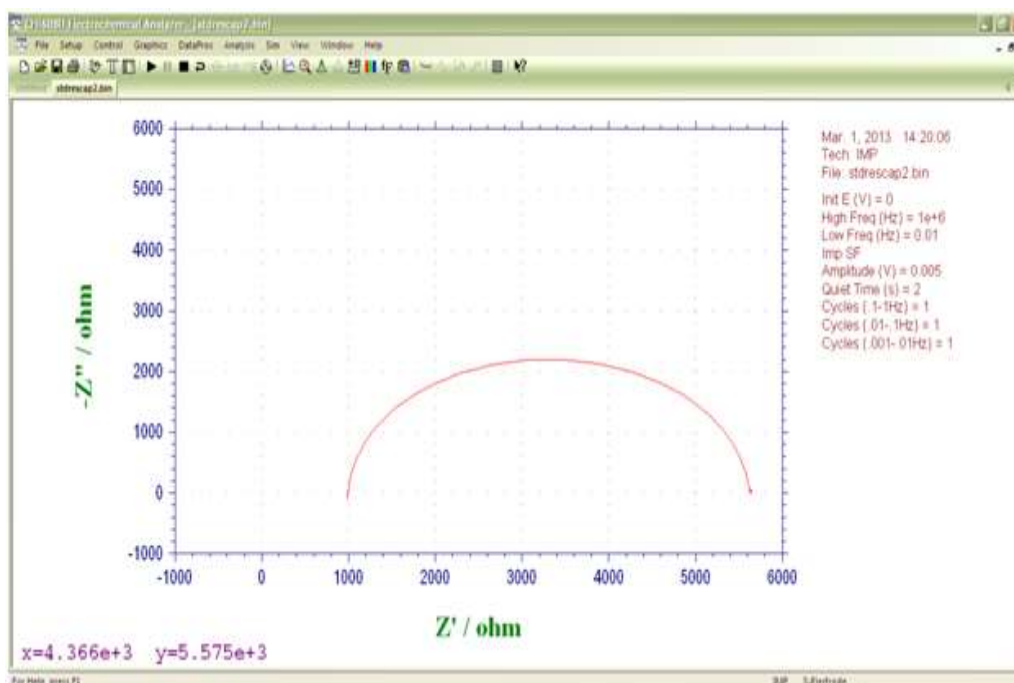
Figure A.2 Impedance spectrum of the standard electrical circuit.

Any deviation from the above spectrum indicates a problem with the hardware or the software. Contact the service engineer for further assistance.

III. Troubleshooting Newport IPCE/ QE kit

The procedure for taking a QE measurement is described in the thesis titled, "Fabrication of Zinc Oxide Nanowire arrays for use as photoanode in Dye-sensitised solar cells", by Anand Prakash[68].

There are three main problem areas. These are

1. Reference detector Si photodiode

The reference detector is a Si photodiode which displays a characteristic spectrum of *Volts vs Wavelength* as shown below. It is in the range of **"millivolts"** as shown in figure A.3. The absolute values of *Volts* changes with the *area of illumination within the active area*; illuminating a larger area gives rise to higher volts than for a smaller area. The location of the peaks, however, remains the same.
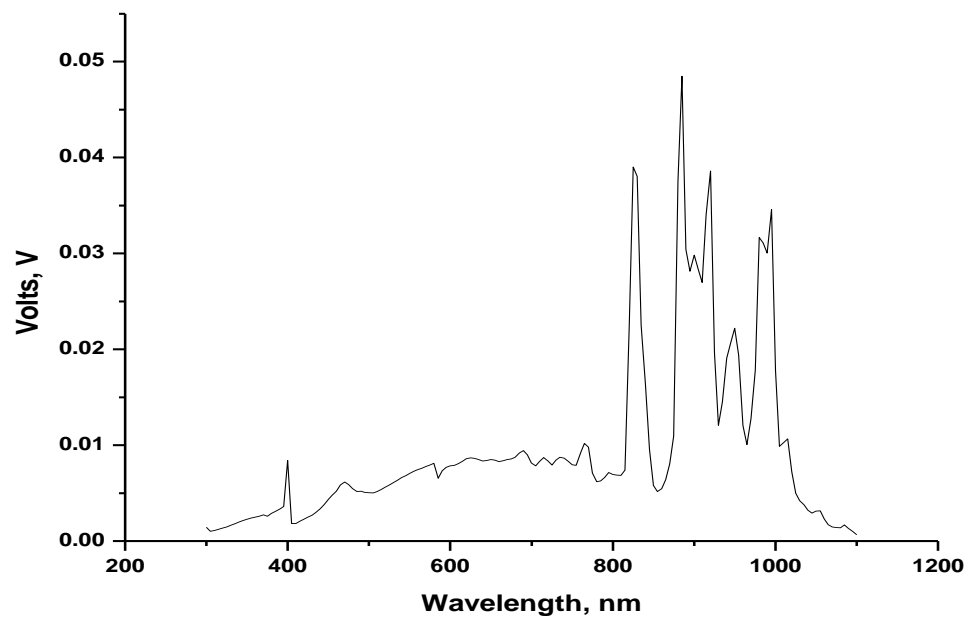
Figure A.3 Spectral response for a good amplifier.
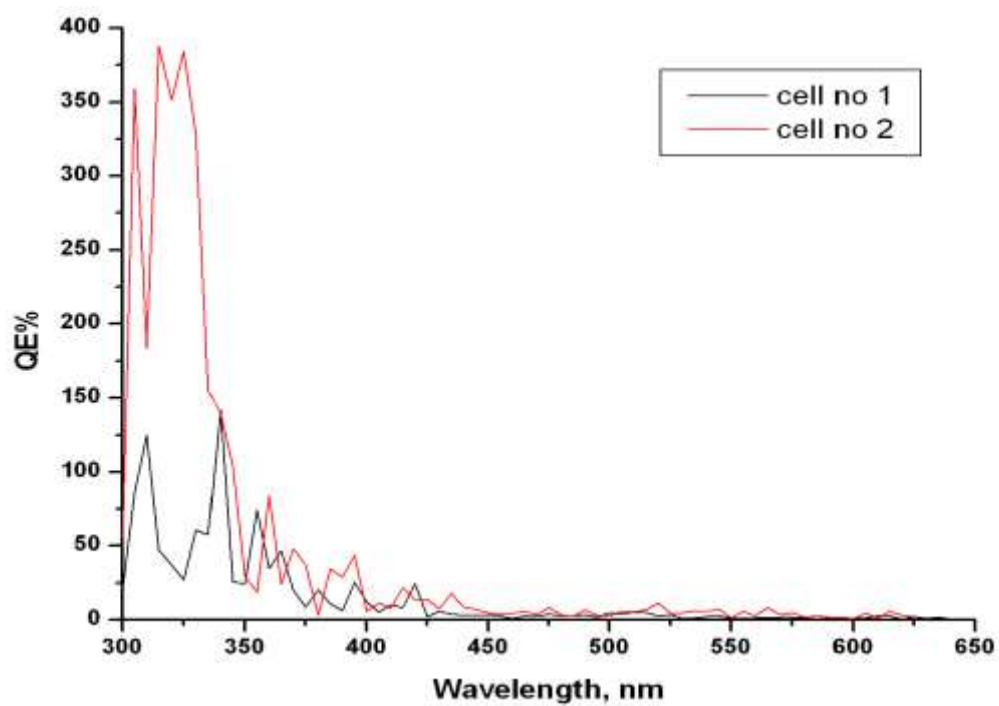
Figure A.4 QE spectrum obtained using a faulty amplifier.

Any deviation from the millivolts range, say a value of 10^{-6}V/ 10^{-9} V or a change in the location of peaks throughout the spectrum indicates that light is falling outside the active area or a problem with the hardware or a problem with the lamp. One solution is to adjust the position of the detector with respect to light to reach the millivolts range. If this does not help, contact the service engineer.

2. **Amplifier of test cell**

There are three problem areas

i. **input port** – connected to the cell. Improper connections can be identified with the help of a multimeter and rectified.

ii. **output port** – any of the three leads: red, white and black can detach from their respective sockets and should be inserted into the sockets by following the colour code in the manual. The colour code should be strictly followed; otherwise, amplifier hardware can get damaged and may explode.

iii. **amplifier electronics**

In cases i and ii, the *QE* value is at "0" throughout the spectrum; in case iii, the *QE* is as shown in figure A.4 and repair can be done only by the service engineers.

3. **Software settings**

In the Tracq Basic software controlling the operation of the QE system, under the **"Gain"** menu, there are two values: "Gpreamp – 10000 , Gref – 1000". Addition of a "0" in the former or deletion of "0" in the latter can lead to abnormal QE values like 300%, 400% or 2500%.

IV. Troubleshooting in I-V measurements

Error can occur due to an improper connection of the measuring leads or due to faulty leads. When the connections are proper and the leads are in a **good condition**, the I-V curve parameters, resistance at short circuit and open circuit – $\mathbf{R_{@}I_{sc}}$ & $\mathbf{R_{@}V_{oc}}$ respectively – are **different**. For **fault** cases, $\mathbf{R_{@}I_{sc}} = \mathbf{R_{@}V_{oc}}$. So, the connections or the leads themselves should be changed.

References

1. Chapter 1, Dye-sensitised solar cells, edited by K.Kalyanansundaram, EPFL Press, 2010.

2. Jung Hei Choi et al, Thienyl-substituted methanofullerene derivatives for organic photovoltaic cells, *J. Mater. Chem*., 2010, 20, pp. 475–482.

3. Diana K. Susarova et al, Photovoltaic performance of PPE-PPV copolymers: effect of the fullerene component, *J. Mater. Chem*., 2011, 21, pp. 2356–2361.

4. Robert Meier et al, Efficiency-improved organic solar cells based on plasticizer assisted soft embossed PEDOT:PSS layers, *Phys. Chem. Chem. Phys*., 2012, 14, pp. 15088–15098.

5. Takeyoshi Sugaya et al, Ultra-high stacks of InGaAs/GaAs quantum dots for high efficiency solar Cells, *Energy Environ. Sci.,* 2012, 5, pp. 6233-6237.

6. Liang-Yi Chang et al, Low-Temperature Solution-Processed Solar Cells Based on PbS Colloidal Quantum Dot/CdS Heterojunctions, *Nano Lett*., 2013,13,pp 994-999

7. Matthew S. Faber et al, Earth-Abundant Cobalt Pyrite (CoS_2) Thin Film on Glass as a Robust, High-Performance Counter Electrode for Quantum Dot-Sensitized Solar Cells, *J. Phys. Chem. Lett*.,2013, 4, pp. 1843−1849.

8. Matthew G. Panthani et al, $CuInSe_2$ Quantum Dot Solar Cells with High Open-Circuit Voltage, *J. Phys. Chem. Lett*., 2013, 4, pp. 2030−2034.

9. Martin A. Green et al, Solar cell efficiency tables, *Prog. Photovolt: Res. Appl.,* 2012, 20, pp. 12–20

10. http://www.dyesol.com/media/wysiwyg/asx/2011/034-2011-Strategic-Vision-Buildings-as-Power-Stations-21062011.pdf

11. Michael Gratzel & Brian O' Regan, A low-cost high efficiency solar cell based on dye-sensitized colloidal TiO_2 films, *Nature,* 1991, 353, pp. 737-739.

12. Kai Zhu et al**,** Enhanced Charge-Collection Efficiencies and Light Scattering in Dye-Sensitized Solar Cells Using Oriented TiO_2 Nanotubes Arrays, *Nano Lett*., 2007, Vol. 7, No. 1, pp. 69-74.

13. Gopal K. Mor et al, Use of Highly-Ordered TiO_2 Nanotube Arrays in Dye-Sensitized Solar Cells, *Nano Lett.*, Vol. 6, No. 2, 2006, pp. 215-218.

14. Jih-Jen Wu et al, Performance and electron transport properties of TiO_2 nano composite dye-sensitized solar cells, *Nanotechnology*, 19, 2008, 105702, pp. 1-7.

15. Hyung-Jun Koo et al, Nano-embossed Hollow Spherical TiO_2 as Bifunctional Material for High-Efficiency Dye-Sensitized Solar Cells, *Adv. Mater.* 2008, 20, pp. 195–199.

16. J B Baxter et al, Synthesis and characterization of ZnO nanowires and their integration into dye-sensitized solar cells, *Nanotechnology*, 2006, 17, S304–S312.

17. Alex B. F. Martinson et al, ZnO Nanotube Based Dye-Sensitized Solar Cells, *Nano Lett.*, Vol. 7, No. 8, 2007, pp. 2183-2187.

18. Feng Xu et al, Hierarchical ZnO Nanowire-Nanosheet Architectures for High Power Conversion Efficiency in Dye-Sensitized Solar Cells, *J. Phys. Chem. C.,* 2010, 114, pp. 2776–2782.

19. Chen-Hao Ku et al, Wet-Chemical Route to ZnO Nanowire-Layered Basic Zinc Acetate/ ZnO Nanoparticle Composite Film, *Crystal Growth & Design*, 2008, Vol. 8, No. 1, pp. 283-290.

20. Seung Hwan Ko et al, Nanoforest of Hydrothermally Grown Hierarchical ZnO Nanowires for a High Efficiency Dye-Sensitized Solar Cell, *Nano Lett.* 2011, 11, pp. 666–671.

21 Etienne Puyoo et al, Efficient Dye-Sensitized Solar Cells Made from ZnO Nanostructure Composites, *J. Phys. Chem. C*, 2012, 116, pp. 18117−18123.

22. Nafiseh Memarian et al, Hierarchically Assembled ZnO Nanocrystallites for High-Efficiency Dye-Sensitized Solar Cells, *Angew. Chem. Int. Ed.*, 2011, 50, pp. 12321 –12325.

23. Aswani Yella et al, Porphyrin-Sensitized Solar Cells with Cobalt (II/III)–Based Redox Electrolyte Exceed 12 Percent Efficiency, *Science*, 2011, 334, pp 629-634

24．Wangdong Zeng et al, Efficient Dye-Sensitized Solar Cells with an Organic Photosensitizer Featuring Orderly Conjugated Ethylenedioxythiophene and Dithienosilole Blocks, *Chem. Mater.*, 2010, 22, pp. 1915–1925

25. Jorge Garcıa-Canadas et al., Determination of electron and hole energy levels in mesoporous nanocrystalline TiO_2 solid-state dye solar cell, *Synthetic Metals*, 2006, 156, pp. 944–948.

26. Jessica E. Kroeze et al., Parameters Influencing Charge Separation in Solid-State Dye-Sensitized Solar Cells Using Novel Hole Conductors, *Adv. Funct. Mater.,* 2006, 16, pp. 1832–1838.

27．Bing-Xin Lei et al., All-solid-state electrolytes consisting of ionic liquid and carbon black for efficient dye-sensitized solar cells, *Journal of Photochemistry and Photobiology A: Chemistry*, 216, 2010, pp. 8–14.

28．K. Imoto et al, High-performance carbon counter electrode for dye-sensitized solar cells, *Solar Energy Materials & Solar Cells*, 2003, 79, pp. 459–469.

29. Takurou N. Murakami et al, Highly Efficient Dye-Sensitized Solar Cells Based on Carbon Black Counter Electrodes, *Journal of The Electrochemical Society,* 2006, 153**,** 12, A2255-A2261.

30. E. Ramasamy et al, Nanocarbon counterelectrode for dye sensitized solar cells, *Appl. Phys. Lett.*, 2007, 90, 173103.

31. E. Ramasamy et al, Spray coated multi-wall carbon nanotube counter electrode for tri-iodide I_3^- reduction in dye-sensitized solar cells, *Electrochemistry Communications*, 2008, 10, pp. 1087–1089.

32. Krishna P. A et al, Pulsed laser deposition of graphite counter electrodes for dye-sensitized solar cells, *Applied Physics Letters*, 2010, 97, 201108.

33. Reeti Bajpai et al, Graphene Supported Platinum Nanoparticle Counter-Electrode for Enhanced Performance of Dye-Sensitized Solar Cells, *ACS Appl. Mater. Interfaces*, 2011, 3, pp. 3884–3889.

34. T. Battumur et al, Graphene/carbon nanotubes composites as a counter electrode for dye-sensitized solar cells, *Current applied physics*, 2012, 12, e49-e53.

35. Joseph D. Roy-Mayhew et al, Functionalized Graphene Sheets as a Versatile Replacement for Platinum in Dye-Sensitized Solar Cells, *ACS Appl. Mater. Interfaces*, 2012, 4, pp. 2794−2800.

36. Sanqing Huang et al, A novel fabrication of a well distributed and aligned carbon nanotube film electrode for dye-sensitized solar cells, *J. Mater. Chem.*, 2012, 22, pp. 16833-16838.

37. Weiwei Tan et al, Electrophoretic deposition of nanocrystalline TiO_2 films on Ti substrates for use in flexible dye-sensitized solar cells, *Electrochimica Acta*, 54, 2009, pp. 4467–4472.

38. Jong Hyeok Park et al, Fabrication of an Efficient Dye-Sensitized Solar Cell with Stainless Steel Substrate, *Journal of The Electrochemical Society*, 2008, 155, 7, F145-F149.

39. Kun Seok Lee et al, Enhanced light harvesting in dye-sensitized solar cells with highly reflective TCO- and Pt-less counter electrode, *J. Mater. Chem.*, 2011, 21, pp. 15193-15196.

40. Chapter 10, Dye-sensitised solar cells, edited by K.Kalyanansundaram, EPFL Press, 2010.

41. Qifeng Zhang et al, ZnO Nanostructures for Dye-Sensitized Solar Cells, *Adv. Mater.,* 2009, 21, pp. 4087–4108.

42. www.solaronix.com.

43. Lori E. Greene et al, Low-Temperature Wafer-Scale Production of ZnO Nanowire Arrays, Angew.Chem.Int.Ed., 2003, 42, pp. 3031–3034.

44. Guang Zhu et al, Synthesis of vertically aligned ultra-long ZnO nanowires on heterogeneous substrates with catalyst at the root, *Nanotechnology*, 2012, 23, 055604.

45. M. K. Nazeeruddin et al, A high molar extinction coefficient charge transfer sensitizer and its application in dye-sensitized solar cell, *Journal of Photochemistry and Photobiology A: Chemistry*, 2007, 185, pp. *331–337.*

46．R. Katoh et al., Kinetics and mechanism of electron injection and charge recombination in dye-sensitized nanocrystalline semiconductors, *Coordination Chemistry Reviews*, 2004, 248, pp. 1195–1213.

47．Chapter 1, Dye-sensitised solar cells, edited by K.Kalyanansundaram, EPFL Press, 2010.

48. Shahzada Ahmad, et al., Metal free sensitizer and catalyst for dye sensitized solar cells, Energy Environ. Sci., 2013, 6, 3439–3466.

49. Seok-Soon Kim et al, Electrodeposited Pt for cost-efficient and flexible dye-sensitized solar cells, *Electrochimica Acta*, 2006, 51, pp. 3814–3819.

50. Xiaoming Fang et al, Effect of the thickness of the Pt film coated on a counter electrode on the performance of a dye-sensitized solar cell, *Journal of Electroanalytical Chemistry*, 2004, 570, pp. 257–263.

51．Yuh-Lang Lee et al, A platinum counter electrode with high electrochemical activity and high transparency for dye-sensitized solar cells, *Electrochemistry Communications*, 2010, 12, pp. 1662–1665.

52．Daesub Hwang et al, High-Efficiency, Solid-State, Dye-Sensitized Solar Cells Using Hierarchically Structured TiO_2 Nanofibers, *ACS Appl. Mater. Interfaces,* 2011, 3, pp. 1521–1527.

53. Jin Hyuck Heo et al, Efficient inorganic–organic hybrid heterojunction solar cells containing perovskite compound and polymeric hole conductors, *Nature Photonics*, 2013, 7, pp. 486-491.

54．Chapter 9, Dye-sensitised solar cells, edited by K.Kalyanansundaram, EPFL Press, 2010.

55．Chapter 7, Dye-sensitised solar cells, edited by K.Kalyanansundaram, EPFL Press, 2010.

56. Seigo Ito et al, Fabrication of thin film dye sensitized solar cells with solar to electric power conversion efficiency over 10%, *Thin Solid Films*, 2008, 516, pp. 4613–4619.

57. Chapter 12, Dye-sensitised solar cells, edited by K.Kalyanansundaram, EPFL Press, 2010.

58. www.gamry.com

59. D.M. Bastidas et al., Application of Kramers-Kronig relationships for titanium impedance data validation in a Ringer's solution, *Rev. Metal. Madrid*, 2004, 40, pp. 304-311.

60. Qing Wang et al, Electrochemical impedance spectroscopic analysis of Dye-sensitised solar cells, *J.Phys. Chem.B*, 2005, 109, pp. 14945-14953

61. Chapter 12, Dye-sensitised solar cells, edited by K.Kalyanansundaram, EPFL Press, 2010.

62. J. Van de Lagemmet et al, *J.Phys Chem B,.* 2000, 104, pp. 2044-2052.

63. http://pubchem.ncbi.nlm.nih.gov

64. K.Takechi, R.Muszynski and P.V. Kamat, Fabrication procedure of dye-sensitized solar cells, http://www3.nd.edu/~pkamat/pdf/solarcell.pdf.

65. Seigo Ito et al, Fabrication of Screen-Printing Pastes From TiO_2 Powders for Dye-Sensitised Solar Cells, *Prog. Photovolt: Res. Appl.*, 2007, 15, pp. 603–612.

66. Anneke Hauch & Andreas Georg, Diffusion in the electrolyte and charge-transfer reaction at the platinum electrode in dye-sensitized solar cells, *Electrochimica Acta*, 2001, 46, pp. 3457–3466.

67. Qing Wang et al., Electrochemical Impedance Spectroscopic Analysis of Dye-Sensitized Solar Cells, *J. Phys. Chem. B* **2005,** *109,* 14945-14953.

68. Anand Prakash, Fabrication of Zinc Oxide Nanowire Arrays for use as Photoanodes in Dye-sensitized Solar Cells, *ME Thesis Report*, IISc., 2012.